LIÈGE université Library

https://lib.uliege.be

https://matheo.uliege.be

Validation of the ColFOWT collision assessment tool for ship/offshore wind turbines

Auteur : Vandegar, Gabriel
Promoteur(s) : Rigo, Philippe
Faculté : Faculté des Sciences appliquées
Diplôme : Master : ingénieur civil mécanicien, à finalité spécialisée en "Advanced Ship Design"
Année académique : 2022-2023
URI/URL : http://hdl.handle.net/2268.2/18060

Avertissement à l'attention des usagers :

Tous les documents placés en accès ouvert sur le site le site MatheO sont protégés par le droit d'auteur. Conformément aux principes énoncés par la "Budapest Open Access Initiative"(BOAI, 2002), l'utilisateur du site peut lire, télécharger, copier, transmettre, imprimer, chercher ou faire un lien vers le texte intégral de ces documents, les disséquer pour les indexer, s'en servir de données pour un logiciel, ou s'en servir à toute autre fin légale (ou prévue par la réglementation relative au droit d'auteur). Toute utilisation du document à des fins commerciales est strictement interdite.

Par ailleurs, l'utilisateur s'engage à respecter les droits moraux de l'auteur, principalement le droit à l'intégrité de l'oeuvre et le droit de paternité et ce dans toute utilisation que l'utilisateur entreprend. Ainsi, à titre d'exemple, lorsqu'il reproduira un document par extrait ou dans son intégralité, l'utilisateur citera de manière complète les sources telles que mentionnées ci-dessus. Toute utilisation non explicitement autorisée ci-avant (telle que par exemple, la modification du document ou son résumé) nécessite l'autorisation préalable et expresse des auteurs ou de leurs ayants droit.

Validation of the ColFOWT collision assessment tool for ship/offshore wind turbines

Submitted on August 1, 2023

by

VANDEGAR Gabriel | Rue du Bex 74 | 4870 Nessonvaux | gabriel.vandegar@student.uliege.be

Student ID No.: 222202280

First reviewer:

Prof. Patrick Kaeding

Chair of Ship Structures

University of Rostock

18051 Rostock

Germany

Second reviewer:

Prof. Le Sourne Hervé

Chair of Mechanical Engineering

ICAM Engineering School

44470 Carquefou

France

MASTER THESIS

Abstract

The consequences of ship collisions against offshore wind turbines can range from minor structural damage to catastrophic failure, depending on various factors such as vessel initial kinetic energy, impact location, and geometry. To address this critical issue, the ColFOWT (Collision against Floating Offshore Wind Turbines) project focuses on developing a rapid collision assessment tool that integrates closed-form analytical models. This tool predicts the complex energy transfer processes during impacts and aims to validate its accuracy through numerical simulations using the LS-DYNA non-linear FEM package.

In this mater thesis, the analytical tool for spar-buoy floating platforms is presented. The developed method adopts a semi-coupled approach, using the rigid-body dynamics program MCOL to simulate the external dynamics of the floating wind turbine. Meanwhile, internal mechanics are computed using an elasto-plastic simplified method for the impact response of standalone tubular offshore wind turbine supports. An overview of the algorithm is provided, including a detailed explanation of both internal mechanics and external dynamics solvers, along with the coupling method.

The presented collision tool is validated by comparing it against simulations conducted with LS-DYNA/MCOL. The case study involves various offshore supply vessels impacting, with varying initial velocities, an NREL 5 MW baseline turbine mounted on an OC3 Hywind reference spar platform. The results demonstrate that in most of the cases, the analytical tool is able to capture quite accurately the response of both the turbine and the vessel, accounting for the action of both the surrounding water and the mooring lines. Its current limitations are also highlighted and, although there is still room for improvement, this user-friendly and cost-effective complementary tool shows good accuracy for the early-design stage.

Keywords: Ship Collisions, Offshore Wind Turbines, Simplified Methods, Finite Element Analysis.

Contents

1. INTRODUCTION **1**

1.1. Background and motivation 1
1.2. Numerical Simulation Methods for Ship-FOWT Collision 3
1.3. Objectives of the Research 4
1.4. Outline of the Thesis 5

2. PHYSICS AND BASIC THEORY **7**

2.1. General Description 7
2.2. Internal Mechanics 8
2.3. External Dynamics 9
2.4. Coupling Approach 11

3. EXISTING SOLVERS **14**

3.1. Introduction 14
3.2. MCOL External Dynamics Solver 15
3.3. Super Element Solver 17
Phase I - Local Elastic Denting 19
Phase II - Local Plastic Denting 21
Phase III - Elephant Foot Buckling 23
3.4. Moorline Solver 24

4. COUPLING OF THE SOLVERS **28**

4.1. Introduction 28
4.2. Definition of the Hypotheses 28
4.3. Step-by-Step Algorithm 29
Step 1 29
Step 2 30
Step 3 30
Step 4 32
Step 5 33
Step 6 33
Step 7 34

5. VALIDATION OF THE COUPLING **36**
5.1. Introduction 36
5.2. Finite Element Model Description 38
5.3. FE Results and Comparison with the SE Solver 41
Initial energy of 12 MJ 41
Initial energy of 75 MJ 45
Kinetic Energy Breakdown 48
5.4. Discussion of the Results 50

6. CONCLUSION **53**
6.1. Summary and Perspective 53
6.2. Recommendation for Future Work 54

Bibliography **55**

Appendix **58**
A. ICCGS 2023 Article 58
B. FOWT.mco File Example 68
C. Scheme of the SE Solver 72
D. Scheme of the Moorline Solver 73
E. LS-DYNA version R13 Issues 74

List of Figures

1.1. Types of floating offshore wind turbines. *From (Ladeira, 2023*) 1
1.2. Damaged monopile foundation from an impact of a drifting cargo vessel (Dutch North Sea). *From (Margientimmer, 2022*) 2
1.3. Semi-submersible DTU 10 MW turbine mounted on the OO-STAR floater. *From: Konsept-It* 4
1.4. Deformation mechanism of a spar type FOWT. 5

2.1. Illustration of the main physical phenomena in a ship/FOWT collision where the interaction of the water, mooring lines, soil and impact force can be seen. *From (Ladeira et al., 2022)* 8
2.2. Strain-load diagram. *From: Norsok, 2004* 9
2.3. External dynamics applied on a FOWT during a collision. *From: Ladeira et al., 2022* 10
2.4. Example of a semi-coupled algorithm. In this code snippet, two solvers are defined, each one can either be run independently or in a semi-couple manner. . 12

3.1. Schematic representation of the MCOL solver as a black box. 15
3.2. Body-fixed and earth-fixed reference systems used in MCOL. *From: Le Sourne et al., 2001* 16
3.3. Example of the application of MCOL. *From (Le Sourne et al., 2001)* 17
3.4. Schematic representation of the SE solver as a black box. 18
3.5. Representation of the FOWT in the SE solver. *From (Ladeira, 2023*) 19
3.6. Local elastic denting mode subjected to two diametrically opposed concentrated loads. *From: Ladeira et al., 2023* 19
3.7. Local elastic denting mode subjected to one concentrated loads. *From (Ladeira et al., 2023)* 20
3.8. Definition of the displacement field for *Phase II*. *From (Ladeira et al., 2023)* . . 21
3.9. Schematic representation of the displacement fields defined for the deformation pattern at the base of the tube. *From (Ladeira et al., 2023)* 23
3.10. Example of force-penetration and penetration-time diagram computed with the SE solver. 24
3.11. Schematic representation of the Moorline solver as a black box 25

3.12. Mooring line description in local reference system 25

4.1. Overall description of the system solved by the ColFOWT algorithm. 29
4.2. Computation of the penetration δ geometrically. 31
4.3. Scheme illustrating the deformation of the FOWT in each phase. 32
4.4. Comparison between the inclusion or not of the vertical component of the mooring line force. (These results have been achieved disregarding the ship impact force and neglecting in MCOL calculation the wave radiation and drag damping forces) 33
4.5. Schematic diagram of the ColFOWT algorithm. 35

5.1. Diagram with the main dimensions of the OC3-Hywind. 36
5.2. Diagram with the main dimensions of the numerical model. 39
5.3. Finite element model setup. An element size of 25 cm and 10 cm is used for the FOWT and the impactor, respectively. 40
5.4. Collision time history plot for an impactor with a mass of 6000 $tons$ and initial velocity of 2 m/s (scenario 1). 41
5.5. Results obtained considering an initial energy of $E_0 = 12\ MJ$. Continuous and dashed lines represent the analytical and numerical results respectively (The time history plots are given for the range [0; t^*]). 43
5.6. Computation of the local penetration δ_{loc} geometrically. 44
5.7. Collision time history plot for an impactor with a mass of 6000 $tons$ and initial velocity of 5 m/s (scenario 3). 46
5.8. Results obtained considering an initial energy of $E_0 = 75\ MJ$. Continuous and dashed lines represent the analytical and numerical results respectively (The time history plots are given for the range [0; t^*]). 47
5.9. Elephant foot deformation mechanism recorded in LS-DYNA at $t = 4\ s$ after the impact of an impactor with a mass of 24000 $tons$ and initial velocity of 2.5 m/s (Scenario 4). 48
5.10. Diagram of numerical results of the kinetic energy breakdown for an impactor ship with a mass of 6000 $tons$ and initial velocity 2 m/s. 50

C.1. Schematic diagram of the SE solver algorithm. In the "Update Kinematics" box, the parameters v_{imp} and a_{imp} denote the velocity and acceleration of the impactor, respectively. *From: Ladeira et al., 2023* 72
D.1. Schematic diagram of the Moorline algorithm. *From: Jonkman et al., 2007* . . 73
E.1. Issue with the velocity computation in LS-DYNA version R13. In the velocity time history plot: (i) the continuous line is the velocity computed by LS-DYNA; (ii) the dashed line is the velocity computed by integration of the acceleration. 74

List of Tables

5.1. Main particulars of the OC3-Hywind. 37
5.2. Structural properties of the OC3-Hywind. 37
5.3. Properties of the mooring lines. 37
5.4. Main dimensions of the numerical model. 38
5.5. Structural properties of the numerical model. 39
5.6. Summary of the different scenarios studied in this paper. 41
5.7. Comparison of the maximum resistance force, penetration, absorbed energy, CoG translational displacement, CoG roll angle and time of contact obtained numerically and with the simplified analytical method for an initial energy of 12 MJ. 42
5.8. Comparison of the maximum resistance force, penetration, absorbed energy, CoG translational displacement, CoG roll angle and time of contact obtained numerically and with the simplified analytical method for an initial energy of 75 MJ. 46
5.9. Kinetic energy distribution in percent considering the mass matrices. 49
5.10. Kinetic energy distribution in percent considering the motion of the FOWT. . . 50

List of Abbreviations

ALS	Accidental Limit States
CFD	Computational Fluid Dynamics
CoG	Center of Gravity
ColFOWT	Collision against Floating Offshore Wind Turbine
DOF	Degree Of Freedom
EOM	Equation Of Motion
FEA	Finite Element Analysis
FOWT	Floating Offshore Wind Turbine
ICAM	Institut Catholique d'Arts et Métiers
ICCGS	International Conference on Collision and Grounding of Ships and Offshore Structures
IEA	International Energy Agency
NLFEA	Non-Linear Finite Element Analysis
OOP	Object Oriented Programming
OSV	Offshore Supply Vessel
OWT	Offshore Wind Turbine
PP	Procedural Programming
RNA	Rotor Nacelle Assembly
SE	Super Element
SPH	Smoothed Particle Hydrodynamics
TLP	Tension Leg Platform

List of Symbols

Greek letters (scalars)

δ	Penetration
$\dot{\delta}$	Penetration rate
$\delta_{fowt},\ \delta_{ship}$	Deformation of the FOWT/ship
δ_{loc}	Local identation
μ	Linear mass
ν	Poisson coefficient
$\phi,\ \theta,\ \psi$	Roll, pitch and yaw
ρ	Density
σ_y	Ultimate strength
$\zeta_1,\ \zeta_2$	Critical penetration in Phase I/Phase II

Latin letters (scalars)

A	Sectional area
B_r	Ring bending stiffness
C_B	Seabed static-friction drag coefficient
E	Young modulus
$\dot{E}$	Deformation energy rate
E_h	Work made by the hydrostatic force
E_{hydro}	Work made by hydro-mechanical forces
E_{moor}	Mooring system potential energy
E_{tot}	Energy total
E_v	Work made by the viscous damping force
E_w	Work made by the wave interaction force
$F_1,\ F_2,\ F_3$	Contact force during Phase I/Phase II/Phase III in the SE solver

$F_c^1,\ F_c^2$	Critical force in Phase I/Phase II in the SE solver
F_c	Contact force
g	Gravitational acceleration
H	Distance between the CoG of the FOWT and the impact point
$H_A,\ H_F$	Horizontal force at the anchor/fairlead point
$K,\ M,\ N$	Moment around x, y and z axis, respectively
K_0	Ship initial kinetic energy
K_{ext}	Energy related to the external dynamics
$K_{fowt},\ K_{ship}$	Kinetic energy of the FOWT/ship
L	Length
L_B	Length of mooring line laying on seabed
m_{ship}	Ship mass
$p,\ q,\ r$	Angular velocity around x, y and z axis, respectively
R	Radius
$R_{fowt},\ R_{ship}$	Resistance force of the FOWT/ship
t	Thickness
$U_{fowt},\ U_{ship}$	Energy of deformation of the FOWT/ship
U_{int}	Energy related to the internal dynamics
$u,\ v,\ w$	Velocity component in surge, sway and heave, respectively
$V_A,\ V_F$	Vertical force at the anchor/fairlead point
v_0	Ship initial velocity
v_a, v_{ship}	Impact point/ship velocity
w	Linear apparent weight in water
w_1	Radial displacement
$X,\ Y,\ Z$	Force component in x, y and z direction, respectively
$x_F,\ z_F$	Horizontal/vertical distance from anchor point to fairlead point
$x_{OG},\ y_{OG},\ z_{OG}$	Position component of body-fixed reference system in earth-fixed reference system

Lowercase Latin bold letters (vectors)

$\boldsymbol{h}$	Force direction vector
$\boldsymbol{x}$	Position vector in earth-fixed reference system

$\boldsymbol{y}$	Velocity vector in body-fixed reference system
$\dot{\boldsymbol{y}}$	Acceleration vector in body-fixed reference system

Uppercase Latin bold letters (normal: matrices; italicized: forces)

$\boldsymbol{F}$	Force vector
$\boldsymbol{F_c}$	Contact force
$\boldsymbol{F_h}$	Hydrostatic restoring force
$\boldsymbol{F_m}$	Force applied by the mooring line
$\boldsymbol{F_v}$	Viscous damping force
$\boldsymbol{F_w}$	Wave interaction force
$\mathbf{G}$	Gyroscopic matrix
$\mathbf{G}_{RB}$	Gyroscopic matrix of rigid body
$\mathbf{G}_{\infty}$	water added gyroscopic matrix
$\mathbf{J}$	Transformation matrix
$\mathbf{M}$	Mass matrix
$\mathbf{M}_{RB}$	Mass matrix of rigid body
$\mathbf{M}_{\infty}$	Water added mass matrix

Declaration of Authorship

I declare that this thesis and the work presented in it are my own and have been generated by me as the result of my own original research.

Where I have consulted the published work of others, this is always clearly attributed.

Where I have quoted from the work of others, the source is always given. With the exception of such quotations, this thesis is entirely my own work.

I have acknowledged all main sources of help.

Where the thesis is based on work done by myself jointly with others, I have made clear exactly what was done by others and what I have contributed myself.

This thesis contains no material that has been submitted previously, in whole or in part, for the award of any other academic degree or diploma.

I cede copyright of the thesis in favour of Icam University

Date: **Signature:**

August 1, 2023

1. INTRODUCTION

1.1. Background and motivation

To achieve a global transition to renewable energies, offshore wind energy is a promising alternative. The offshore wind farming industry has a growing market with advancing technologies and offers a promising option for meeting increasing energy demands and Europe's goal to be carbon-neutral by 2050. Wind farms have already proven their efficiency; however, their installations are limited by factors such as water depth, tourism, or maritime traffic lanes. To increase the expansion of wind farms, floating offshore wind turbines (FOWT) have been introduced, following a similar expansion as seen for floating offshore platforms used in oil and gas production.

Floating offshore wind turbines are currently operating in Europe and Asia, and there are promising prospects for their increased use in the near future. This has led to the investigation of various platform types, such as the spar, barge, semi-submersible, and tension leg platform (TLP). These different types of FOWT are depicted in Fig. 1.1.

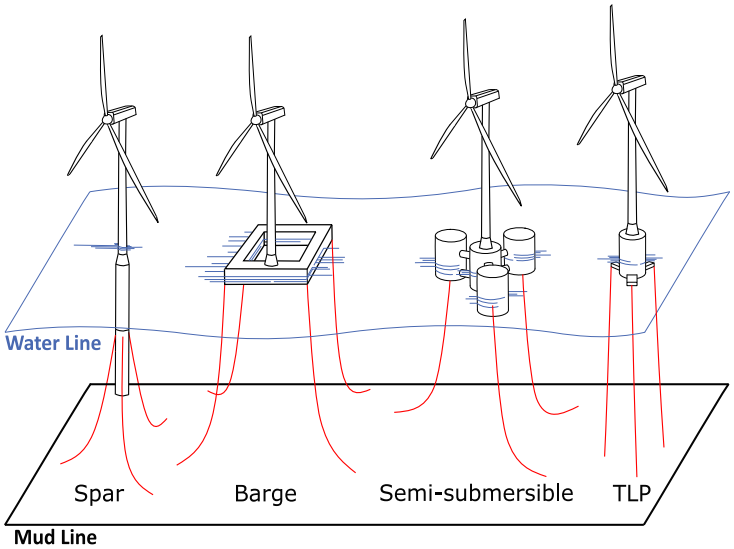

Figure 1.1.: Types of floating offshore wind turbines. *From (Ladeira, 2023)*

However, despite the promising prospects of offshore wind farming, its intensive deployment does not come without any challenges. An example of such challenges was observed when

a 37200 $tons$ cargo ship collided with another vessel, leading to the evacuation of its crew. Subsequently, the cargo ship became rudderless and drifted for several hours within the Hollandse Kust Zuid offshore wind farm in the Dutch North Sea. During this drifting period, the cargo ship collided with a monopile foundation, causing significant damage to the structure *(Hollandse Kust, 2023)*, as illustrated in Fig. 1.2.

Figure 1.2.: Damaged monopile foundation from an impact of a drifting cargo vessel (Dutch North Sea). *From (Margientimmer, 2022*)

This incident is one of the many examples of collisions between ships and offshore wind turbines (OWT). As the number of offshore wind installations continues to rise, the likelihood of such collisions also increases, particularly for wind farms situated near maritime traffic routes. Additionally, regular maintenance activities for OWT involve frequent transportation of personnel and equipment via service vessels within the wind farm. Despite occurring at relatively low speeds, these interactions still pose a significant risk of collisions *(Dai et al., 2013)*, which could result in casualties. From a structural perspective, the consequences for an OWT can vary widely, ranging from minor deformations to complete structural failure, depending on factors such as the impact energy, shape, and geometry of the striking ship, as well as environmental conditions such as wind and waves *(Bela et al., 2017)*.

Therefore, the structural design of OWTs must ensure their crashworthiness based on collision accidental limit states (ALS) prescribed by existing standards and regulations, such as *(DNV-GL, 2021)*, *(BV, 2021)*, and *(IEC, 2020)*. The goal is to prevent or, at the very least, reduce the potential outcomes of collisions. These evaluations are risk-based, involving the assessment of the probability of failure for numerous collision scenarios.

1.2. Numerical Simulation Methods for Ship-FOWT Collision

Numerical modeling of a ship-FOWT collision scenario involves unique challenges due to the multi-physics events that occur during the collision, such as the influence of water added mass and inertia, hydrostatic restoring forces, and deformation mechanisms, for example. To study the influence of various parameters, including gravity, mooring lines, ballast, hydrodynamic forces, and the impactor's deformability, on the response of the impacted structure, *Echeverry et al. (2019)* investigated the collision response of a spar-buoy FOWT impacted by a ship using the nonlinear finite element analysis (NLFEA) software LS-DYNA along with the MCOL external dynamics solver (*Le Sourne et al., 2007*). Numerical results showed that neglecting hydrodynamic loads resulted in a significant underestimation of the collision force. Therefore, it is essential to model such collision events by integrating both internal mechanics and external dynamics.

In recent research, *Zhang et al. (2021)* utilized the LOADUD subroutine in LS-DYNA to consider hydrodynamic, aerodynamic, and mooring loads in the collision model, focusing on the global motions of a spar-type FOWT and the resulting acceleration of the nacelle. In a separate study, *Yu et al. (2022)* used the cost-effective nonlinear finite element code USFOS to analyze the response of a semi-submersible DTU 10 MW turbine mounted on the OO-STAR floater (depicted in Fig. 1.3), impacted by a 7500 $tons$ OSV. The proposed model accurately captured the damage to both structures, as well as their body dynamics and contact force generated through collisions. In (*Marquez et al., 2022)*, collision between a 3000 $tons$ OSV and a reinforced concrete barge FOWT (the ITI Energy barge described in *Jonkman, 2007*) have been the subject of numerical investigations using LS-DYNA along with the MCOL external dynamics solver.

All aforementioned studies showed that NLFEA is able to provide accurate modeling of the complex physical phenomena, such as large deformations, plasticity, complex contact, and fluid-structure interaction, that occur in a ship-FOWT collision event. However, numerical simulations are time-intensive, both in terms of computational time and model preparation, making the method impractical for risk assessment where hundreds of collision scenarios involving different striking ships and impact conditions must be simulated (*Moan, 2009*).

As NLFEA is not suitable for risk assessment studies, other methodologies are being investigated to complement it. One of these approaches involves the use of super element (SE) solvers based on closed-form expressions derived from plastic analysis, which have been developed for ship-ship collisions (*Le Sourne et al., 2012*), ship-jacket collisions (*Pire et al, 2018*), and ship grounding (*Pineau et al., 2022*) simulations. Such pre-design tools are useful for conducting damage stability analyses and crashworthiness optimization for ship-ship collisions,

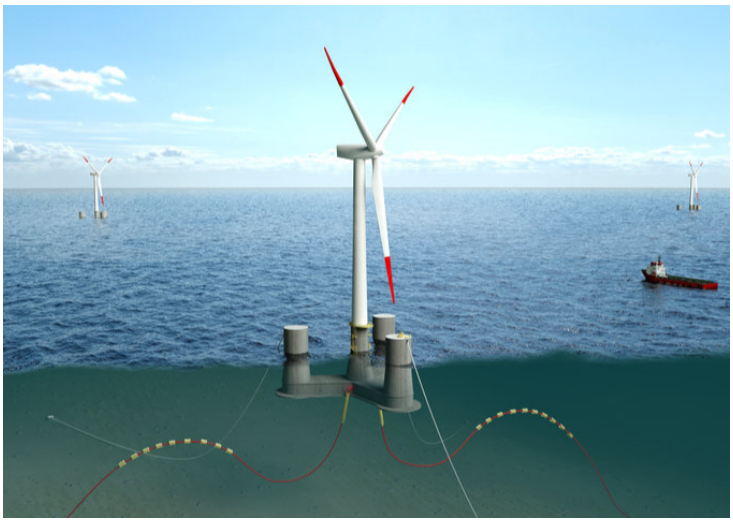

Figure 1.3.: Semi-submersible DTU 10 MW turbine mounted on the OO-STAR floater. *From: Konsept-It*

as recently demonstrated by *Conti et al. (2022)*. However, SE solvers typically neglect the elastic mechanisms that occur during collisions and consequently fail to predict the OWT resisting force in the case of low-energy impacts, as demonstrated by *Echeverry (2021)*.

To account for the elastic deformation mechanisms, *Ladeira et al. (2023)* recently developed a SE solver to simulate the elasto-plastic response of clamped-free standalone tubular OWT supports. This approach is well suited for fixed OWT but also for spar-type FOWT where the ballast of the FOWT can be assumed to be perfectly rigid and acts as a "moving" clamped boundary condition at the lower extremity of the tower.

1.3. Objectives of the Research

This thesis is a continuation of the work conducted at University of Liege and ICAM Engineering School in the frame of the Collision against Floating Offshore Wind Turbines (ColFOWT) project. The primary objective of this project is to develop a rapid assessment tool for ship-OWT collisions. This tool will utilize closed-form analytical expressions to approximate the multi-mechanism energy transfer processes that occur during such collisions. These mechanisms include local and global deformation, hydrodynamic effects, and mooring response of the system. Additionally, the tool aims to provide a user-friendly and computationally efficient approach for analysts to estimate the damage resulting from such collisions in order to perform risk assessment and damage probability analysis, among other applications.

The aim of this master thesis is to implement and validate the algorithm for the ColFOWT collision assessment tool, following the methodology proposed by *Echeverry (2021)*, specifically for a spar-type FOWT. In addition, the methodology accounts for the various deformation

mechanisms that occur during a ship-FOWT collision, as proposed by *Ladeira (2023)*. These deformation mechanisms are illustrated in Fig. 1.4.

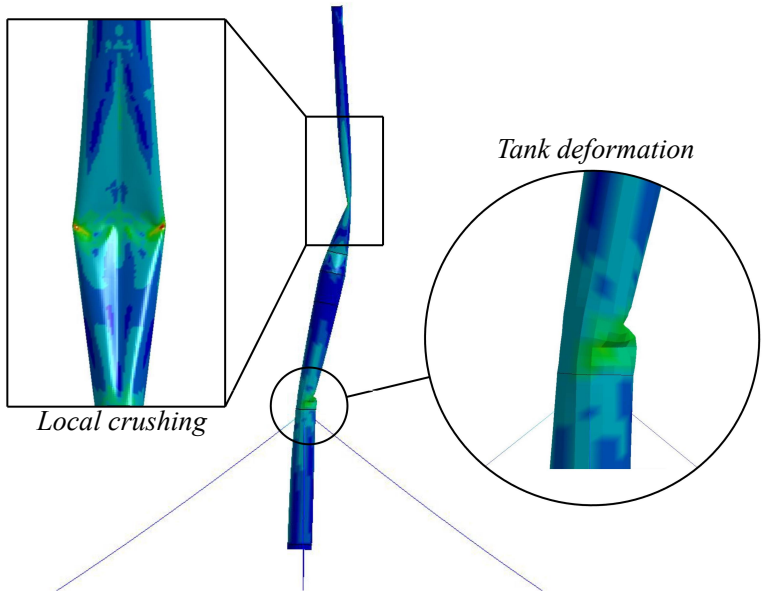

Figure 1.4.: Deformation mechanism of a spar type FOWT.

The research is structured around two main objectives:

- The development of the algorithm: This first objective is achieved by coupling two existing solvers. The resulting program will be referred as " analytical tool" in this thesis;
- The validation of the analytical tool: This second objective is achieved by conducting a series of numerical simulations, providing a reference against which the results of the analytical tool can be compared.

1.4. Outline of the Thesis

The present thesis is divided into six main sections:

Section 1 - INTRODUCTION

This section introduces the context of the research, as well as the work done previously on the matter and the objectives of the research.

Section 2 - PHYSICS AND BASIC THEORY

In this section, the physical phenomena involved in ship collisions against floating offshore wind turbines are overviewed, along with the basic theory to consider when simplifying such events.

Section 3 - EXISTING SOLVERS

Different existing solvers are used for developing the ColFOWT collision assessment tool. This section presents each of the solver considered.

Section 4 - COUPLING OF THE SOLVERS

The aim of the previous sections is to present the existing tools to better understand how they can be used in the ColFOWT collision assessment tool. This section and the following ones present the actual work performed during this master thesis at ICAM Engineering School.

In this section the algorithm developed for the ColFOWT collision assessment tool is broken down and explained step-by-step.

Section 5 - VALIDATION OF THE COUPLING

Numerical simulations of ship collisions against floating offshore wind turbine are carried out and presented in this section and comparisons with analytical results are made to validate the developed tool.

Section 6 - CONCLUSION

This section summarizes the work done in the scope of this master thesis, and gives recommendations for further work.

In addition, an article which summarizes the presented work has been written in the scope of the thesis and accepted for a presentation at the 9^{th} International Conference on Collision and Grounding of Ships and Offshore Structures (ICCGS), which will be held in September 2023 at ICAM Engineering School, Nantes, France. This article is given in the Appendix A.

2. PHYSICS AND BASIC THEORY

2.1. General Description

In general, a ship collision is characterized by the initial kinetic energy. This kinetic energy is governed by the mass of the striking ship including the hydrodynamic added mass and the speed of the ship at the moment the impact occurs. Depending on the impact conditions, this kinetic energy is dissipated in two main parts: some of the initial kinetic energy remains or/and is transferred to the impacted FOWT and governs the *external dynamics* of the system. The rest is dissipated as strain energy and governs the *internal mechanics* of the system (*NORSOK, 2004*) . Such that at anytime of the collision event, the total energy of the system (ie. ship and the impacted object) is writes:

$$E_{tot} = K_0 = U_{int} + K_{ext} \tag{2.1}$$

where E_{tot} is the total energy of the system, K_0 is the initial kinetic energy of the ship, ie. at the time of impact, U_{int} is the energy related to the *internal mechanics* of the system, and K_{ext} is the energy related to the *external dynamics* of the system.

Depending on the collision scenario, the *internal mechanics* and *external dynamics* can further be divided into different physical phenomena as illustrated in Fig. 2.1. Each of these phenomena can be studied using different approaches in order to compute the response of the system over time.

With the Fig. 2.1, it can be seen that a ship collision is a complex multi-physics event. There are water effects to be considered which might require Computational Fluid Dynamics (CFD), complex deformation mechanisms are also involved which need Non-Linear Finite Element Analysis (NLFEA). Furthermore, different boundary conditions have to be considered depending on the involved structures and the collision scenario. Therefore, Eq. 2.1 needs to be broken down into smaller parts to solve the outcome of a ship-FOWT collision.

In this section, the physical phenomena implied in the *internal mechanics* and *external dynamics* are introduced in the case of a ship colliding with a FOWT and methodologies to approach each of them are briefly described. Finally, different methods are discussed to solve the Eq. 2.1.

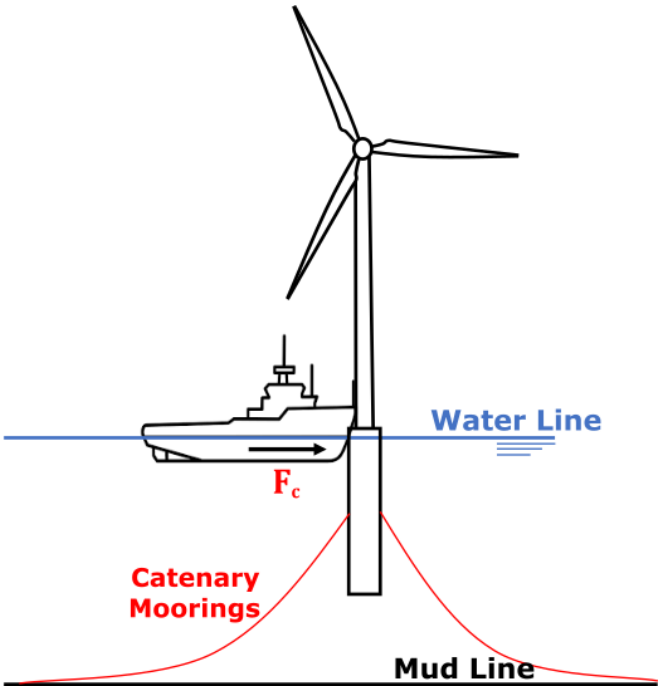

Figure 2.1.: Illustration of the main physical phenomena in a ship/FOWT collision where the interaction of the water, mooring lines, soil and impact force can be seen. *From (Ladeira et al., 2022)*

2.2. Internal Mechanics

The *internal mechanics* account for the deformation in the striking ship and the struck structure. They are therefore governed by:

- The elastic and plastic deformations of the striker, ie. the ship;
- The elastic and plastic deformations of the struck, ie. FOWT.

To simulate these structural deformations, NLFEA is commonly used but collision events may also be analyzed with simplified elasto-plastic calculation methods. In both cases, the deformation energy can be computed by means of the conservation of energy and by the conservation of momentum. Such internal energy can be illustrated with a strain-load diagram as the one given in Fig. 2.2.

In the strain-load diagram, R_{ship} and R_{fowt} are the resistance force of the ship and the FOWT respectively, δ_{ship} and δ_{fowt} are the deformations of the ship and the FOWT respectively and U_{ship} and U_{fowt} are the strain energy dissipated by the ship and the FOWT respectively (these terms can also be named the energy of deformation of the ship and the FOWT, respectively). This diagram shows that the strain energy dissipated by both the ship and FOWT is equal to the total area under the load-deformation curves. Or, it can be described mathematically as:

$$U_{int} = U_{ship} + U_{fowt} \tag{2.2}$$

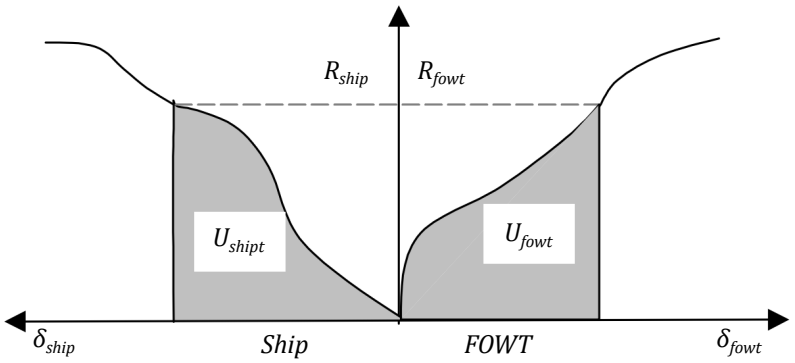

Figure 2.2.: Strain-load diagram. *From: Norsok, 2004*

where U_{ship} and U_{fowt} are calculated as:

$$U_{ship} = \int_0^{\delta_{ship,\ max}} R_{ship}\, d\delta_{ship} \tag{2.3}$$

$$U_{fowt} = \int_0^{\delta_{fowt,\ max}} R_{fowt}\, d\delta_{fowt} \tag{2.4}$$

This equation can be solved either numerically or analytically, it is typical to solve it using iterative methods where the resistance force is computed as a function of the deformation. With numerical simulation such as NLFEA, this can be solved accurately. However, with simple elasto-plastic methods, the load-deformation relationships for the ship and the FOWT are often computed independently of each other with the assumption that the other object is rigid which brings some limitation to the method (*NORSOK, 2004*) . Such method is further reviewed in the following section.

2.3. External Dynamics

The *external dynamics* account for the motion and dynamic response of the system in its environment as illustrated in Fig. 2.3.

As it can be seen in Fig. 2.3, this mechanism is governed by:

- Motion of the bodies;
- Water added mass effects;
- Damping hydrodynamic effects such as drag and wave radiation;
- Mooring lines interaction;

This dynamic response of the system can be computed by solving the resulting equation of

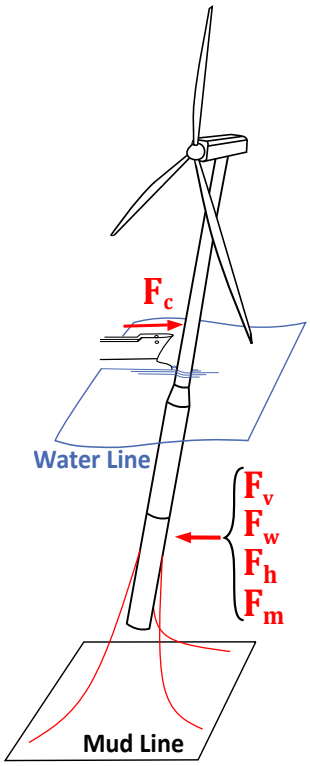

Figure 2.3.: External dynamics applied on a FOWT during a collision. *From: Ladeira et al., 2022*

motion (EOM) and the conservation of energy. As it can be seen on the Fig. 2.3, the motion of the bodies is governed by the contact force F_c. Therefore, the conservation of energy can be given as:

$$\begin{aligned} K_{\text{ext}} &= \int_0^t \boldsymbol{y}_s^T \boldsymbol{F}_{c,s}\, dt + \int_0^t \boldsymbol{y}_i^T \boldsymbol{F}_{c,i}\, dt \\ &= \int_0^t \boldsymbol{y}_s^T \boldsymbol{F}_{v,s}\, dt + \int_0^t \boldsymbol{y}_s^T \boldsymbol{F}_{w,s}\, dt + \int_0^t \boldsymbol{y}_s^T \boldsymbol{F}_{h,s}\, dt + \frac{1}{2}\, \boldsymbol{y}_s^T \mathbf{M}_s \boldsymbol{y}_s \\ &+ \int_0^t \boldsymbol{y}_i^T \boldsymbol{F}_{v,i}\, dt + \int_0^t \boldsymbol{y}_i^T \boldsymbol{F}_{w,i}\, dt + \int_0^t \boldsymbol{y}_i^T \boldsymbol{F}_{h,i}\, dt + \int_0^t \boldsymbol{y}_i^T \boldsymbol{F}_{m,i}\, dt + \frac{1}{2}\, \boldsymbol{y}_i^T \mathbf{M}_i \boldsymbol{y}_i \end{aligned} \tag{2.5}$$

Where $\boldsymbol{y}_s$ and $\boldsymbol{y}_i$ denote the velocity vectors in 6-DOFs of the ship and the FOWT respectively. The forces involved in the system include the contact force $\boldsymbol{F}_c$, the viscous damping force $\boldsymbol{F}_v$, the wave damping radiation force $\boldsymbol{F}_w$, the hydrostatic restoring force $\boldsymbol{F}_h$, and the force exerted by the mooring lines $\boldsymbol{F}_m$. The indices s and i indicate whether the force is applied on the ship or the FOWT. Additionally, $\mathbf{M}_s$ and $\mathbf{M}_i$ represent the combined mass matrix $\mathbf{M}_{RB}$ of the dry ship, resp. FOWT, and their respective water added mass matrix $\mathbf{M}_\infty$.

For better readability, the Eq. 2.5 can be rewritten as:

$$K_{ext} = K_{ship} + K_{fowt} + E_{hydro} \tag{2.6}$$

Where K_{ship} and K_{fowt} are the kinetic energies of the ship and the FOWT respectively and E_{hydro} is the total work done by the viscous drag damping forces, the wave radiation forces, the hydrostatic forces and the mooring lines forces.

Moreover, the EOM in 6-DOFs that describes the rigid-body motion of a body in water is given as:

$$\mathbf{M}\dot{\boldsymbol{y}} + \mathbf{G}\boldsymbol{y} - [\boldsymbol{F}_v(\boldsymbol{x}, \boldsymbol{y}) + \boldsymbol{F}_w(\boldsymbol{x}, \boldsymbol{y}) + \boldsymbol{F}_h(\boldsymbol{x}, \boldsymbol{y})] = \boldsymbol{F}(\boldsymbol{x}) \tag{2.7}$$

where $\mathbf{M}$ is the total mass matrix of the body defined by the sum of the dry mass matrix $\mathbf{M}_{RB}$ with its respective water added mass matrix $\mathbf{M}_{\infty}$ and $\mathbf{G}$ is the total gyroscopic matrix defined by the sum of the dry body gyroscopic matrix $\mathbf{G}_{RB}$ with its respective water added mass gyroscopic matrix $\mathbf{G}_{\infty}$. And where the forces involved in the system include the applied force $\boldsymbol{F}$, the viscous damping force $\boldsymbol{F}_v$, the wave radiation damping force $\boldsymbol{F}_w$, and the hydrostatic restoring force $\boldsymbol{F}_h$. Moreover, the vector $\boldsymbol{x}$ denotes the motion of the body in an earth fixed reference system and the vectors $\boldsymbol{y}$ and $\dot{\boldsymbol{y}}$ denote the velocity and acceleration, respectively, in a body-fixed reference system.

This EOM can also be solved by numerical simulation with CFD software for example or by simplified analytical method. However, with the later method, the computation of the equation is limited due to the hypothesis done to solve it. For example, this equation is generally solved with the assumption of small Froud number as well as small angle variation. Moreover, in a ship collision, it is commonly assumed that the water added mass matrix, damping matrix, and restoring matrix remain constant throughout the event, as the collision is considered as a momentary occurrence (*Le Sourne et al., 2012*) . Consequently, if a collision scenario involves prolonged contact between the ship and the FOWT, the computed results towards the end of the computation may not accurately reflect the actual physical behavior.

2.4. Coupling Approach

Now that the *internal mechanics* and *external dynamics* of the system have been overviewed, a method to bring each part of the Eq. 2.1 together needs to be defined. But first, this equation can be rewritten by substituting the terms in the right-hand side with the Eqs. 2.2 and 2.6 to define the most general equation for the energy conservation in a ship/FOWT collision, the equation rewrites as developed in *(Ladeira et al., 2022)* :

$$E_{tot} = K_0 = \underbrace{U_{ship} + U_{fowt}}_{\textit{Internal mechanisms}} + \underbrace{K_{ship} + K_{fowt} + E_{hydro}}_{\textit{External dynamics}} \tag{2.8}$$

Each term of this equation can be solved individually (the so-called *decoupled* approach), such approach does not work well in all the cases of ship/FOWT collisions: the internal mechanics terms are dependent on the penetration of the ship into the FOWT and the terms related to the external dynamics depend on the reaction force. That is why, in this context, a *decoupled* approach is not well suited as demonstrated by *Echeverry et al. (2019)* . Therefore, the *internal mechanisms* and *external dynamics* need to be coupled in order to capture the interaction between each contribution.

Two different approaches can be used to couple each term together. The first one is the so-called *semi-coupled* approach, while the second one is the *fully-coupled* approach. In the latter, both the structure and the fluid are modeled, enabling the computation of each term in Eq. 2.8 in relation to one another. Such approach can be implemented using numerical methods like CFD or Smoothed Particle Hydrodynamics (SPH), for example. However, the *fully-coupled* approach is not suitable for simplified analytical methods and becomes limited due to the associated computational costs of CFD.

The second approach is the *semi-coupled* approach. For the *semi-coupled* approach, two solvers are used sequentially, typically in a step-by-step iterative manner, to solve the response of the system. This approach is called *"semi-coupled"* because the two solvers are used sequentially where the inputs of a solver are the output of the other one. A code snippet is given in the Fig. 2.4 to explain a *semi-coupled* algorithm.

```
def Structural_solver(x, y, z, sigma, E)
    # compute the force from positional and mechanical parameter
    return F

def Dynamic_solver(F, rho)
    # compute the position base on a force and water density
    return x, y, z

sigma = 350         # setting some constant for yield strength,
E = 210             # young modulus, water density and initial
rho = 1025          # force
F[0] = 0
x[0], y[0], z[0] = Dynamic_solver(F[0], rho)
stoping_criterion = False    # Will be set to True to stop the algorithm

while not stoping_criterion:
    F[i] = Structural_solver(x[i], y[i], z[i], sigma, E)
    x[i+1], y[i+1], z[i+1] = Dynamic_solver(F[i], rho)

    if x[i+1] > 10:                          # if the body moved more than
        stoping_criterion = True             # 10m, the stopping criterion
                                             # is met -> stop.
    i += 1
```

Figure 2.4.: Example of a semi-coupled algorithm. In this code snippet, two solvers are defined, each one can either be run independently or in a semi-couple manner.

The *semi-coupled* approach can also be used in numerical simulations. One example of such application is the rigid-body dynamic solver MCOL (*Le Sourne et al., 2001*), which has been coupled with the NLFEA software LS-DYNA and used in the SE SHARP (*Le Sourne et al., 2012*) and FLAGS (*Pineau et al., 2022*) programs. This example illustrates the modularity enabled by such an approach. Moreover, this approach can provide a good compromise in terms of computational time and accuracy.

3. EXISTING SOLVERS

3.1. Introduction

Following the methodology outlined in Section 2, the ColFOWT algorithm is based on three distinct solvers. The first one, MCOL, computes the *external dynamics* of the bodies. As the MCOL solver had been developed in 2005 and tested since then, this solver is the best option in terms of reliability, accessibility and efficiency. The second solver is a structural solver that calculates internal interactions and deformation modes based on a SE approach. This solver has been developed and tested in *(Ladeira et al., 2023)*. Finally, the third solver is employed to compute the interaction of mooring lines with the structure, using the methodology proposed by *Marquez et al. (2022)* .

The ColFOWT algorithm is based on a *semi-coupled* approach with a quasi-static assumption for the internal mechanics modeling. Currently, the algorithm assumes that the striking ship is an infinitely rigid body, and therefore, the energy dissipated by the ship deformation is disregarded. Only the kinetic energy of the ship related to its rigid-body motion is considered. Additionally, the algorithm does not account for hydrodynamic forces that apply on the striking ship in the computation of *external dynamics*.

Having these assumption and simplification in mind, the Eq. 2.8 can be computed with a *semi-coupled* algorithm where each term is computed by its own solver:

- U_{ship}: Is not considered as the impactor is perfectly rigid;
- U_{fowt}: Is computed with the SE solver;
- K_{ship}: As the hydrodynamic effects of the ship are not considered, this energy can be obtained from the contact force resulting the impact;
- K_{fowt}: Is computed with the the MCOL solver;
- E_{hydro}: Is also computed with the MCOL solver (only the terms related to the FOWT);
- E_{moor}: Is neglected as this energy is relatively small.

Finally, it must be pointed out that the aim of this tool is not to replace Finite Element Analysis

(FEA) but rather to complement it. The main objective of this fast collision tool is to be used for risk assessment, damage probability or even optimization in early design process.

In this section, each solver is presented as a black box to understand its respective aim and how it can be integrated with the other ones. In the following subsections, the three solvers are then presented in more detail.

3.2. MCOL External Dynamics Solver

In a few words, the MCOL solver can be viewed as a black box that takes two inputs: (i) a file containing matrices describing the body mass and inertia and hydrodynamic properties (An example of such a file is provided in Appendix B), and (ii) the force resulting from the collision.

MCOL solves Eq. 2.7 to determine the acceleration, velocity, and displacement vectors ($\dot{\boldsymbol{y}}$, $\boldsymbol{y}$, and $\boldsymbol{x}$) of the body's center of gravity. Additionally, it computes the work done by the hydrostatic, wave, and viscous damping forces, as well as the total kinetic energy of the body denoted by E_h, E_w, E_v, and K_{body}, respectively (Additional outputs are provided by the MCOL solver, and more details can be found in *(Le Sourne et al., 2001)*. However the one listed are the ones of interest in this paper). A diagram illustrating the MCOL solver as a black box is presented in Fig. 3.1.

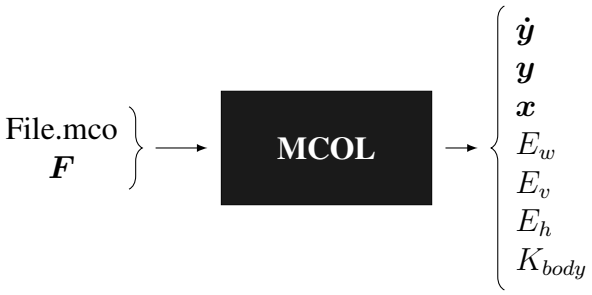

Figure 3.1.: Schematic representation of the MCOL solver as a black box.

In addition, it must be noted that the MCOL solver utilizes two reference systems. The first one is a body-fixed reference system with its origin located at the center of mass of the body. The second one is an earth-fixed reference system, established at the initial position of the body-fixed frame. The orientation of the axes is illustrated in Fig. 3.2.

Furthermore, the motion is defined by the translation of its center of mass from its initial position and by its roll, pitch and yaw (ϕ, θ, ψ).Therefore, the general motion of the body can be described

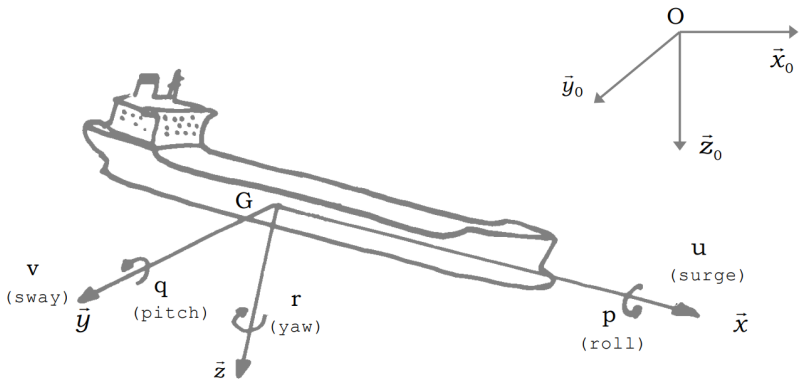

Figure 3.2.: Body-fixed and earth-fixed reference systems used in MCOL. *From: Le Sourne et al., 2001*

with the following convention:

$$\begin{aligned} \boldsymbol{x} &= (x_{OG}, y_{OG}, z_{OG}, \phi, \theta, \psi)^T \\ \boldsymbol{y} &= (u, v, w, p, q, r)^T \\ \boldsymbol{F} &= (X, Y, Z, K, M, N)^T \end{aligned} \tag{3.1}$$

where $\boldsymbol{x}$ denotes the position of the center of mass of the body in the earth-fixed reference system along with the Eulerian angles, $\boldsymbol{y}$ denotes the velocity of the body in the body-fixed reference system (the relationship between $\boldsymbol{x}$ and $\boldsymbol{y}$ is given in Eq. 3.2) and $\boldsymbol{F}$ denotes the forces and moments acting on the body relative to its center of mass.

$$\dot{\boldsymbol{x}} = \mathbf{J}\boldsymbol{y} \tag{3.2}$$

where $\mathbf{J}$ is the transformation matrix that relates the vector components from the body-fixed reference system to the earth-fixed reference system. More details on this matrix are given in (*Le Sourne et al., 2001*) .

Moreover, the EOM given in Eq. 2.7 is solved by taking into account the relationship between $\boldsymbol{x}$ and $\boldsymbol{y}$ as given in Eq. 3.2.

Finally, by solving the Eq. 2.7, the energies involved in the system can be computed such that:

$$\begin{cases} E_w = \int_0^t \boldsymbol{y}^T \boldsymbol{F_w}\, dt \\ E_v = \int_0^t \boldsymbol{y}^T \boldsymbol{F_v}\, dt \\ E_h = \int_0^t \boldsymbol{y}^T \boldsymbol{F_h}\, dt \\ K_{tot} = \frac{1}{2}\boldsymbol{y}^T \mathrm{M}_{\boldsymbol{RB}} \boldsymbol{y} + \frac{1}{2}\boldsymbol{y}^T \mathrm{M}_{\infty} \boldsymbol{y} \end{cases} \tag{3.3}$$

An illustration of the application of the MCOL solver is shown in Fig. 3.3. In this illustration, the MCOL solver is coupled with the nonlinear finite element code LS-DYNA. LS-DYNA is used to compute the contact force resulting from the collision of a ship (shown in red in the figure) with a submarine (shown in black in the figure). The resulting force is then passed to the MCOL solver, which solves the EOM and returns the motion of the ship and the submarine. As depicted in the illustration, there is no need to model the surrounding water in LS-DYNA, which helps saving computation time.

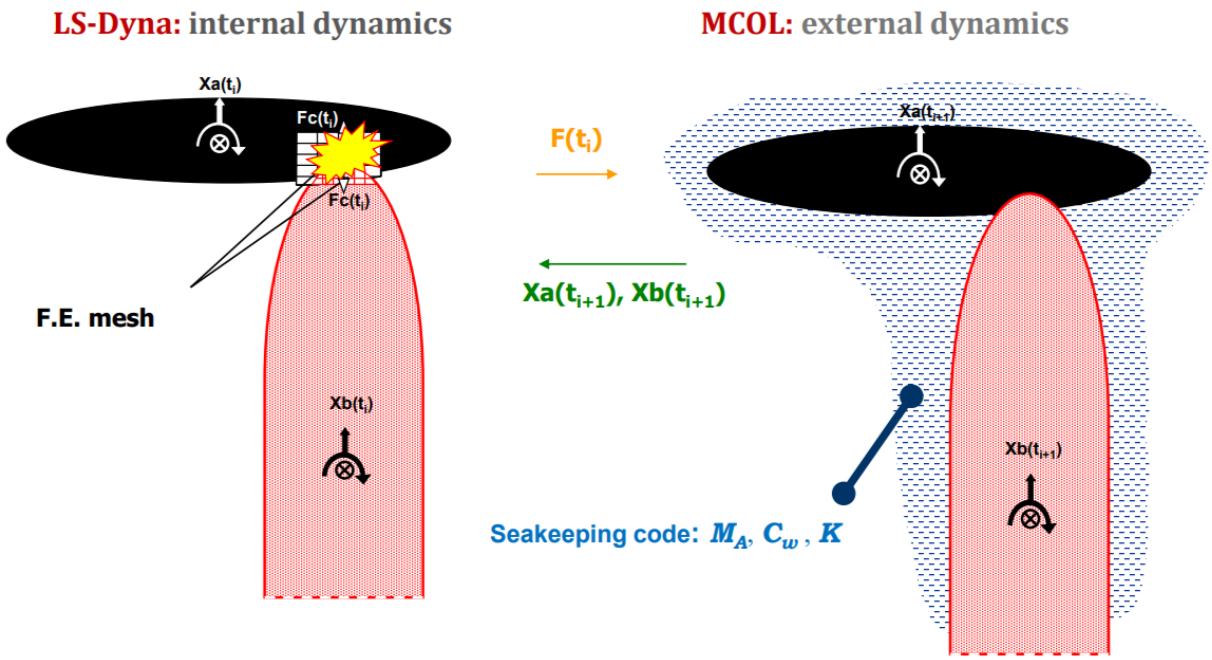

Figure 3.3.: Example of the application of MCOL. *From (Le Sourne et al., 2001)*

3.3. Super Element Solver

In a few words, the SE solver considers the geometries of the impactor and the tube used to describe the FOWT, as well as the velocity vector $\boldsymbol{y}$ that describes the motion of the FOWT. It then returns the contact force vector $\boldsymbol{F}$, the penetration of the impactor into the tube δ, and the

energy of deformation in the tube U_{int}. A diagram illustrating the SE solver as a black box is provided in Fig. 3.4.

Figure 3.4.: Schematic representation of the SE solver as a black box.

In more details, during each iteration, the resistance force of the tube $\boldsymbol{F}$, is computed as a function of the penetration of the ship into the tube, δ. This penetration can be computed by taking the variation of the impactor displacement relatively to the tube displacement. Through a series of simulations, *Ladeira et al. (2023)* identified three distinct deformation phases and derived separate analytical formulae to compute the resistance force for each phase of deformation. The proposed solver has then been extended to FOWT but the three phases of deformation remain the same:

- *Phase I*: Local elastic indentation at the contact zone;
- *Phase II*: Local plastic indentation;
- *Phase III*: Buckling mechanism at the base of the tube (Elephant foot deformation mechanism).

However, it must be pointed out that in reality, the separation between each phase is not strictly delimited, and some overlapping of phases can be observed in the numerical simulations. In the current approach, the transition between two phases is well-defined and triggered by a threshold value calculated at the beginning of the routine and based on the geometry and properties of the tube. These values are further explained in the following sections.

Moreover, with this approach, the support of the FOWT is idealized as a cantilever tube with a constant average cross-section, and a lumped mass is placed at the upper free extremity of the tube to represent the Rotor Nacelle Assembly (RNA). Additionally, the impact is always assumed to occur at mid-length of the tube. Fig. 3.5 illustrates the idealization of the FOWT in the SE solver.

A summary of the SE solver adapted for a FOWT is given in the following subsections. Moreover, a schematic diagram explaining the SE algorithm is given in the Appendix C. For detailed explanations, please refer to *(Ladeira et al., 2023)* .

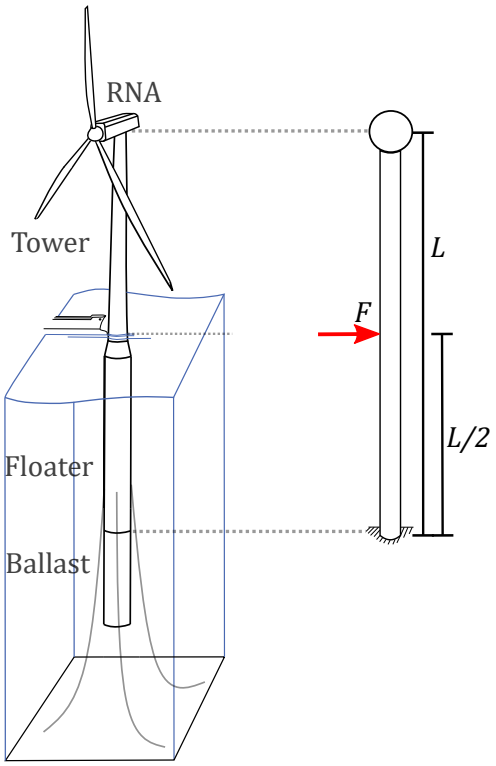

Figure 3.5.: Representation of the FOWT in the SE solver. *From (Ladeira, 2023)*

Phase I - Local Elastic Denting

The local elastic denting mechanism in *Phase I* is computed under the assumption that the tubular member can be approximated as a cylindrical thin-walled shell subjected to a pair of diametrically opposed concentrated loads *(Ting & Yuan, 1958)* . This simplification is depicted in Fig. 3.6.

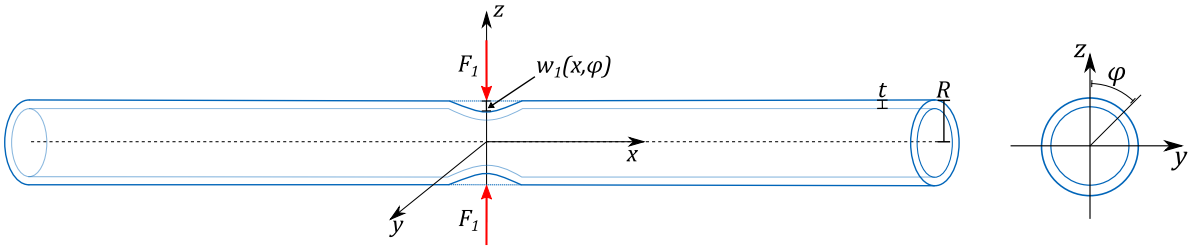

(a) Side view. (b) Cross-section.

Figure 3.6.: Local elastic denting mode subjected to two diametrically opposed concentrated loads. *From: Ladeira et al., 2023*

In the cylindrical coordinate system (r, φ, x), consider the radial displacement $w_1(x, \varphi)$ of the tubular member under the influence of a collision force, as illustrated in Fig. 3.6. A closed-form solution can be obtained by expressing the general differential equation in the form of a Fourier series. At the impact point, corresponding to the loaded cross-section ($x = 0$), the radial

displacement is given by:

$$w_1(0,\varphi) = 1.117\frac{F_1 R^3}{B_r R\sqrt{\frac{R}{t}}} \sum_{n=2(i+1)}^{\infty} \left(\frac{t}{R}\frac{\cos(n)}{A_n}\right) \tag{3.4}$$

where F_1 is the local elastic denting load, R is the mean radius of the tube and t is its thickness. Coefficients A_n are dependent on the geometry of the tube. The parameter B_r denotes the ring bending stiffness of the tube wall per unit of length under plane strain conditions:

$$B_r = \frac{Et^3}{12(1-\nu^2)} \tag{3.5}$$

where E and ν denote the material Young modulus and Poisson coefficient respectively.

Assuming that the local indentation is twice the displacement $\delta_{loc} = 2w_1(0,0)$ at the load application (as depicted in Fig. 3.7), Eq. 3.4 can be rewritten in terms of the local elastic resistance force F_1 as a function of local indentation δ_{loc} (For further details on the development of this equation, please refer to *(Ting & Yuan, 1958)* :

$$F_1(\delta_{loc}) = 8.928\left(\frac{B_r\sqrt{\frac{R}{t}}}{R^2}\right)\delta_{loc} \tag{3.6}$$

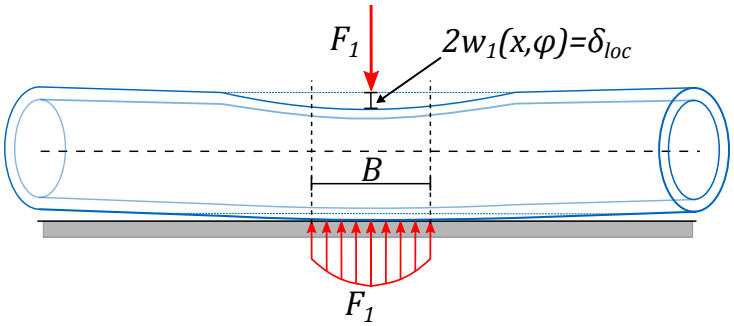

Figure 3.7.: Local elastic denting mode subjected to one concentrated loads. *From (Ladeira et al., 2023)*

Finally, the threshold for the local elastic denting mechanism is defined by the characteristic collapse resistance of the tube wall. Thus, *Phase II* is triggered once $F_1 \geq F_1^c$, where F_1^c is calculated as:

$$F_1^c = \sigma_y \frac{t^2}{4}\sqrt{\frac{D}{t}} \tag{3.7}$$

where σ_y is the yield strength, D is the tube diameter and t its thickness .

Phase II - Local Plastic Denting

Phase II consists of a combination of local plastic denting and global beam-like elastic bending. These mechanisms are strongly coupled and interact through a highly non-linear dynamic that appears to be particularly sensitive to the tube characteristic geometry, the impact location and the impactor kinetic energy. However, in the case of an impact at mid-length of the tube, the global beam-like elastic bending can be neglected as its contribution to the resistant force is relatively small compared to the local plastic denting. In addition, neglecting the global elastic bending allows the computed force to be more conservative.

The mathematical model used to compute the resistance of local plastic denting is based on the formulation developed by *Buldgen et al. (2014)* for the local crushing resistance of tubular jacket members. It employs plastic limit analysis and assumes that the tube is composed of a rigid-perfectly plastic material with a flow stress σ_0. The resistance is determined by applying the upper bound theorem *(Jones, 2011)* to a predefined displacement field that approximates the expected deformation pattern for this mechanism, as illustrated in Fig. 3.8.

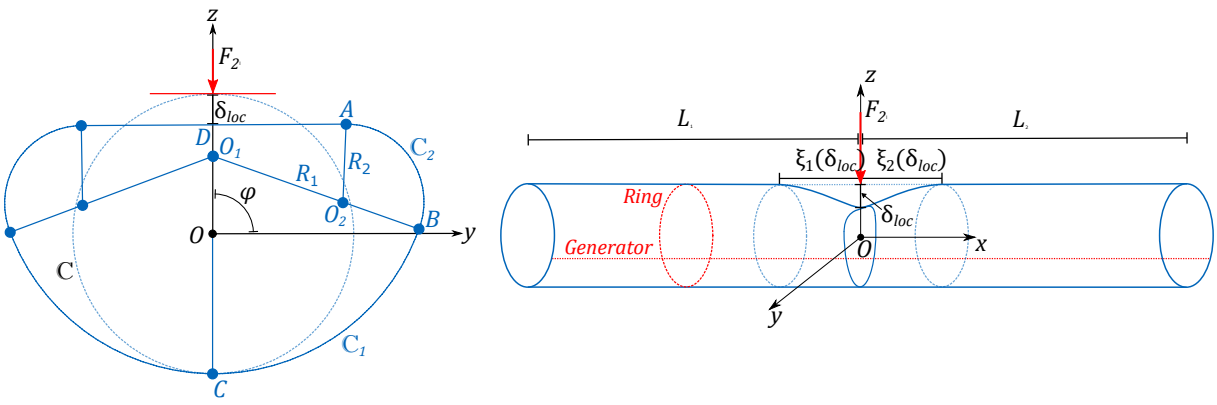

(a) Cross-section view.

(b) Side view.

Figure 3.8.: Definition of the displacement field for *Phase II*. *From (Ladeira et al., 2023)*

The first step is to define the displacement field. A suitable approach, proposed by *Wierzbicki & Suh (1988)* , assumes that the tube consists of a series of generators supported by independent rings. These rings are allowed to slide freely along the generators without any shear resistance, as illustrated in Fig. 3.8b. The total deformation energy rate, denoted as $\dot{E}_2$, can then be computed by summing the energy rates of the rings and the generators, denoted as $\dot{E}_{2r}$ and $\dot{E}_{2g}$ respectively:

$$\dot{E}_2 = \dot{E}_{2r} + \dot{E}_{2g} \tag{3.8}$$

Given the *Virtual Velocity Principle (Jones, 2011)*, it is possible to obtain the following

force-penetration relationship:

$$F_{2l}(\delta_{loc}) = \frac{1}{\dot{\delta}_{loc}} \left[\dot{E}_{2b} \frac{\xi_1 + \xi_2}{2} + \left(\frac{1}{\xi_1} + \frac{1}{\xi_2} \right) \dot{E}'_{2m} \right] \tag{3.9}$$

where $\dot{E}_{2b}$ denotes the energy rate related to both the change in curvature and bending of the plastic hinges that develop in the ring-like indented cross-section, $\dot{E}'_{2m}$ denotes the energy rate related to membrane deformation along the generators, and $\dot{\delta}_{loc}$ denotes the local penetration rate. By minimizing the resistant force given by Eq. 3.9, the parameters ξ_1 and ξ_2 can be obtained as:

$$\xi_1 = \min \left(\sqrt{\frac{2E'_{2m}}{E_{2b}}}, L_1 \right); \quad \xi_2 = \min \left(\sqrt{\frac{2E'_{2m}}{E_{2b}}}, L_2 \right) \tag{3.10}$$

where E'_{2m} and E_{2b} are calculated such that:

$$E'_{2m} = \frac{\dot{E}'_{2m}}{\dot{\delta}_{loc}} \tag{3.11}$$

$$E_{2b} = \frac{\dot{E}_{2b}}{\dot{\delta}_{loc}} \tag{3.12}$$

In order to maintain continuity between *Phase I* and *Phase II*, a correction coefficient is used. This coefficient is given as the characteristic collapse resistance of the tube wall F_1^c divided by the values of $F_{2l}(\zeta_1)$ where ζ_1 is the penetration for which $F_1(\zeta_1) = F_1^c$, ie. the critical penetration for which the *Phase II* is triggered. Mathematically, this gives:

$$C = \frac{F_1^c}{F_{2l}(\zeta_1)} \tag{3.13}$$

Using this coefficient, the resulting force F_2 for *Phase II* is thus calculated as:

$$F_2(\delta_{loc}) = F_{2l}(\delta_{loc})C \tag{3.14}$$

The transition to *Phase III* occurs when the plastic collapse load of the cantilever tube F_2^c is reached ($F_2 \geq F_2^c$). The value of F_2^c is given by:

$$F_2^c = \frac{D^2 t \sigma_0}{L_1} \tag{3.15}$$

Phase III - Elephant Foot Buckling

The deformation during the "elephant foot" asymmetric buckling, ie. in *Phase III*, occurs at the base of the tube, where the compressed region undergoes successive folding. *Pire (2018)* proposed a semi-analytical methodology to evaluate the resistance force associated with a comparable mechanism observed in jacket foundations subjected to ship impacts. A plastic limit analysis is conducted following an approach similar to the one used for assessing local plastic denting.

The displacement field is determined based on the geometry depicted in Fig. 3.9. Following a similar approach to the local plastic denting methodology in *Phase II*, the tube is idealized as a composition of rings and generators.

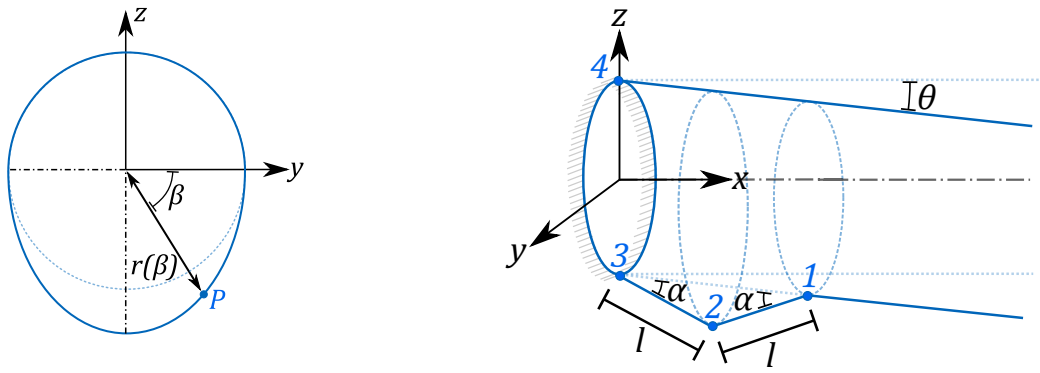

(a) Cross-section view.

(b) Side view.

Figure 3.9.: Schematic representation of the displacement fields defined for the deformation pattern at the base of the tube. *From (Ladeira et al., 2023)*

The deformation process consists of the following mechanisms: three plastic hinges (numbered 1, 2, and 3 in Fig. 3.9b) that develop as a consequence of the folding of the generators, the elongation of the rings located between hinges 1 and 3, which introduces membrane strain in the cross-section, and a fourth plastic hinge (numbered 4 in Fig. 3.9b) that develops at the clamped base on the non-folded side of the tube due to its overall rotation.

The total energy rate due to the deformation, $\dot{E}_3$, is obtained by summing the energy rates associated with deformation at the hinges ($\dot{E}_3^{h1}$, $\dot{E}_3^{h2}$, $\dot{E}_3^{h3}$, $\dot{E}_3^{h4}$) and the membrane effects at the generators ($\dot{E}_3^{m}$):

$$\dot{E}_3 = \dot{E}_3^{h1} + \dot{E}_3^{h2} + \dot{E}_3^{h3} + \dot{E}_3^{h4} + \dot{E}_3^{m} \tag{3.16}$$

Finally, the *Virtual Velocity Principle* can be applied to the total energy rate given by Eq. 3.16

to define the resistance force F_3 for a given penetration rate $\dot{\delta}$ such as:

$$F_3 = \frac{\dot{E}_3}{\dot{\delta}} \tag{3.17}$$

In summary, regarding the SE solver, Fig. 3.10a presents an example of the force-penetration diagram where the threshold that separates each phase can be seen. The parameter ζ_1 is defined such that $F_1(\zeta_1) = F_1^c$, and similarly, ζ_2 is defined such that $F_2(\zeta_2) = F_2^c$. Furthermore, it is worth noting that the penetration δ represents the overall displacement of the impactor with respect to the tube initial position. Consequently, this penetration can be divided into two components: the overall penetration δ and the local penetration δ_{loc}. The local penetration δ_{loc} is calculated during *Phase I* and *Phase II* and remains constant in *Phase III*, as depicted in Fig. 3.10b.

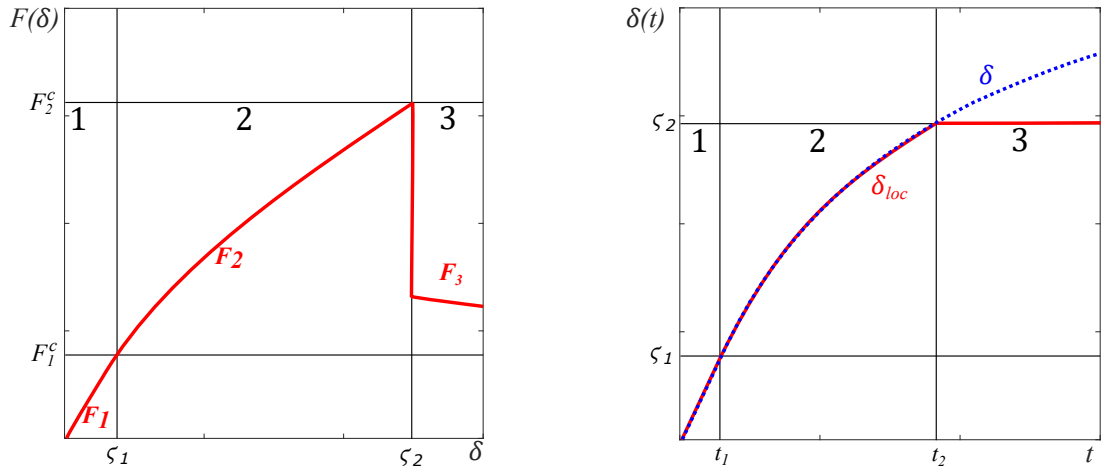

(a) Force-penetration diagram.

(b) Penetration-time diagram.

Figure 3.10.: Example of force-penetration and penetration-time diagram computed with the SE solver.

3.4. Moorline Solver

In a few words, the Moorline solver computes the forces exerted at the fairlead point of a mooring line. This solver was developed by *Marquez et al., (2022)* , building upon the work of *Jonkman (2007)* . The solver takes as inputs the parameters of the mooring lines and the displacement of the FOWT at its CoG. Subsequently, it determines the forces acting at the fairlead point. A diagram illustrating the Mooring solver as a black box is presented in Fig. 3.11.

In more detail, each mooring line is characterized by its length L, linear apparent weight in water w, Young modulus E, sectional area A, and the seabed static-friction drag coefficient C_B.

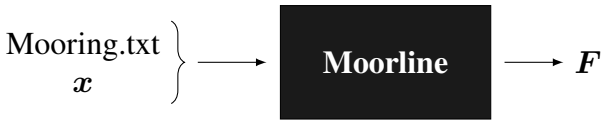

Figure 3.11.: Schematic representation of the Moorline solver as a black box

Since a mooring line is buoyant, w can be defined as follows:

$$w = (\mu - \rho A)\, g \tag{3.18}$$

where μ, ρ and g denote the linear mass of the mooring line, the water density and the gravitational acceleration, respectively.

Moreover, the mooring line is characterized by the horizontal distance x_F and vertical distance z_F between its fairlead and anchor points, as illustrated in Fig. 3.12, where V_F, H_F and V_A, H_A denote the vertical and horizontal forces, respectively. The subscripts F and A indicate whether the force is applied at the fairlead point or at the anchor point.

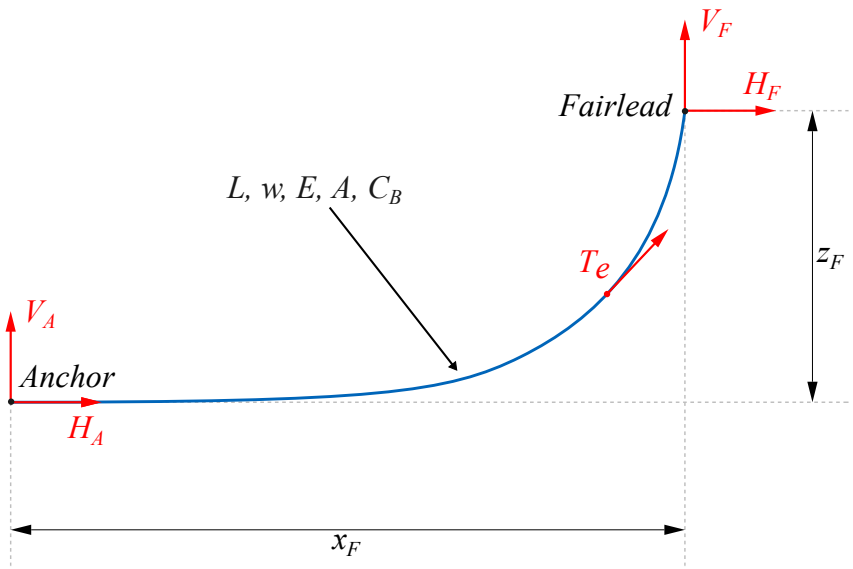

Figure 3.12.: Mooring line description in local reference system

In the Moorline solver, the position of the fairlead point is defined based on a transformation from the global to local reference system by computing the motion of the input $\boldsymbol{x}$ relative to the initial position at $t = 0$. Following the approach used by *Jonkman (2007)* , two sets of equations are defined: the first set applies when the mooring line does not lie on the seabed, and the second applies when a portion of the mooring line lies on the seabed. In both cases, the equations are nonlinear, and therefore, a *Newton-Raphson* iteration scheme is employed to solve

them. Additionally, the portion of the mooring line that lies on the seabed is defined as follows:

$$L_B = L - \frac{V_F^0}{w} \quad \begin{cases} \leq 0 & \text{Not laying on seabed} \\ > 0 & \text{Laying on seabed} \end{cases} \tag{3.19}$$

where V_F^0 is the value computed during the previous iteration for the vertical force at the fairlead point. Moreover, for the first iteration, this value is guessed based on the documentations in *Peyrot & Goulois (1979)* .

In the case where $L_B \leq 0$, the set of equations to solve are given as:

$$x_F(H_F, V_F) = \frac{H_F}{w}\left[\sinh^{-1}\left(\frac{V_F}{H_F}\right) - \sinh^{-1}\left(\frac{V_F - wL}{H_F}\right)\right] + \frac{H_F L}{EA} \tag{3.20a}$$

$$z_F(H_F, V_F) = \frac{H_F}{w}\left[\sqrt{1 + \left(\frac{V_F}{H_F}\right)^2} - \sqrt{1 + \left(\frac{V_F - wL}{H_F}\right)^2}\right] + \frac{2V_F L - wL^2}{2EA} \tag{3.20b}$$

And the forces at the anchor point are computed such that:

$$H_A = H_F \tag{3.21a}$$

$$V_A = V_F - wL \tag{3.21b}$$

In the case where $L_B > 0$, the set of equations to solve are given as:

$$\begin{aligned} x_F(H_F, V_F) = {} & L - \frac{V_F}{w} + \frac{H_F}{w}\sinh^{-1}\left(\frac{V_F}{H_F}\right) + \frac{H_F L}{EA} \\ & + \frac{C_B w}{2EA}\left[-\left(L - \frac{V_F}{w}\right)^2 + \left(L - \frac{V_F}{w} - \frac{H_F}{C_B w}\right)\max\left(L_B - \frac{H_F}{C_B w},\ 0\right)\right] \end{aligned} \tag{3.22a}$$

$$z_F(H_F, V_F) = \frac{H_F}{w}\left[\sqrt{1 + \left(\frac{V_F}{H_F}\right)^2} - \sqrt{1 + \left(\frac{V_F - wL}{H_F}\right)^2}\right] + \frac{2V_F L - wL^2}{2EA} \tag{3.22b}$$

And the forces at the anchor point are computed such that:

$$H_A = \max\left(H_F - C_B w L_B,\ 0\right) \tag{3.23a}$$

$$V_A = 0 \tag{3.23b}$$

Finally, the forces are converted from the local reference system to the global reference system, and the moments are computed based on the global reference system and the position of the

fairlead point within it.

A diagram explaining the Moorline algorithm in more details is given in Appendix D.

4. COUPLING OF THE SOLVERS

4.1. Introduction

The work presented in this section and in the following one has been performed during the master thesis.

This section is dedicated to the description of the algorithm and the coupling of the solvers described in the previous section. As most of the solvers described in Section 3 are coded in MATLAB, this algorithm is also developed in MATLAB for a better versatility. However, some of these solvers are developed using a Procedural Programming (PP) architecture which is not suitable when working in bigger and more complex project. Therefore, most of the solver had to be converted to an Object Oriented Programming (OOP) architecture which is better suited for the ColFOWT algorithm.

In this section, the algorithm is described step-by-step.

4.2. Definition of the Hypotheses

For the coupling of each solver described in Section 3, the following assumptions are made:

- Gravity is not applied on the system (the gravitational acceleration is used only to compute the linear apparent weight in water of the mooring lines);
- The impact is represented as a punctual force strictly in y direction (as a result of the ship moving strictly in y direction in the global reference system, refer to Fig. 4.1 for the axis orientation);
- The impact point is located at mid-length of the FOWT tower;
- The hydrodynamics loads acting on the ship are not taken into account;
- The base of the FOWT (denoted by the ballast on Fig. 4.1) is considered as rigid.

Moreover, different reference systems are used throughout the algorithm and are define as follows:

- $(O, x_0,\ y_0,\ z_0)$: Earth-fixed reference system, define at the initial position of the FOWT's CoG;
- $(F, x_{fowt},\ y_{fowt},\ z_{fowt})$: FOWT reference system, define at the CoG of the FOWT;
- $(S, 0,\ y_s,\ 0)$: Ship reference system, define at the CoG of the ship;
- $(M_j, x_{m,j},\ y_{m,j},\ z_{m,j})$: Mooring line reference system where j denotes the number of the mooring line, define at the fairlead point of the mooring line.

A schematic diagram is given in Fig. 4.1 to resume these notations and give an overview of each reference system used in this study.

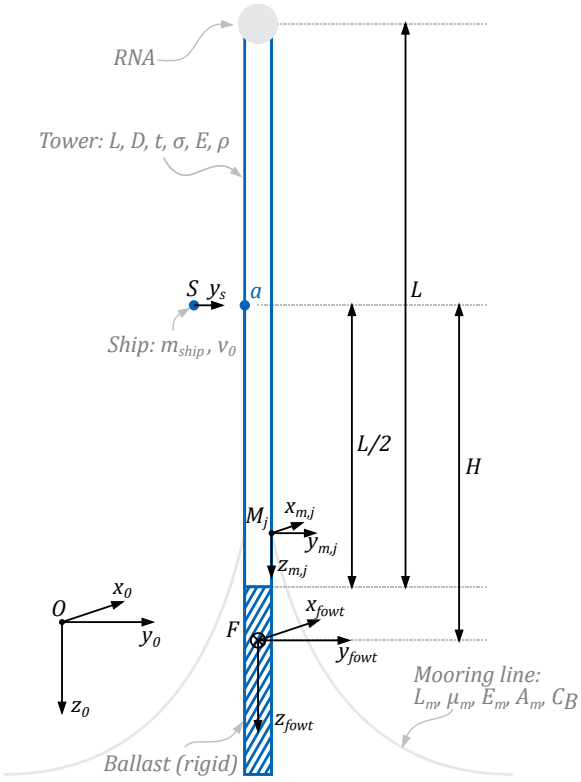

Figure 4.1.: Overall description of the system solved by the ColFOWT algorithm.

4.3. Step-by-Step Algorithm

Step 1

The first step is the initialization of the parameters and variables. The algorithm is based on an OOP architecture. Therefore, the Ship, FOWT, Moorline and MCOL objects are created. By default, only one Ship and one FOWT object can be created, however, the Moorline object can

be created as many times as required. Then, the MCOL object groups the Ship, FOWT and Moorline objects and defines the reference systems as described in Fig. 4.1.

Moreover, the initial values of the energies are computed such that:

$$E_{tot} = K_{ship} = \frac{1}{2} m_{ship} v_0^2, \quad U_{fowt} = K_{ship} = E_{hydro} = 0 \tag{4.1}$$

and the initial force and penetration are set to zero.

Finally, the MCOL solver is used to establish the $\boldsymbol{x}$ and $\boldsymbol{y}$ vectors required in *Step 2* and *Step 3*, respectively. Completing *Step 1* and the first iteration.

Step 2

During the second step, a loop iterates through each mooring line and calculates their respective resisting forces using the Mooring solver. These forces are subsequently computed in the earth-fixed reference system, and the corresponding moments with respect to the center of gravity of the FOWT are calculated as well.

Step 3

The *Step 3* invokes the SE solver. However, since the SE solver is designed for fixed cantilever tubes, some corrections need to be made regarding the computation of the penetration δ of the ship into the structure. Initially, the latter is defined as the ship position relative to the base of the tube. In the case of a FOWT, both the rigid-body translation and rotation of the tower at the impact point need to be deduced from the overall displacement of the ship. Fig. 4.2 illustrates geometrically how the penetration is computed. In this figure, the penetration at instant t represents the distance between points a and S_t.

Mathematically, the penetration is computed as:

$$\delta^i = \delta^{i-1} + (v^i_{ship} - v^i_a)\Delta t \tag{4.2}$$

where Δt is the time step and v_a is the velocity of the FOWT at point a (initial impact point) such that:

$$v^i_a = v^{i-1} + \sin p^{i-1} H \tag{4.3}$$

where v is the FOWT sway velocity and p its roll velocity (i.e. the angular velocity around the

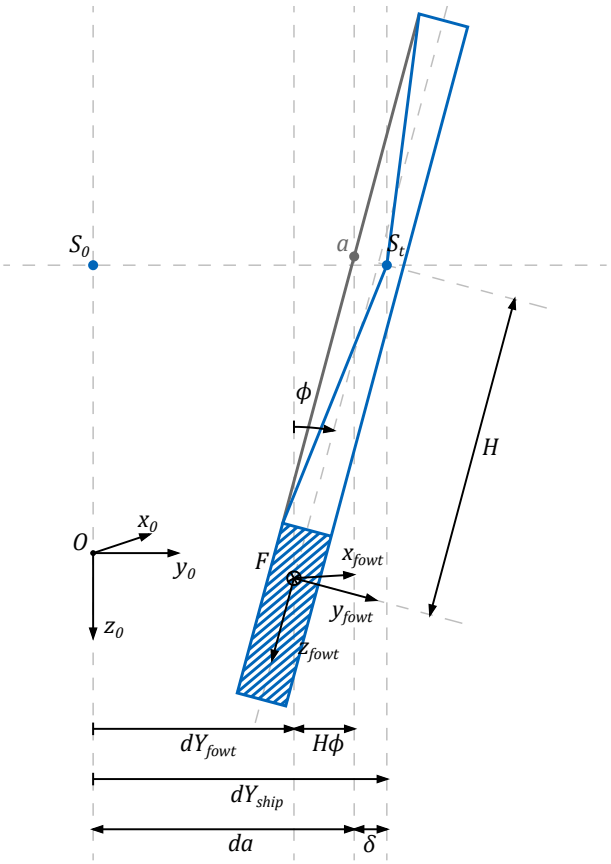

Figure 4.2.: Computation of the penetration δ geometrically.

x_{fowt} axis) as defined in Eq. 3.1. H is the vertical distance between the CoG of the FOWT and its impact point.

However, it should be noted that the penetration computed during *Phase III* does not represent the actual indentation of the FOWT's tower, as illustrated in Fig. 4.3. The additional penetration which occurs during *Phase III* is in fact the plastic bending deflection of the beam-like tower (calculated at the impact point) due to the "elephant foot" mechanism that occurs just above the ballast. In *Phase I* and *Phase II*, $\delta = \delta_{\text{loc}}$ represents the distance between point a and s in Fig. 4.3. In *Phase III*, the overall penetration δ is the distance between point a and s, while the local penetration δ_{loc} remains the distance between point a' and s, as depicted in Fig. 4.3.

Moreover, the current ship velocity v_{ship} is computed such that:

$$v_{ship}^{i} = v_{ship}^{i-1} - \frac{F_c^{i-1}}{m_{ship}} \Delta t \tag{4.4}$$

Then, the FOWT resisting force is computed using the SE solver as described in Sec. 3.3.

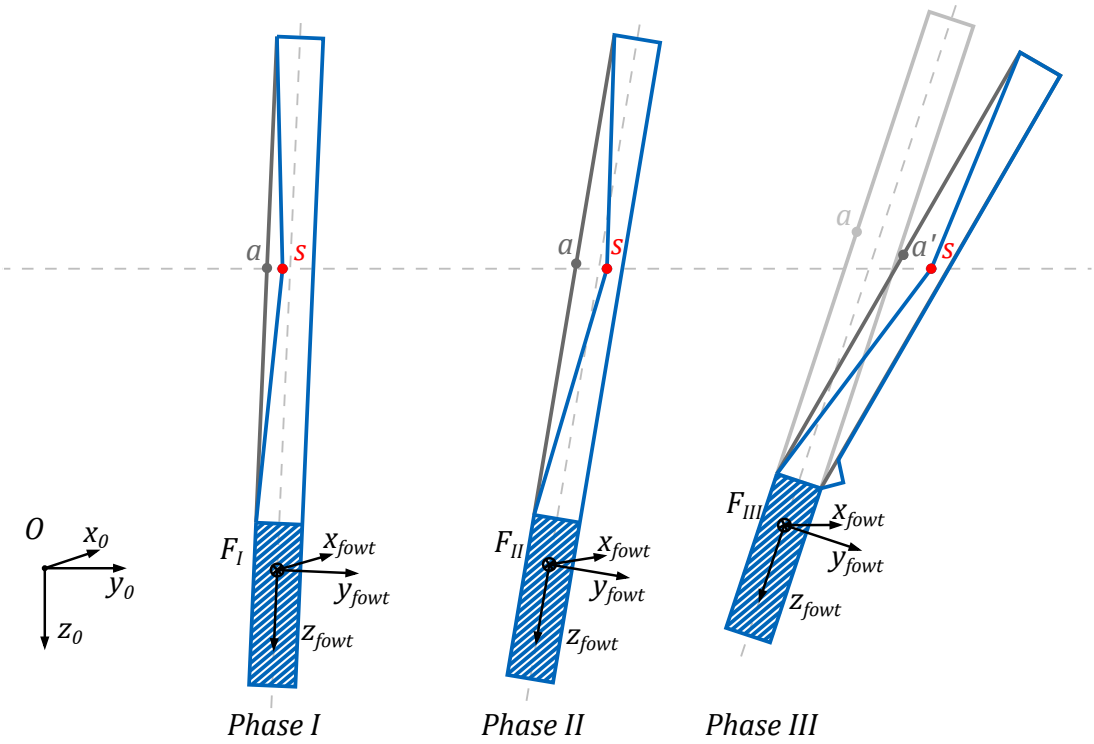

Figure 4.3.: Scheme illustrating the deformation of the FOWT in each phase.

Step 4

Step 4 consists of summing the forces computed in *Step 2* and *Step 3* and correcting the force vector, such that:

$$\boldsymbol{F}^i = \sum_j \left(\boldsymbol{F}^i_{\boldsymbol{m,j}} - \boldsymbol{F}^*_{\boldsymbol{m,j}} \right) + F^i_c \boldsymbol{h} \tag{4.5}$$

where $\boldsymbol{h} = (0, 1, 0, H, 0, 0)^T$ is the force direction vector, and $\boldsymbol{F}^*_{\boldsymbol{m,j}}$ is the mooring line correction force vector such that:

$$\boldsymbol{F}^*_{\boldsymbol{m,j}} = (0, 0, F^{z,0}_{m,j}, 0, 0, 0)^T \tag{4.6}$$

where $F^{z,0}_{m,j}$ represents the initial vertical force component of mooring line j at time $t = 0$.

This vertical component of the force at time $t = 0$ needs to be removed because the tension in the mooring line is computed based on its weight. Therefore, including this term acts as an "added weight" on the FOWT, which is not realistic. In practice, the presence of this "added weight" would alter the waterline of the FOWT. Consequently, either, one would remove some ballast to counterbalance this additional weight, or, the FOWT would oscillate until it reaches a new equilibrium waterline. Fig. 4.4 compares the results obtained for the FOWT vertical displacement and for the force exerted by the mooring lines, considering or not the initial

vertical force exerted by the mooring line.

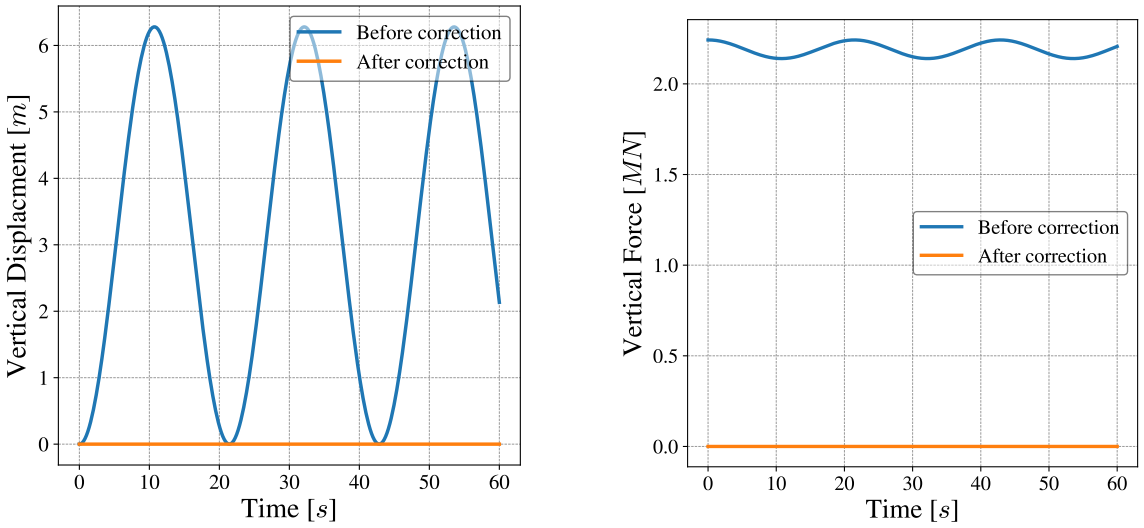

(a) Vertical motion of the FOWT.

(b) Vertical force applied at the CoG of the FOWT.

Figure 4.4.: Comparison between the inclusion or not of the vertical component of the mooring line force. (These results have been achieved disregarding the ship impact force and neglecting in MCOL calculation the wave radiation and drag damping forces)

As can be seen in Fig. 4.4a, prior the correction, the FOWT oscillates around its new waterline $3\ m$ below its initial position. On the other hand, after the correction, no disturbance from the mooring line can be observed, which is more realistic.

Step 5

During *Step 5*, the MCOL solver is activated considering the external force computed in *Step 4*.

Step 6

In *Step 6*, the FOWT deformation energy is computed by integrating the resisting force-penetration curve and the kinetic energies of both the ship and the FOWT are updated.

The total work of the hydrodynamic forces writes:

$$E^i_{hydro} = E^i_w + E^i_v + E^i_h \tag{4.7}$$

where E^i_w, E^i_v, E^i_h are computed by MCOL as defined in Eq. 3.3. The kinetic energy of the FOWT is also computed by MCOL.

The deformation energy of the FOWT is computed from the force-penetration curve using a trapeze integration scheme such that:

$$U_{fowt}^{i} = U_{fowt}^{i-1} + \left(\frac{F_c^{i-1} + F_c^{i}}{2} \right) \Delta\delta \tag{4.8}$$

where $\Delta\delta$ is the penetration increment given as:

$$\Delta\delta = (v_{ship}^{i} - v_{a}^{i})\Delta t \tag{4.9}$$

Lastly, the kinetic energy of the ship is computed such that:

$$K_{ship}^{i} = \frac{1}{2} m_{ship} \left(v_{ship}^{i} \right)^2 \tag{4.10}$$

Step 7

The *Step 7* concludes the algorithm by evaluating the stopping criterion. The variations in velocity and penetration are computed for iteration $i + 1$, and the stopping criterion is defined as follows: if $v_{\text{ship}}^{i+1} \leq 0$, the ship kinetic energy is zero, indicating that the ship has transferred all of its energy to the FOWT. Alternatively, if $\Delta\delta \leq 0$, the FOWT velocity at point a exceeds the ship velocity, indicating a loss of contact between the ship and the FOWT.

If one or both of these conditions are satisfied, the program terminates. Otherwise, the current time is incremented as follows:

$$t^{i+1} = t^{i} + \Delta t \tag{4.11}$$

and the next iterations starts from *Step 2*.

Fig. 4.5 illustrates a schematic diagram of the complete algorithm.

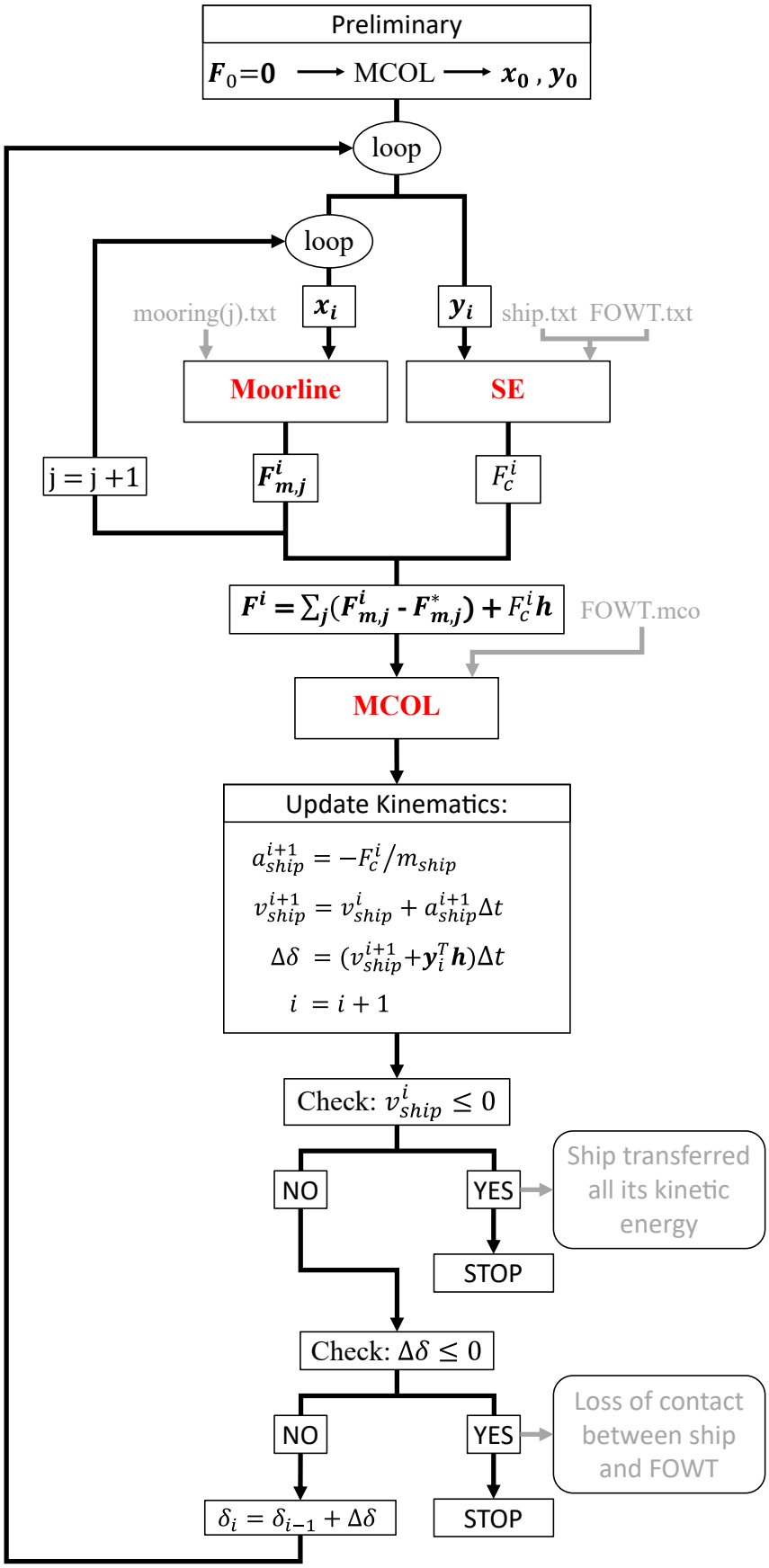

Figure 4.5.: Schematic diagram of the ColFOWT algorithm.

5. VALIDATION OF THE COUPLING

5.1. Introduction

To validate the developed tool, non-linear finite element simulations are performed using the commercial software LS-DYNA along with the MCOL solver, using the *BOUNDARY_MCOL card in LS-DYNA datafile. Furthermore, as discussed in Appendix E, the version R711 of LS-DYNA is used due to some issues identified in the latest version (version R13). In order to have realistic numerical simulations, the OC3-Hywind FOWT, well documented in literature, is considered for this validation. Additionally, the data used to model this platform are extracted from an NREL report by *Jonkman et al. (2010)*. The main particulars of the OC3-Hywind FOWT are given in Fig. 5.1 and Tab. 5.1.

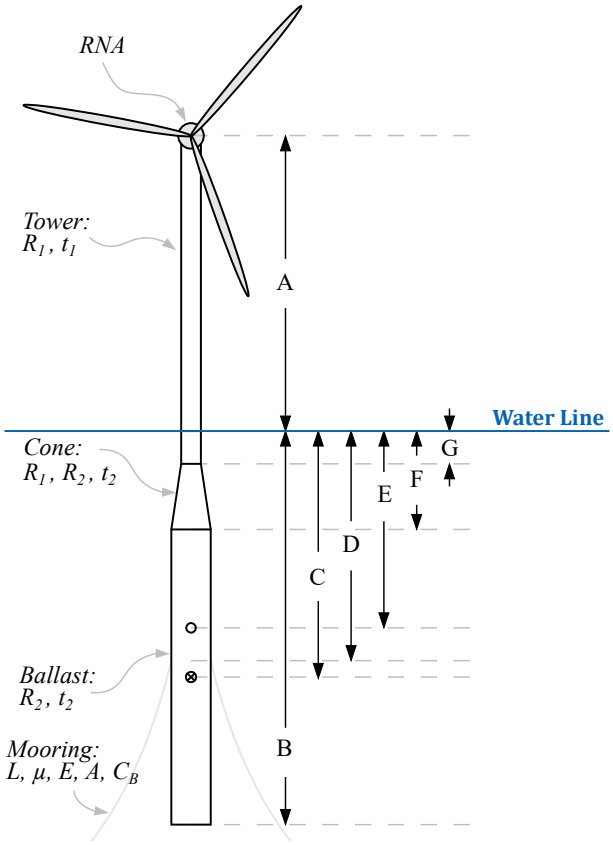

Figure 5.1.: Diagram with the main dimensions of the OC3-Hywind.

Table 5.1.: Main particulars of the OC3-Hywind.

Structure	Notation	Position $[m]$
Water depth	-	320
Tower top	A	90
Spar depth	B	120
Center of Gravity	C	78
Mooring location	D	70
Center of Buoyancy	E	62.7
Taper bottom	F	12
Taper top	G	4

Moreover, structural properties of the OC3-Hywind are given in Tab. 5.2 and mooring lines characteristics are given in Tab. 5.3.

Table 5.2.: Structural properties of the OC3-Hywind.

Property	Notation	Value	Unit
Mass of the RNA	M_{RNA}	350	$tons$
Tower radius	R_1	3.25	m
Ballast radius	R_2	4.7	m
Tower thickness	t_1	23	mm
Ballast thickness	t_2	27	mm
Density	ρ	8500	kg/m^3
Yield strength	σ_y	255.7	MPa
Young's modulus	E	210	MPa

Table 5.3.: Properties of the mooring lines.

Property	Notation	Value	Unit
Number of moorling lines	n_m	4	-
Length	L_m	900	m
Linear mass	μ_m	77.7	kg/m
Young's modulus	E_m	48.9	GPa
Sectional area	A_m	78.5	cm^2
Seabed frictional coefficient	C_B	1	-
Anchor-Fairlead horizontal distance	x_F	850.4	m
Anchor-Fairlead vertical distance	z_F	250	m

To avoid redundancy, the results presented in this paper represent only a selection of the numerical simulations performed to validate the developed tool. In practice, various collision scenarios involving different length, diameter, thickness, density, Young's modulus, yield stress, ship mass, and ship initial velocity have been investigated. However, the center of gravity, center of buoyancy, mooring location, inertia, and mass of the OC3-Hywind remain constant in all the simulations to keep the initial properties of the platform. Generally, similar results in terms of discrepancies and response of the system have been observed for all simulations. The results

presented in this paper are chosen because they effectively allow to point out the strengths and limitations of the tool.

Hereafter, the model used for the simulations is presented and discussed, including four different collision scenarios. These collision scenarios involve two different Offshore Service Vessels (OSV): the first one with a mass of $6000\ tons$ and the second one with a mass of $24000\ tons$. Furthermore, the initial velocity of the ship is defined to study both low-energy impact with an initial kinetic energy of $12\ MJ$ and high-energy impact with an initial kinetic energy of $75\ MJ$.

Finally, it should be mentioned that as the validation methodology follows a comparative approach between analytical computation and numerical simulation, it is not necessary for the geometry and hydrodynamic characteristics of the FOWT to represent precisely the initial platform. Therefore, the investigated models are inspired by the OC3-Hywind to be consistent with the hydrodynamic characteristics defined in the *FOWT.mco* file, but the properties and geometry used for the model are defined to approximate and simplify the real platform. (Additional results for another geometry without considering the mooring lines may be found in *(Vandegar et al., 2023)*.

5.2. Finite Element Model Description

To model the aforementioned FOWT, a few simplifications are made: (i) only the tower of the platform is modeled, which is simplified as a tube with a constant diameter and thickness, (ii) the RNA is modeled as a lumped mass at the upper extremity of the tube, (iii) at the other extremity of the tube, the ballast is modeled as a thin, perfectly rigid disc, (iv) the ship is idealized as a perfectly rigid wedge, and (v) the ship's motion is limited to the y-direction.

With these simplification, the FOWT can be simplified as depicted in Fig. 5.2. Additionally, the dimensions and properties used for the model are listed in Tabs. 5.4 and 5.5.

Table 5.4.: Main dimensions of the numerical model.

Structure	Notation	Position [m]
Tower length	L	160
Arm lever	H	88
Water depth	-	320
Center of gravity	C	78
Center of Buoyancy	D	62.7
Mooring location	E	70

Moreover, the properties of the mooring lines are the ones of the actual platform, ie. the one given in Tab. 5.3.

In addition, to use LS-DYNA with the *BOUNDARY_MCOL card, a *FOWT.mco* file containing

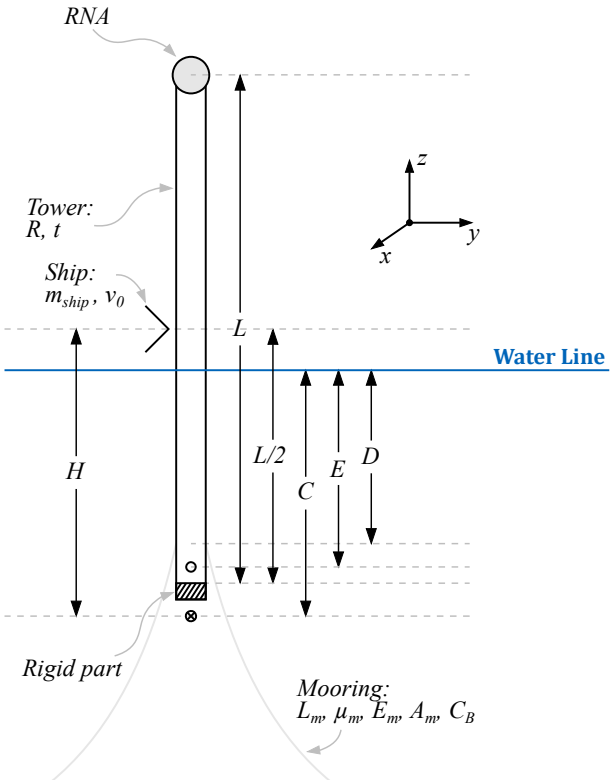

Figure 5.2.: Diagram with the main dimensions of the numerical model.

Table 5.5.: Structural properties of the numerical model.

Property	Notation	Value	Unit
Mass of the RNA	M_{RNA}	350	$tons$
Tower radius	R	3.5	m
Tower thickness	t	30	mm
Density	ρ	8500	kg/m^3
Ultimate strength	σ_y	255.7	MPa
Young's modulus	E	210	MPa

the matrices defining both the FOWT mass properties and hydrodynamic characteristics must be provided. The datafile used for this model is given in Appendix B.

It should also be mentioned that when using the MCOL solver with LS-DYNA, a rigid part needs to be defined. This rigid part is used to account for the rigid-body motion of the FOWT's CoG computed by MCOL. Therefore, the perfectly rigid disc defined in this model serves two purposes, (i) the first one is to satisfy the requirement for a proper usage of MCOL, (ii) the second one is to correct the mass and inertia of the model to be in accordance with the mass and inertia defined in the *FOWT.mco* file.

Furthermore, Belytschko-Tsay elements with two and five through-thickness integration points are utilized for the tube and for the impactor, respectively. Regarding the mesh size, *Ladeira et*

al. (2023) investigated similar collision scenarios for a clamped tube. In the context of their research, a convergence study was done and it was concluded that a maximum element size of 25 cm for the tube and an element size of 10 cm for the impactor should be considered. Moreover, a bi-linear piecewise plasticity behevior law is considered for the tube while a rigid material is used for the impactor. Furthermore, the strain-rate hardening effects are disregarded due to their inherent uncertainties and the complexities in the realistic modeling of these phenomena *(Yu and Amdahl, 2018)*. Note that their influence tends to be limited as ship collisions occur at relatively low velocities (lower than 10 m/s) as demonstrated by *Cerik & Choung (2020)*.

Fig. 5.3 presents a side view and a perspective view of the LS-DYNA model.

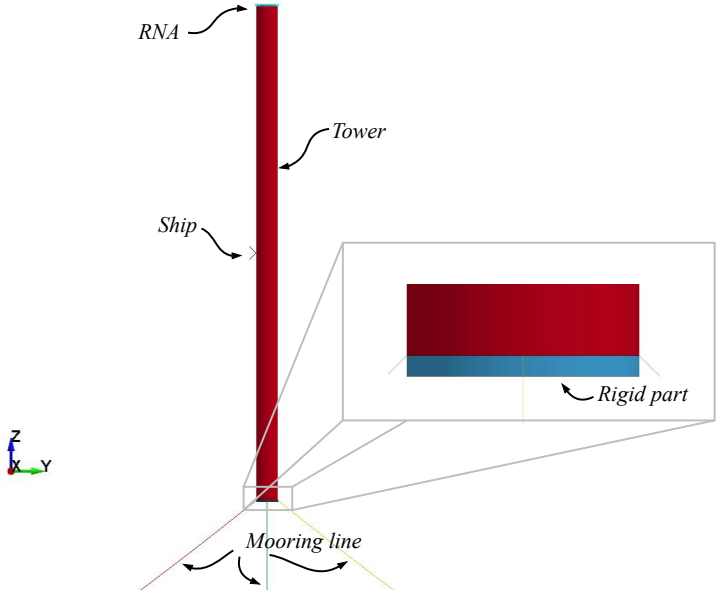

(a) Side view.

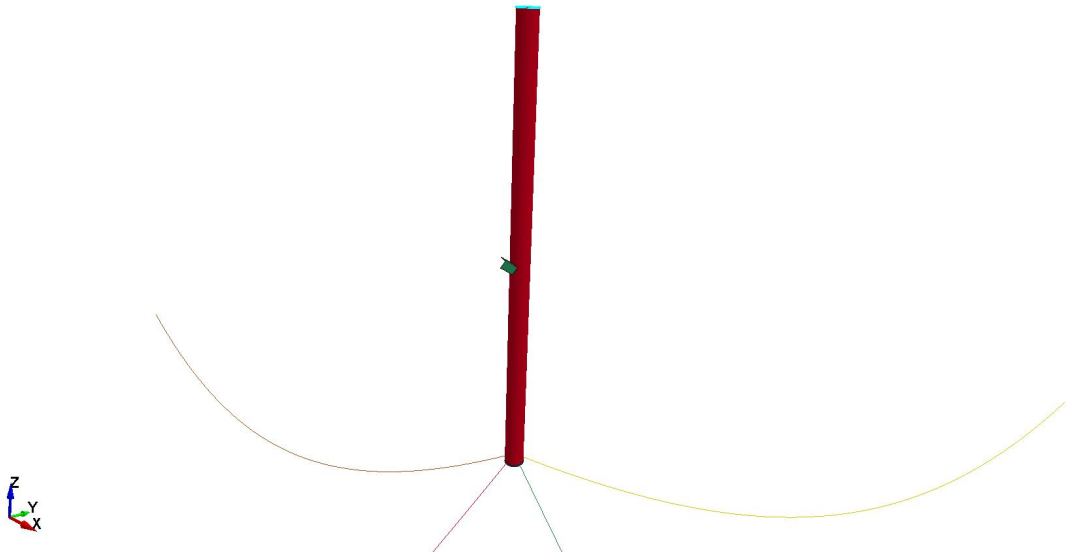

(b) Perspective view.

Figure 5.3.: Finite element model setup. An element size of 25 cm and 10 cm is used for the FOWT and the impactor, respectively.

Finally, as aforementioned, four different scenarios with different impactor masses and initial velocities are presented in this master thesis report. These scenarios are summarized in Tab. 5.6.

Table 5.6.: Summary of the different scenarios studied in this paper.

Scenario	Ship mass $[tons]$	Ship initial velocity $[m/s]$	Initial kinetic energy $[MJ]$
Scenario 1	6000	2	12
Scenario 2	24000	1	12
Scenario 3	6000	5	75
Scenario 4	24000	2.5	75

5.3. FE Results and Comparison with the SE Solver

Initial energy of 12 MJ

The results of the first two scenarios, which involve an initial kinetic energy of 12 MJ, are presented here-after. To avoid redundancy, only the collision time-history of scenario 1 is depicted in Fig. 5.4.

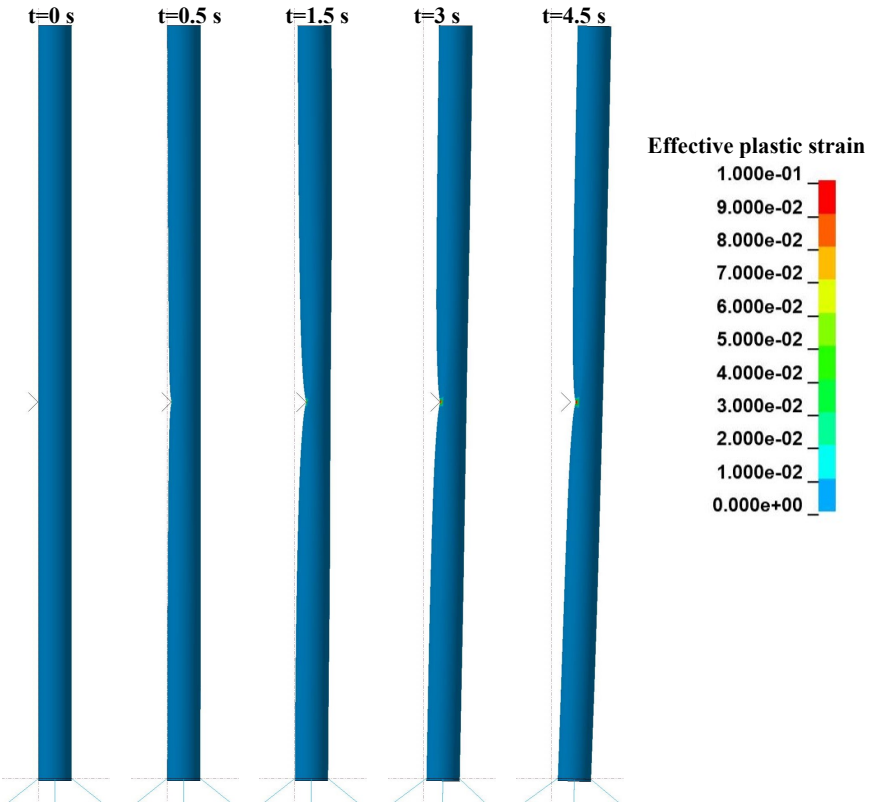

Figure 5.4.: Collision time history plot for an impactor with a mass of 6000 $tons$ and initial velocity of 2 m/s (scenario 1).

Additionally, the force-penetration curves, along with the penetration, energy balance, displacement of CoG, and rotation time history plots for both scenarios, are shown in Fig. 5.5. Lastly, the maximum resistance forces, penetration and deformation energies, as well as the sway, roll, and the time at which the loss of contact occurred, are compared in Tab. 5.7. The maximum penetration, sway and roll at the time of contact loss, t^*, denoted as $\delta_{max},\ y^*,\ \phi^*$, respectively, are defined as follows:

$$\delta_{max} = \delta(t^*) \tag{5.1}$$

$$y^* = y(t^*) \tag{5.2}$$

$$\phi^* = \phi(t^*) \tag{5.3}$$

Table 5.7.: Comparison of the maximum resistance force, penetration, absorbed energy, CoG translational displacement, CoG roll angle and time of contact obtained numerically and with the simplified analytical method for an initial energy of 12 MJ.

Scenario	Parameter	NLFEA	Analytical	$Disc.$ [%]
Scenario 1	F_{max}[MN]	5.25	4.29	-18.22
	δ_{max}[m]	2.46	2.44	-0.89
	U_{max} $[MJ]$	6.38	6.51	2.04
	y^* $[m]$	0.06	0.1	86.64
	ϕ^* [°]	0.33	0.44	31.46
	t^* $[s]$	1.95	2.06	5.49
Scenario 2	F_{max}[MN]	3.89	3.09	-20.5
	δ_{max}[m]	1.65	1.43	-13.55
	U_{max} $[MJ]$	2.63	2.75	4.34
	y^* $[m]$	0.08	0.11	40.12
	ϕ^* [°]	0.34	0.43	26.25
	t^* $[s]$	2.5	2.42	-3.43

The discrepancy in percentage between numerical and analytical results is computed such that:

$$Disc. = \left(\frac{Analytical - Numerical}{Numerical} \right) \cdot 100 \tag{5.4}$$

Moreover, the discrepancies are given as relative values to indicate whether the results are over ($Disc. > 0$) or underestimated ($Disc. < 0$) by the analytical approach.

For both scenarios, it can be seen that the analytical results are consistent with the numerical ones. The duration of contact between the impactor and the tube shows relatively small discrepancies, and the overall results are generally similar, excepted the sway displacement of the FOWT where the discrepancies are more pronounced. Furthermore, it can be observed that in both scenarios, the buckling mode occurring at the base of the tower (*Phase III*) is not reached, ie. the contact

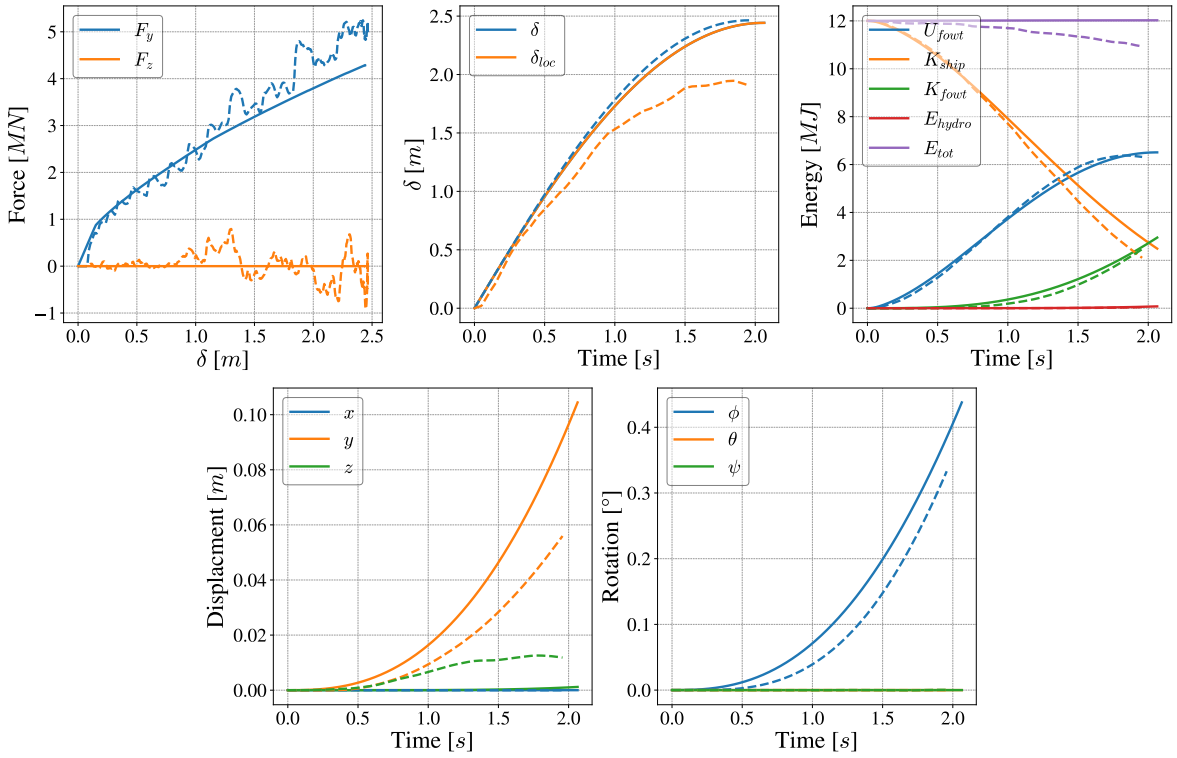

(a) Results for scenario 1, ie. an impactor mass $m_{ship} = 6000\ tons$ and initial velocity $v_0 = 2\ m/s$.

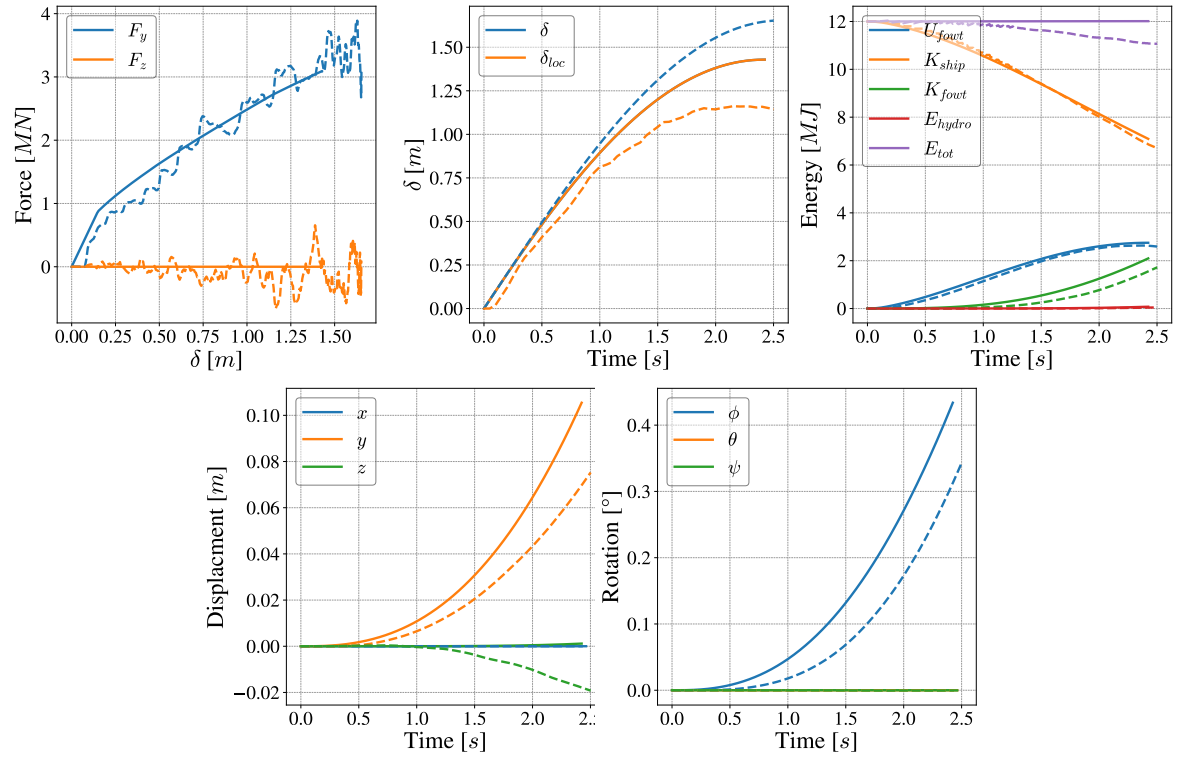

(b) Results for scenario 2, ie. an impactor mass $m_{ship} = 24000\ tons$ and initial velocity $v_0 = 1\ m/s$.

Figure 5.5.: Results obtained considering an initial energy of $E_0 = 12\ MJ$. Continuous and dashed lines represent the analytical and numerical results respectively (The time history plots are given for the range [0; t^*]).

between the impactor and the tube is lost during *Phase II*.

In the force-penetration diagram, the transition between *Phase I* and *Phase II* can be seen with the change in the slope of the horizontal resistant force F_y. Furthermore, for both scenarios, a vertical force F_z is observed, which is a result of the tube's elastic response to bending. However, since the impactor is perfectly rigid and limited to motion along the y-axis only, this vertical force mostly affects the heave motion of the FOWT's CoG. Nonetheless, the analytical computation provides a reasonably accurate approximation of the force-penetration curve in both scenarios, despite discrepancies of up to 20.5% observed for the maximum force.

In addition with the force-penetration plot, it can be observed that the forces computed in the numerical simulations contain high-frequency oscillations. These oscillations can be attributed to localized dynamic effects or small numerical instabilities. However, these oscillations do not significantly influence the overall quality of the results.

In LS-DYNA, the computation of the overall penetration is done by computing the displacement of the impact point relatively to the CoG of the tube, in the same way as for the analytical tool. As depicted in Fig. 5.6, the local penetration is computed by subtracting the distance between the impact point and its diametrically opposed point to the initial diameter of the tube:

$$\delta_{loc} = D - |ab| \tag{5.5}$$

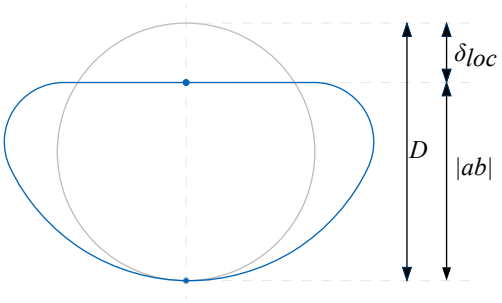

Figure 5.6.: Computation of the local penetration δ_{loc} geometrically.

In the penetration time history plots, it can be seen that neglecting the bending resistance of the tube leads to an overestimation of the local penetration. This overestimation makes the tool more conservative in terms of the local deformations. However, by neglecting the bending of the tube, the contact force is underestimated. Despite this, the overall penetration is generally well approximated by the analytical tool.

Regarding the energy balance plots, a good approximation of all energies can be observed in general. However, one may notice that the total energy is not constant in the numerical simulation. The gap in the total energy comes from the fact that the kinetic energy of the deformed nodes is not taken into account by LS-DYNA when coupled with MCOL. For more detail about this issue,

please refer to *(Ladeira et al., 2021)*. In addition, despite the discrepancies observed both in the resistance force and in the overall penetration, the FOWT deformation energy is generally well approximated with a maximum discrepancy of around 2% in scenario 1 and 4.3% in scenario 2.

It is also observed that the translation of the FOWT's CoG is not well approximated in all the investigated cases. Such discrepancies may be attributed to various factors and simplifications made in the analytical tool. Specifically, it is assumed that the platform rotates around its CoB, whereas in the numerical simulation, the FOWT rotates around the impact point as it can be seen in Fig. 5.7. As a result, the heave motion is negligible in the analytical tool but not in the numerical simulation. Consequently, the influence of the translation terms in the computation of kinetic energy requires further investigation.

Despite the discrepancy observed in the roll motion, a good approximation of the roll angle is generally observed in all the cases studied. Moreover, the discrepancy in the roll angle is computed at the time when the contact between the ship and the tube is lost . As a consequence, it is closely related to the discrepancy in the time of contact loss.

It is finally worth noting that the discrepancies observed on both the sway displacement and roll angle of the FOWT do not affect significantly the results in term of overall tower deformation as those values remain very small (less than 10 cm and 0.5° respectively).

Initial energy of 75 MJ

The results of scenario 3 and 4 are presented hereafter, ie. the cases with an initial kinetic energy of 75 MJ. To avoid redundancy, only the time history of scenario 3 is shown in Fig. 5.7.

The force-penetration curves, along with the penetration, energy balance, CoG displacement and rotation time history plots for both scenarios are given in Fig. 5.8. In the same way, the maximum resistance forces, penetration and deformation energies, as well as the sway displacement, roll angle, and time at which the loss of contact occurred, are compared in Tab. 5.8.

In the two scenarios proposed with an initial kinetic energy of 12 MJ, the results were quite similar in terms of response and amplitude. However, in scenario 3 and 4, the time of contact between the ship and the tube differs significantly. In addition, in scenario 3, *Phase III* is reached while in scenario 4, the contact between the ship and the tube is lost during *Phase II*. Moreover, the vertical force F_z is much higher for such high energy impacts than the one observed at lower energy impact.

Regarding the force-penetration diagram, in scenario 3, the distinction between *Phase II* and *Phase III* is noticeable by the sudden drop in the amplitude of the force F_y, both in the analytical and numerical results. This drop in the force F_y is also observed in scenario 4, although it is not as pronounced. Nevertheless, this sudden drop in the resistance force indicates the

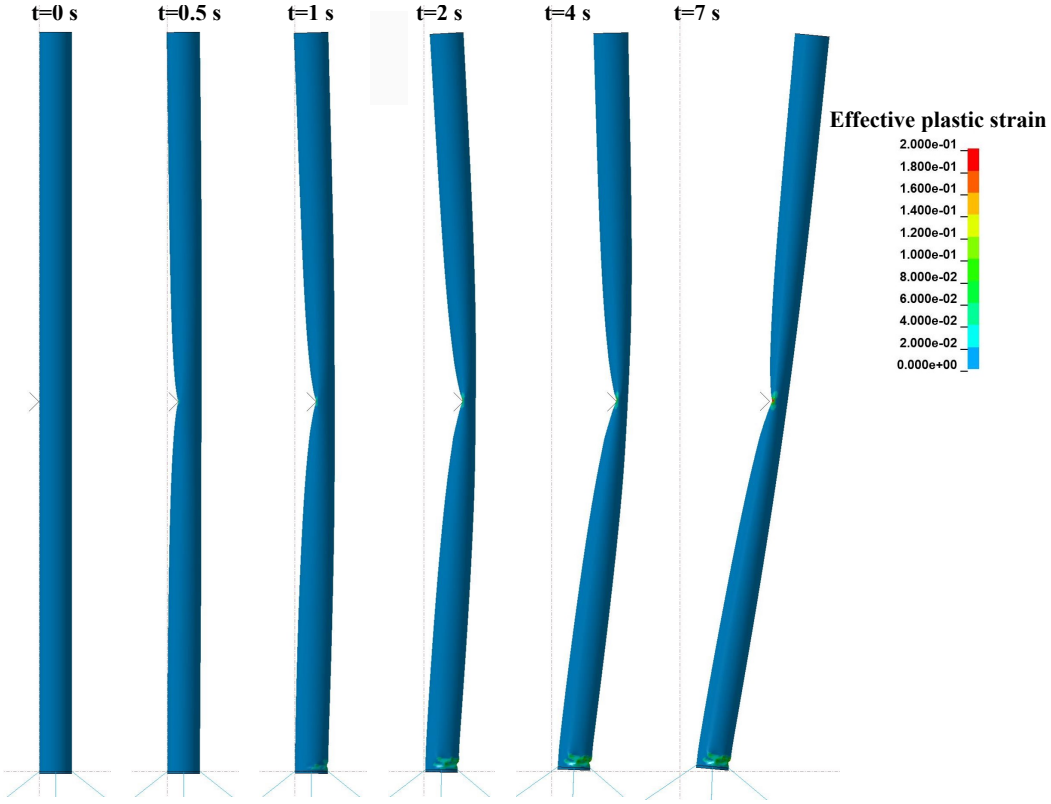

Figure 5.7.: Collision time history plot for an impactor with a mass of 6000 $tons$ and initial velocity of 5 m/s (scenario 3).

Table 5.8.: Comparison of the maximum resistance force, penetration, absorbed energy, CoG translational displacement, CoG roll angle and time of contact obtained numerically and with the simplified analytical method for an initial energy of 75 MJ.

Scenario	Parameter	NLFEA	Analytical	$Disc.$ [%]
Scenario 3	F_{max}[MN]	7.48	6.38	-14.71
	δ_{max}[m]	10.86	12.42	14.43
	U_{max} $[MJ]$	39.52	42.19	6.77
	y^* $[m]$	0.42	1.44	243.52
	ϕ^* [°]	2.9	3.83	31.93
	t^* $[s]$	4.79	5.86	22.24
Scenario 4	F_{max}[MN]	6.2	6.14	-1.04
	δ_{max}[m]	5.05	4.54	-10.08
	U_{max} $[MJ]$	16.57	17.29	4.31
	y^* $[m]$	0.37	0.35	-4.69
	ϕ^* [°]	2.07	1.38	-33.7
	t^* $[s]$	3.97	3.09	-22.15

occurrence of the "elephant foot" deformation mechanism at the base of the tube, as depicted in Fig. 5.9. Moreover, during the elephant foot deformation mechanism, the force oscillates in the numerical results. These oscillations are attributed to the folding at the base of the tube, forming the "elephant foot," and to the bending elastic response of the tube.

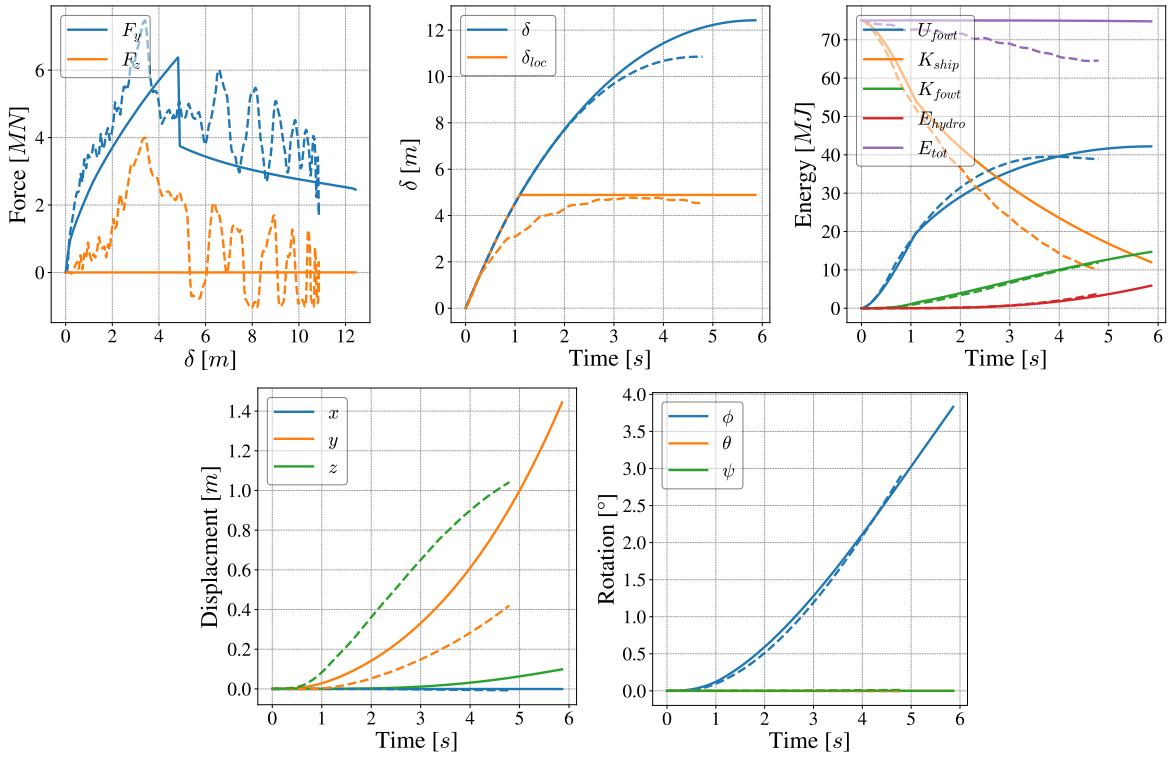

(a) Results for scenario 3, ie an impactor mass $m_{ship} = 6000\ tons$ and initial velocity $v_0 = 5\ m/s$

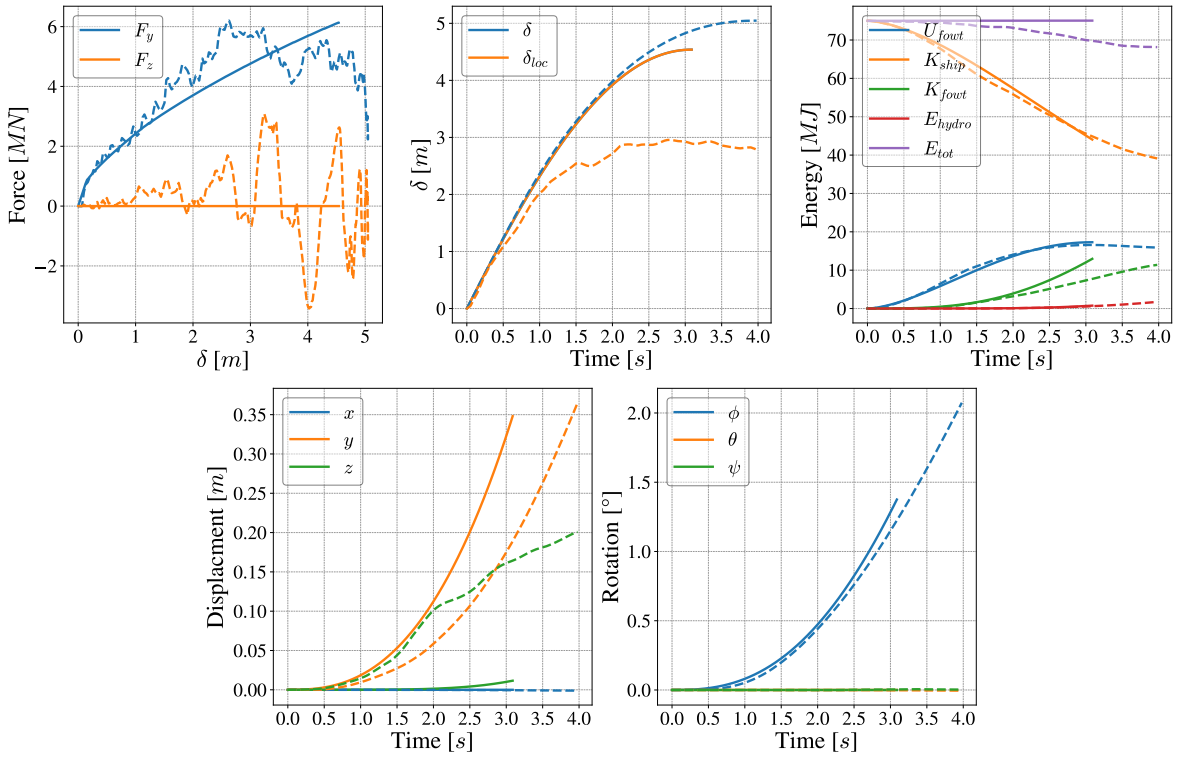

(b) Results for scenario 4, ie an impactor mass $m_{ship} = 24000\ tons$ and initial velocity $v_0 = 2.5\ m/s$

Figure 5.8.: Results obtained considering an initial energy of $E_0 = 75\ MJ$. Continuous and dashed lines represent the analytical and numerical results respectively (The time history plots are given for the range [0; t^*]).

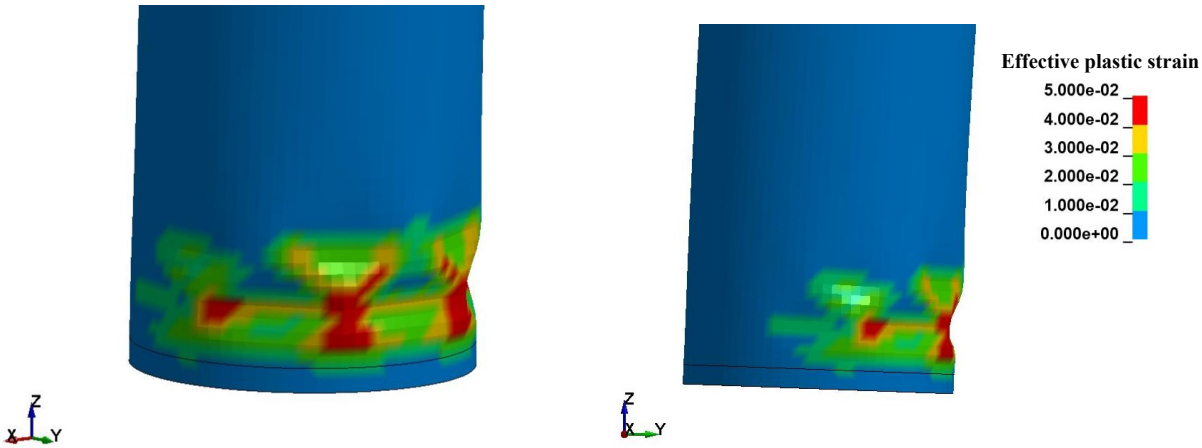

(a) Isometric view.

(b) Side view.

Figure 5.9.: Elephant foot deformation mechanism recorded in LS-DYNA at $t = 4\ s$ after the impact of an impactor with a mass of 24000 $tons$ and initial velocity of 2.5 m/s (Scenario 4).

In the penetration time history plot, the analytical tool provides a good approximation of the overall penetration for both scenarios. In scenario 3, the analytical tool approximates well the evolution of the local penetration over time. However, in scenario 4, where *Phase III* is not triggered by the analytical tool, the local penetration is significantly overestimated .

Moreover, the energy time history plot suggests a similar conclusion as the one drawn in the previous subsection. However, a greater discrepancy in the kinetic energy of the ship can be noticed in scenario 3, while a good approximation is observed in scenario 4. Additionally, the kinetic energy of the FOWT is well approximated in scenario 3, whereas there is a divergence from the numerical results in scenario 4.

Finally, the roll angle curves are almost perfectly approximated by the analytical tool. However, since the loss of contact is off by 20% in both cases, the angle at the loss of contact is not well approximated. Furthermore, in the lower initial energy cases, the FOWT sway displacement does not exceed a few centimeters, and its heave motion is negligible. However, for high energy impacts, the heave motion of the FOWT becomes significant, especially in scenario 3.

Kinetic Energy Breakdown

In order to understand the contribution of each terms in the kinetic energy, the later is firstly broken down in terms of the dry platform and the water added mass and secondly in terms of translation, rotation and coupled terms. The contribution of each terms can be computed as

follows:

$$K_{fowt} = \underbrace{\frac{1}{2}\boldsymbol{y}^T \mathbf{M}_{RB} \boldsymbol{y}}_{\text{Mass term}} + \underbrace{\frac{1}{2}\boldsymbol{y}^T \mathbf{M}_{\infty} \boldsymbol{y}}_{\text{Water added mass term}} \tag{5.6}$$

and:

$$K_{fowt} = \underbrace{\frac{1}{2}\sum_{i=1}^{3} m_{ii} y_i^2}_{\text{Translation term}} + \underbrace{\frac{1}{2}\sum_{i=4}^{6} I_{ii} y_i^2}_{\text{Rotation term}} + \underbrace{\sum_{i=2}^{5}\sum_{j=i+1}^{6} c_{ij} y_i y_j}_{\text{Coupled term}} \tag{5.7}$$

Where m_{ii} are the diagonal terms related to the mass of the FOWT in the total mass matrix, ie. the sum of the mass matrix and the water added mass matrix. I_{ii} are the diagonal terms related to the inertia of the FOWT in the total mass matrix, and c_{ij} are the non-diagonal elements in the total mass matrix.

An example of the time history plot for the distribution of kinetic energy is shown in Fig. 5.10. In this figure, the kinetic energy is computed for scenario 1 using the analytical tool. Additionally, the percentage distribution for each scenario discussed in the previous section is provided in Tabs. 5.9 and 5.10 to compare the contributions from the mass terms and the terms related to the motion of the FOWT, respectively. Furthermore, these values are computed at the time of the loss of contact between the impactor and the tube and are defined as follows:

$$Contibution = \frac{K_{\text{term considered}}}{K_{tot}} \cdot 100 \tag{5.8}$$

Table 5.9.: Kinetic energy distribution in percent considering the mass matrices.

Scenario	Analytical		Numerical	
	Mass	Added mass	Mass	Added mass
Scenario 1	26.11	73.89	27.76	72.24
Scenario 2	26.01	73.99	27.15	72.85
Scenario 3	24.93	75.07	27.82	72.18
Scenario 4	25.82	74.18	26.55	73.45
Average	25.72	74.28	27.32	72.68

Based on the results shown in Fig. 5.10a and Tab. 5.9, it can be seen that the kinetic energy of the FOWT is primarily influenced by the water added mass effect. On average, the contribution of these water added mass effects accounts for 73.48% of the total kinetic energy. In comparison, for a ship, the water added mass is generally assumed to be around 5% of the total weight of the ship. The disparity in these values is due to the geometry of the spar-type FOWT, where the elongated cylinder generates significant inertia compared to a typical ship, where the water

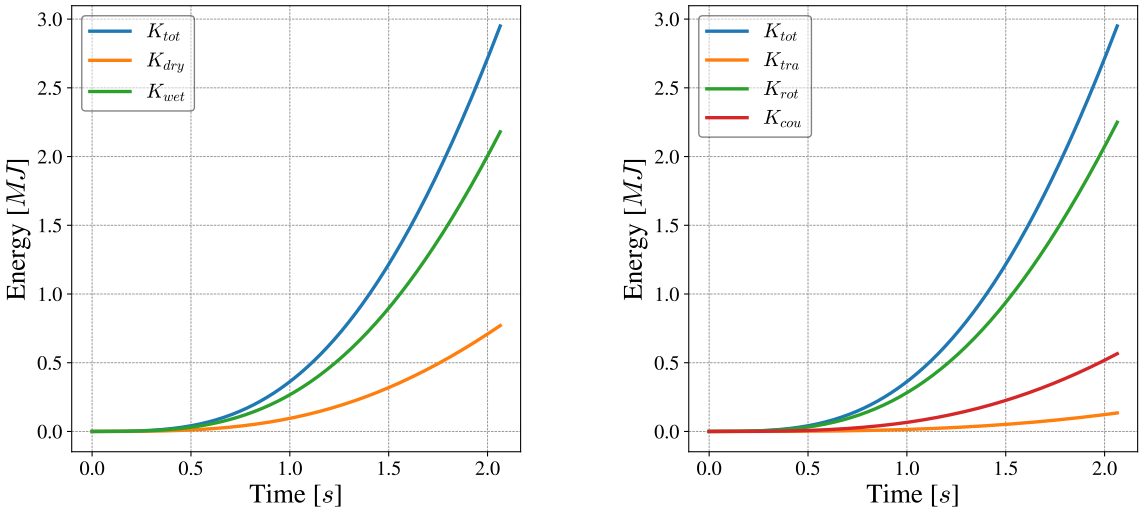

(a) Kinetic energy distribution considering the mass matrices.

(b) Kinetic energy distribution considering the motion of the FOWT.

Figure 5.10.: Diagram of numerical results of the kinetic energy breakdown for an impactor ship with a mass of 6000 $tons$ and initial velocity 2 m/s.

Table 5.10.: Kinetic energy distribution in percent considering the motion of the FOWT.

Scenario	Analytical			Numerical		
	Translation	Rotation	Coupled	Translation	Rotation	Coupled
Scenario 1	4.56	76.26	19.18	1.66	86.08	12.26
Scenario 2	4.84	75.51	19.65	2.6	82.55	14.84
Scenario 3	17.91	50.76	31.33	3.87	81.86	14.27
Scenario 4	5.47	73.9	20.63	3.7	78.92	17.38
Average	8.19	69.11	22.7	2.96	82.35	14.69

added inertia related to the ship surge motion is relatively small.

In Fig. 5.10b and Tab. 5.10, it can be observed that the contribution of the FOWT's translation is negligible, and the total kinetic energy is primarily influenced by the rotation of the platform. Therefore, it is important to accurately approximate the rotation of the platform, and the significant discrepancy observed in the sway motion of the platform may not be an issue. Specifically, there is no strict need to compute the heave motion at the CoG of the FOWT. Additionally, since the vertical force does not appear to contribute significantly to the dynamic response of the FOWT, except for the heave motion, it can be disregarded.

5.4. Discussion of the Results

As it can be seen with the four proposed scenarios, the accuracy of the analytical tool can easily be influenced by each parameters involved in the collision scenario. In general, it can be seen that for more rigid tube the approximation of the analytical tool is rather accurate,

whereas for more flexible tube, the accuracy of the tool becomes questionable. Therefore some generalities can be drawn for some parameters whereas the accuracy of the solver can be random for other. For example, the horizontal force is generally underestimated by the solver, the energy of deformation is well approximated in all cases, and the overall penetration can either be over or underestimated depending on the scenario and geometry of the tube.

However, the inaccuracy in some parameters can be justify by the assumption done in the analytical tool. As the tool improves, fewer simplifications will be done and consequently the reliability of the tool will increase. As of now, among the main assumptions that can affect the accuracy of the tool, the most important are (i) neglecting the tube elastic bending during *Phase II* and (ii) restraining the impactor's motion to one direction.

By neglecting the bending of the tube, the resistance force is underestimated and this can have a major influence on the time of contact between the ship and the FOWT. In addition, due to this underestimation, some deformation mechanisms might not be caught by the analytical tool as it was the case in scenario 4 where the *Phase III* was not reached in the analytical simulation, while the elephant foot buckling was observed in the numerical simulation.

Additionally, limiting the ship's motion to the y-axis leads to unrealistic motion of the FOWT. However, not doing this simplification complicates a bit the numerical model set-up. In order to consider the heave motion of the impactor, the later needs to be coupled with MCOL as well. However, the analytical tool is not developed enough to couple the impactor with MCOL yet. Therefore, if the numerical simulation takes the hydrodynamics effects of the ship and the analytical tool neglects them, new issues and discrepancies will appear because the two cases will be different. However, allowing the ship to move in 6-DOFs might resolve the issue with the vertical force and the heave motion of the FOWT.

Lastly, minor miscellaneous issues or limitation can be pointed out for future work and improvement of the analytical tool:

- The analytical tool is not able to compute the response of the system after the loss of contact. Therefore a *Phase IV* could be implemented to compute the dynamic response of the FOWT after the collision.
- The SE solver assumes a constant cross section area. However, the elephant foot buckling mechanism is highly influenced by the diameter of the FOWT where buckling appears. Therefore, improving the SE solver to consider different diameter would improve the reliability of the tool.
- The FOWT is assumed to be in "parked mode" where no forces related to the wind are considered. However, the wind force can have a major influence on the outcome of the collision as it can be seen in *Bela et al. (2017)*. Therefore the wind force should also be considered.

- The rotation of the wind turbine's blade can also affect the dynamic response of the FOWT. Therefore a fourth solver that would compute the forces resulting from the wind turbine motion could be implemented.

To sum up, despite the issues and points of improvement listed hereabove, it must be pointed out that the analytical tool already shows promising results. In general, it provides a good approximation of the deformation energy, with a discrepancy below 5% compared to numerical results. The maximum penetration typically shows a discrepancy less than 15%, and the maximum force can be underestimated by up to 25%. Such discrepancies can be acceptable at early design stage or when performing risk assessment or damage stability analyses. Moreover, in terms of computational time, the analytical tool takes only a few minutes to compute the outcome of the collision scenario, whereas the numerical simulation can take up to 18 hours to compute the outcome of a high initial kinetic energy impact.

6. CONCLUSION

6.1. Summary and Perspective

The expansion of the offshore wind energy farming presents particular challenges for maritime safety due to the increased risk of collisions between ships and OWTs, either because of ships passing by or because of OSV actively approaching the FOWT during maintenance operations.

This thesis aims to develop a simplified tool for assessing the ship-FOWT collision response for spar-type FOWT. Engineers often use NLFEA to ensure the crashworthiness of these structures. However, such approach can be computationally expensive when simulating numerous collision scenarios. Therefore, in the context of the ColFOWT project, the research seeks to integrate simplified approaches that consider both low and high-energy impacts. The goal is to develop a comprehensive rapid assessment tool for ship-OWT collisions, addressing various factors like local and global deformation mechanisms, hydrodynamic effects, and mooring dynamic response. This tool will propose a good balance between accuracy and computational cost, making it practical for applications such as pre-project risk assessments, probabilistic damaged stability analyses, and structural optimization routines.

The Sections 1, 2 and 3, are respectively dedicated to: (i) The general introduction where the context of the research and the description of its main objectives are described; (ii) An overview of the physical phenomena that occur during a ship-OWT collision event including the internal mechanics and external dynamics of the system; And (iii) The different existing solvers that were used to develop the analytical tool.

The Section 4 presents the analytical tool developed in the scope of this master thesis. This section covers the applied hypotheses and assumptions, along with the definitions of the reference systems and terminology used in the analysis. Moreover, the tool is described in detail, providing a step-by-step explanation of the inclusions and coupling of each solver used, as well as the algorithm.

The Section 5 is dedicated to the validation of the developed tool. In this section, four scenarios of ship-FOWT collisions are simulated using LS-DYNA/MCOL finite element software and the results are compared with those obtained from the developed analytical tool. The scenarios

involve a simplified model of an NREL 5 MW baseline turbine mounted on an OC3 Hywind reference spar platform impacted by two different OSVs (One with a mass of 6000 $tons$ and the other one with a mass of 24000 $tons$) at different initial velocities.

Finally, the proposed analytical tool shows promising results in terms of accuracy and computational cost. A good correlation between the numerical and analytical results is usually observed. Moreover, since the higher discrepancies observed do not significantly influence the outcome of the collision, such discrepancies can be disregarded, as discussed in Section 5.4. Additionally, the analytical tool is relatively new, and further work will be conducted to improve the tool and reduce the observed discrepancies.

6.2. Recommendation for Future Work

Listed hereafter is the major improvements that will improve the quality of the tool and the reliability of the results:

- A methodology to estimate the elastic response of the tube in bending for an impact at mid-length can be implemented, following a similar approach used for a quarter-length impact in the SE solver proposed by *Ladeira et al. (2023)*;
- At the moment, MCOL is only used for the FOWT. Using MCOL to compute the external dynamics of the ship will improve the computation of the ship's kinetic energy as well as the overall penetration. In addition, the ship's motion will be computed in 6-DOFs instead of 1-DOF as it is currently done;
- Computing the deformation of the ship will improve the tool as well. As of now, the tool is rather conservative with the computation of the damage suffered by the FOWT. Nevertheless, it would certainly be more realistic to also estimate the damage suffered by the ship. This would allow to estimate, for example, the probability of loss of the striking vessel;
- As established in *(Bela et al., 2017)*, the environmental conditions such as wind and waves can have a major influence in the outcome of a ship-FOWT collision event. Therefore, computing the environmental conditions and coupling them with the RNA's motion would also improve the proposed tool.

Bibliography

Bela, A., Le Sourne, H., Buldgen, L., and Rigo, P. (2017). Ship collision analysis on offshore wind turbine monopile foundations. *Marine Structures*, 51:220–241.

Buldgen, L., Le Sourne, H., and Pire, T. (2014). Extension of the super-elements method to the analysis of a jacket impacted by a ship. *Marine Structures*, 38:44–71.

BV (2021). Rules for the classification and certification of floating offshore wind turbines. Standard NI572 R02, Bureau Veritas.

Cerik, B. C. and Choung, J. (2020). On the modelling of strain-rate effects in nonlinear fe analysis of ship collisions. In *Proceedings of the International Conference on Ships and Offshore Structures, Glasgow*.

Conti, F., Le Sourne, H., Vassalos, D., Kujala, P., Lindroth, D., Kim, S. J., and Hirdaris, S. (2022). A comparative method for scaling solas collision damage distributions based on ship crashworthiness–application to probabilistic damage stability analysis of a passenger ship. *Ships and Offshore Structures*, 17(7):1498–1514.

Dai, L., Ehlers, S., Rausand, M., and Utne, I. B. (2013). Risk of collision between service vessels and offshore wind turbines. *Reliability Engineering & System Safety*, 109:18–31.

DNV-GL (2021). Recommended practice for determining design loads for offshore wind turbines. Recommended Practice DNVGL-RP-C204, Det Norske Veritas Germanischer Lloyd.

Echeverry, S. (2021). *Numerical and analytical study of a spar-like floating offshore wind turbine impacted by a ship*. PhD thesis, University of Liege.

Echeverry, S., Márquez, L., Rigo, P., and Le Sourne, H. (2019). Numerical crashworthiness analysis of a spar floating offshore wind turbine impacted by a ship. In *Developments in the collision and grounding of ships and offshore structures*, pages 85–95. CRC Press.

IEC (2020). Wind turbines – part 3-2: Design requirements for offshore wind turbines. Technical report 61400-3-2, International Electrotechnical Commission.

Jones, N. (2011). *Structural impact*. Cambridge university press.

Jonkman, J. (2010). Definition of the floating system for phase iv of oc3. Technical report, National Renewable Energy Lab.(NREL), Golden, CO (United States).

Jonkman, J. M. (2007). *Dynamics modeling and loads analysis of an offshore floating wind turbine*. University of Colorado at Boulder.

Konsept-It, I. P. S. (n.d.). RENEWABLE ENERGY - Dr.Techn. Olav Olsen AS. Accessed: 20-07-2023.

Ladeira, I. (2023). *Development of a fast and reliable solver based on simplified formulae to assess the response of standalone tubular Offshore Wind Turbine supports subjected to ship impact.* PhD thesis, École centrale de Nantes.

Ladeira, I., Jaramillo, S. E., and Le Sourne, H. (2023). A simplified method to assess the elasto-plastic response of standalone tubular offshore wind turbine supports subjected to ship impact. *Ocean Engineering*, 279:114313.

Ladeira, I., Le Sourne, H., Echeverry, S., and Rigo, P. (2021). Assessment of the energy balance gap for ship-fowt collision simulations with ls-dyna/mcol. In *Developments in the Analysis and Design of Marine Structures*, volume 85864, pages 221–228. MARSTRUCT Virtual Institute, CRC Press.

Ladeira, I., Marquez, L., Echeverry Jaramillo, S., Le Sourne, H., and Rigo, P. (2022). Review of methods to assess the structural response of offshore wind turbines subjected to ship impacts. *Ships and Offshore Structures*, pages 1–20.

Le Sourne, H. (2007). A ship collision analysis program based on super-element method coupled with large rotational ship movement analysis. In *4th International Conference on Collision and Grounding of Ships*, pages 131–138.

Le Sourne, H., Besnard, N., Cheylan, C., and Buannic, N. (2012). A ship collision analysis program based on upper bound solutions and coupled with a large rotational ship movement analysis tool. *Journal of Applied Mathematics*, 2012.

Le Sourne, H., Donner, R., Besnier, F., and Ferry, M. (2001). External dynamics of ship-submarine collision. In *Preprints of 2nd International Conference on Collision and Grounding of Ships, Copenhagen*.

Margientimmer (2022). Rudderless Julietta D causes damage to foundation of wind farm Hollandse Kust Zuid - Windpark Hollandse Kust South. Accessed: 12-07-2023.

Márquez, L., Le Sourne, H., and Rigo, P. (2022). Mechanical model for the analysis of ship collisions against reinforced concrete floaters of offshore wind turbines. *Ocean Engineering*, 261:111987.

Moan, T. (2009). Development of accidental collapse limit state criteria for offshore structures. *Structural Safety*, 31(2):124–135.

NORSOK, D. (2004). Standard N-004. Design of steel structures, Appendix A, Design against accidental actions.

Pevrot, A. and Goulois, A. (1979). Analysis of cable structures. *Computers & Structures*, 10(5):805–813.

Pineau, J.-P., Conti, F., Le Sourne, H., and Looten, T. (2022). A fast simulation tool for ship grounding damage analysis. *Ocean Engineering*, 262:112248.

Pire, T., Le Sourne, H., Echeverry, S., and Rigo, P. (2018). Analytical formulations to assess the energy dissipated at the base of an offshore wind turbine jacket impacted by a ship. *Marine Structures*, 59:192–218.

Ting, L. and Yuan, S. (1958). On radial deflection of a cylinder of finite length with various end conditions. *Journal of the Aerospace Sciences*, 25(4):230–234.

Vandegar, G., Sone Oo, Y. P., Ladeira, I., Le Sourne, H., and Echeverry, S. (2023). A simplified method to assess the elastoplastic response of standalone tubular floating offshore wind turbine supports subjected to ship impact. *Proceedings of the International Conference on Collision and Grounding of Ships and Offshore Structures, Nantes, France*.

Wierzbicki, T. and Suh, M. (1988). Indentation of tubes under combined loading. *International Journal of Mechanical Sciences*, 30(3-4):229–248.

Yu, Z. and Amdahl, J. (2018). A review of structural responses and design of offshore tubular structures subjected to ship impacts. *Ocean Engineering*, 154(November 2017):177–203.

Yu, Z., Amdahl, J., Rypestøl, M., and Cheng, Z. (2022). Numerical modelling and dynamic response analysis of a 10 mw semi-submersible floating offshore wind turbine subjected to ship collision loads. *Renewable Energy*, 184:677–699.

Zhang, Y., Hu, Z., Ng, C., Jia, C., and Jiang, Z. (2021). Dynamic responses analysis of a 5 mw spar-type floating wind turbine under accidental ship-impact scenario. *Marine Structures*, 75:102885.

Appendix

A. ICCGS 2023 Article

A simplified method to assess the elastoplastic response of standalone tubular Floating Offshore Wind Turbine supports subjected to ship impact

G. Vandegar, Y.P. Sone Oo
ICAM Engineering School - Nantes Campus, France

I. Ladeira, H. Le Sourne
ICAM Engineering School - Nantes Campus, France
Nantes University, Ecole Centrale Nantes, CNRS, GeM Institute (UMR 6183), Nantes, France

S. Echeverry
ANAST, Department of ArGEnCo, University of Liège, Belgium

ABSTRACT: This paper presents a rapid collision simulation tool for Floating Offshore Wind Turbines (FOWTs), with specific focus on spar-buoy floating platforms. The tool is based on a semi-coupled approach, applying the rigid-body dynamics program MCOL to simulate external dynamics. Internal mechanics is modeled based on an elastoplastic simplified method for the impact response of standalone tubular OWT supports. First, the overall algorithm is explained: an overview of both internal mechanics and external dynamics solvers is provided along with a detailed description of the coupling method. Second, the presented collision tool is validated by comparing against simulations performed with LS-DYNA/MCOL. The case study consists of a 6000-tons offshore supply vessel impacting an NREL 5MW baseline turbine mounted on an OC3 Hywind reference spar platform at velocities of 2 m/s and 5 m/s. Results demonstrate that the tool is capable of accurately capturing the response of both the turbine and the vessel, accounting for the effects of water added mass, wave radiation and viscous damping, as well as hydrostatic restoring forces. It presents a user-friendly and inexpensive alternative to NLFEA, with good accuracy for early-design stage.

1 INTRODUCTION

Offshore wind energy is a promising alternative for achieving a global transition to renewable energies. With a growing market and advancing technologies, offshore wind power presents itself as a viable option for meeting increasing energy demands while reducing carbon emissions. However, this transition is not coming without challenges. Recently, a 37200-tons rudderless cargo ship drifted into the Hollandse Kust Zuid offshore wind farm in the Dutch North Sea during a storm (Hollandse Kust, 2023). The vessel impacted a monopile foundation and caused a significant dent in the structure, as illustrated in Figure 1.

As the number of offshore wind installations increases, the likelihood of collision events involving passing ships and offshore wind turbines (OWTs) rises, particularly for wind farms situated near maritime traffic lanes. Additionally, OWTs require regular maintenance, that entails service vessels to be frequently transporting personnel and equipment through the wind farm. Despite occurring at relatively low speeds, these interactions may still pose a considerable collision hazard (Dai et al., 2013) and even casualties. From a strictly structural perspective, for the OWT, outcomes may range from minor deformations to the complete failure of the structure depending on a wide variety of factors, notably the striking ship's impact energy, shape, and floater geometry as well as environmental conditions such as wind, and waves (Bela et al., 2017).

Figure 1. Damaged monopile foundation from the impact of a drifting cargo vessel (Dutch North Sea) - From (Hollandse Kust, 2023)

Therefore, to prevent or at least minimize these outcomes, OWT structural design must ensure their crashworthiness based on collision accidental limit

states (ALS) defined by established standards and regulations e.g., (DNV-GL, 2021), (BV, 2021), (IEC, 2020). These assessments are risk-based, meaning that the probability of failure is evaluated for many collision scenarios.

Floating offshore wind turbines (FOWTs) present unique challenges due to the hydrodynamic loads (water inertia, wave radiation and drag damping, hydrostatic restoring) that govern the response of the impacted structure. Collision events may thus be modeled using step-by-step algorithms that couple internal mechanics with external dynamics.

Echeverry et al. (2019) investigated the response of a spar-buoy FOWT collided by a ship using non-linear finite element analysis (NLFEA) software LS-DYNA in conjunction with MCOL external dynamics solver (Le Sourne et al., 2007). The influence of various parameters such as gravity, mooring lines, ballast, hydrodynamic forces, and impactor deformability was investigated. Numerical results showed that neglecting hydrodynamic loads led to a significant underestimation of the collision force. Indeed, hydrostatic restoring forces counteract the spar's floater resulting pitch and heave motions and thus significantly affect both the damage and the rigid-body movement of the FOWT.

More recently, Zhang et al. (2021) used the LOADUD subroutine in LS-DYNA to consider hydrodynamic, aerodynamic, and mooring loads in the collision model. The study focused primarily on the global motions of a spar FOWT and the resulting acceleration of the nacelle.

Yu et al. (2022) used the cost-effective non-linear finite element code USFOS to assess the response of a semisubmersible DTU 10 MW turbine mounted on the OO-STAR floater and impacted by a 7500-tons OSV. The proposed model accurately captured the damage of both structures, as well as their body dynamics and contact force generated through collisions.

Reinforced concrete barge floaters have recently been the subject of numerical investigations, as reported by Marquez et al. (2022). To validate a proposed simplified collision mechanical model, the study simulated a collision between a 3000-tons OSV and the ITI Energy barge (Jonkman, 2007) using LS-DYNA/MCOL.

All abovementioned studies showed that NLFEA allows for accurate modeling of the complex physical phenomena that take place in a ship-FOWT collision event, including large deformations, plasticity, complex contact, and fluid-structure interaction. However, such numerical analyses remain time intensive, not only in terms of computation, but also with regards to model preparation. This is especially problematic in the context of risk assessments, where up to hundreds of collision scenarios involving different striking ships and different impact conditions must be simulated (Moan, 2009), rendering the method completely unpractical.

As an alternative to NLFEA, fast super-element (S.E.) solvers based on closed-form expressions derived from plastic analysis have been developed for ship-ship collision (Le Sourne et al., 2012), ship-jacket collision (Pire et al, 2018) and ship grounding (Pineau et al., 2022) simulations. Resulting pre-design tools are particularly useful for damage stability analyses and crashworthiness optimization, as recently demonstrated by Conti et al. (2022) for ship-ship collisions. However, these solvers typically neglect the elastic mechanisms and consequently fail to predict OWT resisting force for low-energy impacts, as demonstrated by Echeverry (2021). That is why the authors of this paper recently introduced elastic mechanisms in a new S.E. solver to simulate the elasto-plastic response of clamped-free standalone tubular OWT supports (Ladeira et al., 2023). Guessing that the ballast of a spar-buoy FOWT acts like a "moving" clamped boundary condition for the tower, the objective of the present work was to couple the abovementioned solver with MCOL external dynamics program, the aim being to fully simulate the response of this kind of FOWT to a ship impact.

2 SUPER-ELEMENT SOLVER

Ladeira et al. (2023) carried out a series of impact numerical simulations, which demonstrated the presence of three distinct phases in the deformation process of a standalone tubular OWT support, impacted at quarter and mid-length from its lower fixed extremity: (i) an initial local elastic indentation at the contact zone, followed by (ii) a local plastic indentation combined with a global beam-like elastic bending, and (iii) a final buckling mechanism at the base of the tube.

Based on these observations, a quasi-static S.E. solver that encompasses this complete elasto-plastic response was developed. It can estimate associated force-penetration and energy balance time-history curves by integrating theoretical formulations for each of the deformation mechanisms into a comprehensive time-stepping algorithm. The OWT support is idealized as a cantilever tube with a constant average cross-section.

A summary of the analytical derivations applied for each deformation phase is provided in the following subsections. For detailed explanations, please refer to Ladeira et al. (2023).

2.1 *Phase 1 - Local Elastic Denting*

The local elastic denting mechanism in *Phase 1* is modeled based on the assumption that the tubular member consists of a cylindrical thin-walled shell that

is subjected to a pair of diametrically opposed punctual forces (Ting & Yuan, 1958).

In the cylindrical coordinate system (r, φ, x), consider the radial displacement $w_1(x, \varphi)$ of the tubular member subjected to a collision force. A closed-form solution can be obtained by expressing the general differential equation in the form of a Fourier series. For the loaded cross-section ($x = 0$) at the impact point, the radial displacement is given by:

$$w_1(0, \varphi) = 1.117 \frac{F_1 R^3}{B_r R \sqrt{\frac{R}{t}}} \sum_{n=2,4,6,\dots}^{\infty} \left(\frac{t}{R} \frac{\cos(n)}{A_n} \right) \quad (1)$$

where F_1 is the local elastic denting load, R is the tube's mean radius and t is its thickness. Coefficients A_n are dependent on the geometric characteristics of the tube. The parameter B_r denotes the ring bending stiffness of the tube's wall per unit length under plane strain conditions: $Et^3/12(1-\upsilon^2)$, with E and υ denoting, respectively, the material's Young modulus and Poison coefficient.

Assuming that the local indentation is equal to twice the displacement $\delta_l = 2w_1(0,0)$ at the load application, Equation 1 can be rewritten in terms of the local elastic resistance force F_1 as a function of local indentation δ_l:

$$F_1(\delta_l) = 8.928 \left(\frac{B_r \sqrt{\frac{R}{t}}}{R^2} \right) \delta_l \quad (2)$$

The threshold for the local elastic denting mechanism is defined by the characteristic collapse resistance of the tube's wall. Thus, *Phase 2* is triggered once $F_1 \geq F_1^c$, where F_1^c may be calculated as:

$$F_1^c = \sigma_y \frac{t^2}{4} \sqrt{\frac{D}{t}} \quad (3)$$

where σ_y is the yield strength and D is tube's diameter.

2.2 *Phase 2 - Combined Mode*

Phase 2 consists of a combination of local plastic denting and global beam-like elastic bending. These mechanisms are strongly coupled and interact through a highly non-linear dynamic that appears to be particularly sensitive to the tube's characteristic geometry, the impact location and the impactor's kinetic energy.

Applying existing closed-form solutions for each individual mechanism, corresponding resistances can be evaluated independently and in parallel at each time-step. A resultant force is then obtained by combining these two values.

2.2.1 *Local Plastic Denting*

The mathematical model applied to calculate the local plastic denting resistance is based on the formulation developed by Buldgen et al. (2014) for the local crushing resistance of a tubular jacket members. It relies on plastic analysis, assuming that the tube is made of a rigid-perfectly plastic material characterized by a flow stress σ_0. The resistance is then derived by applying the upper bound theorem (Jones, 2011) to a pre-defined displacement field that approximates the deformation pattern expected for such a mechanism, as depicted in Figure 2.

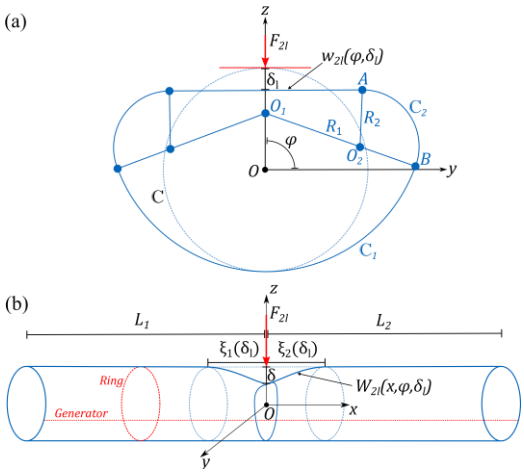

Figure 2. Definition of the displacement field as presented by Buldgen et al. (2014) for the local plastic denting mode. (a) Cross-section view. (b) Side view.

The initial step consists in defining the displacement field. A convenient way to achieve this is via the approach proposed by Wierzbicki & Suh (1988): the tube is assumed to be composed of a series of generators supported by independent rings that are allowed to freely slide along them without any shearing resistance, as illustrated in Figure 2.

The total deformation energy rate $\dot{E}_2$ is then calculated by summing the energy rates of the rings and the generators, respectively $\dot{E}_{2r}$ and $\dot{E}_{2g}$:

$$\dot{E}_2 = \dot{E}_{2r} + \dot{E}_{2g} \quad (4)$$

Given the *Virtual Velocity Principle*, which states that the internal energy rate $\dot{E}_2$ equals the external power associated to the tube's local plastic denting resistance F_{2l}, is it possible to obtain the following force-penetration relationship:

$$F_{2l}(\delta_l) = \left[\dot{E}_{2b} \frac{\xi_1 + \xi_2}{2} + \left(\frac{1}{\xi_1} + \frac{1}{\xi_2} \right) \dot{E}'_{2m} \right] \frac{1}{\delta_l} \quad (5)$$

where $\dot{E}_{2b}$ is the energy rate associated to both the change in curvature and bending of the plastic hinges that develop in the ring-like indented cross-section, and $\dot{E}'_{2m}$ is the energy rate associated to membrane deformation along the generators. Parameters ξ_1 and ξ_2 are obtained by minimizing the resistant force given by Equation 5, which leads to:

$$\xi_1 = min\left(\sqrt{\frac{2E'_{2m}}{E_{2b}}}, L_1 \right); \; \xi_2 = min\left(\sqrt{\frac{2E'_{2m}}{E_{2b}}}, L_2 \right) \quad (6)$$

2.2.2 *Global Elastic Bending*

Based on *Classical Beam Theory*, the global elastic beam bending resistance F_{2g} as a function of the tube's global beam displacement δ_g at the impact point writes:

$$F_{2g}(\delta_g) = \frac{3EI}{L_1^3}\delta_g \quad (7)$$

Here, I is the cross-section's second moment of area and L_1 is the longitudinal distance from the base of the tube to the impact point.

2.2.3 *Local/Global Mode Integration*

The integration of the local plastic denting and global elastic bending mechanisms is done through a simple procedure. During *Phase 1*, the resistance forces associated to local plastic denting F_{2l} and global elastic bending F_{2g} are calculated in parallel with the dominant mechanism, local elastic denting resistance F_1.

When the characteristic collapse resistance of the tube's wall F_1^c is reached and *Phase 2* is triggered, the values of F_{2l} and F_{2g} at this specific step are saved and used to calculate local C_l and global C_g correction coefficients, respectively:

$$C_l = \frac{F_1^c}{F_{2l}(\delta_t)} \quad (8)$$

and

$$C_g = \frac{F_1^c}{F_{2g}(\delta_t)} \quad (9)$$

where δ_t is the penetration at the transition between *Phase 1* and *Phase 2*.

For mid-length impacts, the numerical simulations showed that during *Phase 2*, the contribution of the global elastic bending mode to the total deformation energy appears to be less significant compared to the local plastic denting counterpart. During this phase, intentionally neglecting the contribution of the global elastic bending mode to the overall resistance was found to yield satisfactory results in most of the cases. The resulting force F_2 is thus calculated as:

$$F_2 = F_{2l}(\delta_l)C_l \quad (10)$$

A detailed description of this methodology applied to quarter-length impacts and further discussion on the utilized assumptions are given in (Ladeira et al., 2023).

The transition to *Phase 3* occurs when the plastic collapse load of the cantilever tube F_2^c is reached ($F_2 \geq F_2^c$). The value of F_2^c is given by:

$$F_2^c = \frac{M_0}{L_1} \quad (11)$$

where $M_0 = D^2 t\sigma_0$ is the tube's fully plastic bending moment.

2.3 *Phase 3 - Elephant Foot Buckling*

The "elephant foot" asymmetric buckling mode is observed at the base of the tube, where the region under compression sustains successive folding. Pire (2018) proposed a semi-analytical methodology to assess the resistance force of an analogous mechanism observed in jacket foundations under ship impact. A plastic limit analysis is performed, following an approach like the one used for local plastic denting.

The displacement field is postulated according to the geometry depicted in Figure 3. As done previously, the tube is idealized as a composition of rings and generators.

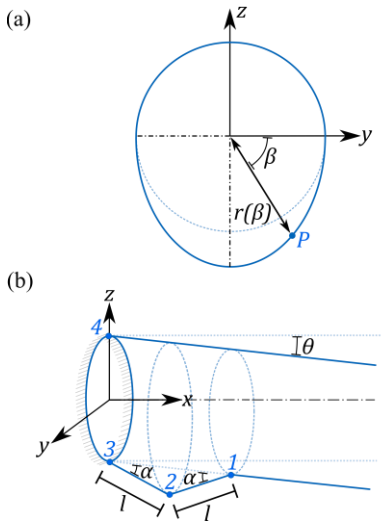

Figure 3. Schematic representation of the displacement fields defined for the deformation pattern at the base of the tube. (a) Cross-section view. (b) Side view.

The following mechanisms compose the deformation process: three plastic hinges (numbered 1, 2 and 3 in Figure 3) that develop as a consequence of the generator's folding, the elongation of the rings located between hinges 1 and 3 that introduce membrane strain in the cross-section, and a fourth plastic hinge (numbered 4 in Figure 3) that develops at the clamped base on the non-folded side of the tube due to its overall rotation.

The total deformation energy rate $\dot{E}_3$ is obtained by summing the energy rates associated to deformation at the hinges ($\dot{E}_3^{h1}, \dot{E}_3^{h2}, \dot{E}_3^{h3}, \dot{E}_3^{h4}$) and membrane effects at the generators $\dot{E}_3^m$:

$$\dot{E}_3 = \dot{E}_3^{h1} + \dot{E}_3^{h2} + \dot{E}_3^{h3} + \dot{E}_3^{h4} + \dot{E}_3^m \quad (12)$$

Finally, by applying the *Virtual Velocity Principle* to the total energy rate given by Eq. (11), the resistance force F_3 is obtained for a given penetration rate $\dot{\delta}_g$ by:

$$F_3 = \dot{E}_3 \frac{1}{\dot{\delta}_g} \quad (13)$$

3 COUPLING WITH MCOL SOLVER

3.1 *MCOL external dynamics solver*

As the motion of a floating body is generally governed by hydrostatic restoring forces F_H, wave radiation damping forces F_W, drag damping forces F_V and water inertial forces, these are accounted for in the model through the large rotation rigid-body dynamics solver MCOL. In this study, the FOWT rigid-body movement during the collision is captured by solving an equation of motion in the time domain while including the abovementioned hydrodynamic contributions.

To do this, the hydrodynamic characteristics of the spar-buoy floater (i.e., water added mass M_∞, hydrostatic and frequency dependent wave damping matrices) are previously determined using the *Hydrostar* seakeeping code and stored into the so-called FOWT.mco file. Storing in the vector F_C the contact force obtained from the S.E. solver presented in section 2 as well as the resulting pitch momentum, the 6 DOF rigid-body equation of motion has the general form:

$$M\dot{y} + G(y)y = [F_w + F_H + F_V](y, x) + F_C \qquad (14)$$

where $M = M_{FOWT} + M_\infty$ is the total mass matrix, $G = G_{FOWT} + G_\infty$ is the total gyroscopic matrix, while x and y are respectively the earth-fixed position and absolute translational and angular body-fixed velocity vectors of the FOWT's center of mass. The time integration of Equation 14 is performed by a classical step-by-step algorithm. Further details on the calculation of each term of Equation 14 can be found in (Ferry et al., 2002).

3.2 *Coupling with the S.E. solver*

As illustrated in Figure 4, the coupling between internal mechanics and external dynamics is based on successive calls of the S.E. solver described in Section 2 and MCOL. Note that SHIP.txt and FOWT.txt datafiles contain the involved structures particulars while the collision parameters such as the impact location and the ship initial velocity are defined in the so-called Scenario.txt datafile.

At each time step, the increment of penetration $\Delta\delta(t)$ is first obtained from the relative velocity between the ship and the FOWT:

$$\Delta\delta(t) = [v_{ship}(t) - v_{impact}] \cdot dt \qquad (15)$$

where the FOWT's velocity at the impact point is calculated as:

$$v_{impact}(t) = v_{fowt}(t) + \Omega_{fowt}(t) \cdot H \qquad (16)$$

Here, $v_{fowt}(\mathrm{t})$ and $\Omega_{fowt}(t)$ denote the surge and pitch velocities of the FOWT's center of gravity respectively and H is the height between the center of gravity and the impact point.

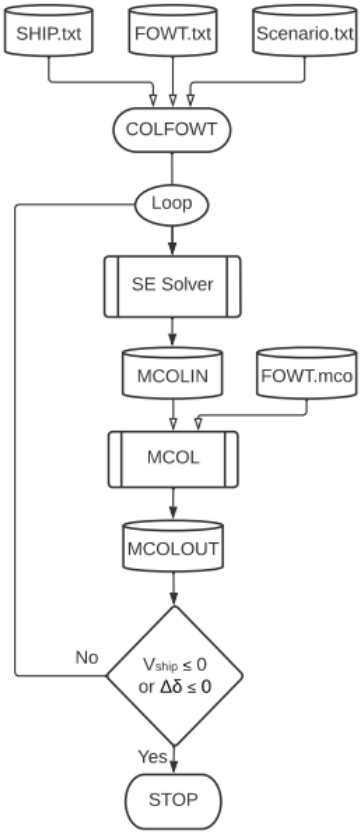

Figure 4. Scheme describing the methodology developed to couple Super-Element and MCOL solvers.

The contact force and resulting pitch torque are then computed by the S.E. solver and transmitted to the MCOL program, which calculates the new FOWT's velocities, $v_{fowt}(\mathrm{t})$ and $\Omega_{fowt}(t)$, considering the actions of the hydrodynamic loads. In parallel, the ship surge velocity v_{ship} is updated from its acceleration calculated as:

$$a_{ship}(t) = -\frac{F(t-dt)}{m_{ship}} \qquad (17)$$

The program stops when the ship velocity vanishes ($v_{ship}(t) = 0$) or when the contact between both structures is lost ($\Delta\delta(t) \leq 0$).

4 VALIDATION

4.1 *Finite element model description*

To validate the developed tool, non-linear finite element simulations are performed using the commercial software LS-DYNA along with the `*BOUNDARY_MCOL` card. The OWT support structure adopted from Jonkman (2010) is idealized as a simple cylinder with uniform diameter and thickness. A lumped mass of 350 tons is imposed at the top and a rigid ballast tank (6711 tons) at the bottom. The ballast behaves as

a clamped boundary which is then associated to MCOL by using `*PART_INERTIA`. Refer to Figure 5 and Table 1 to find the finite element model setup and the principal parameters respectively. As for the impactor, a simplified rigid wedge, having a total mass of 6000 tons (i.e., it is assumed that this value includes the surge water added mass of the ship), is considered. Initial velocities of 2 m/s and 5 m/s, corresponding to the initial kinetic energies of 12 MJ and 75 MJ respectively, are specified to the impactor. The nodes of the rigid impactor are permitted to translate in the *x*-direction only. The hydrodynamic characteristics of the spar-buoy floater, as mentioned in subsection 3.1, are then passed into the LS-DYNA solver via the same FOWT.mco file. Note that no mooring line has been considered in the article.

Table 1 Main dimensions of the OWT model (NREL 5MW OC3 adopted from Jonkman (2010))

D (m)	L (m)	$L_{ballast}$ (m)	t (mm)	M_{rna} (kg)
7.0	140	70	37	350,000

where D = OWT diameter, t = thickness, and M_{rna} = mass of the RNA.

Table 2 Material properties used for the FOWT

ρ (kg/m^3)	σ_y (MPa)	E (MPa)	E_{tan} (MPa)
8500	363.7	207,000	5500

Note that the yield strength σ_y is assumed to be the same as the average flow stress σ_0.

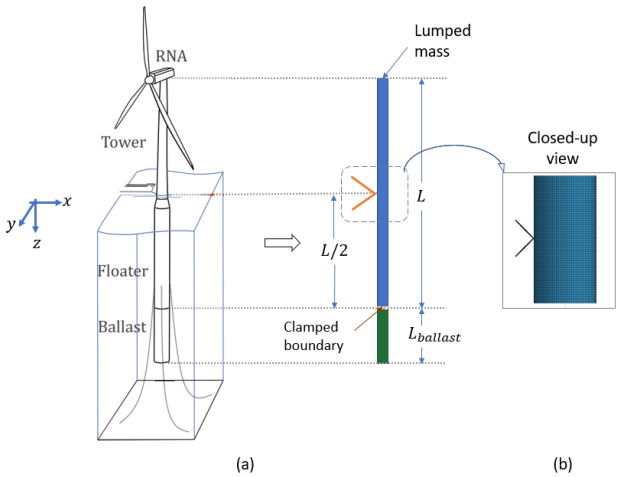

Figure 5 Typical finite element model setup: (a) Idealization of the FOWT as a simplified cylinder with a tip mass, and (b) Closed-up view of the FEA model in LS-DYNA.

Belytschko-Tsay elements with two and five through-thickness integration points are utilized for the impactor and for the tube respectively. In accordance with the convergence studies, see (Ladeira et al., 2023) for further details, a maximum element size of 25 cm was considered for the tube and 10 cm for the impactor. Piecewise linear plasticity model (*MAT_024*), with bi-linear consideration for simplicity (see Table 2), is applied for the test tube while rigid material (*MAT_020*) for the impactor. The strain-rate hardening effects are disregarded due to their inherent uncertainties and the complexities in the realistic modeling of these phenomena (Yu and Amdahl, 2018). Furthermore, their influence tends to be limited, as ship collisions occur at relatively low velocities (lower than 10 m/s) as demonstrated by Cerik and Choung (2020).

4.2 *Results and discussion*

4.2.1 *Results at 2 m/s*

For a ship collision at 2 m/s, force-penetration curve and energy balance time history plots are presented in Figures 6 and 7 respectively, while maximum levels of resistance force, deformation energy, total deformation (i.e, indentation + deflection) and rigid-body pitch angle are compared in Table 3.

Note that the discrepancy between numerical and analytical results is calculated as:

$$Disc. = \left(\frac{Analytical - Numerical}{Numerical}\right) \cdot 100 \quad (18)$$

Table 3 Comparison of maximum levels of resistant force, deformation energy, total deformation, and rigid-body pitch angle for an impact at 2 m/s

	F_{max} [MN]	U_{max} [MJ]	δ [m]	Pitch [°]
LS-DYNA	8847	7389	1.78	0.146
COLFOWT	7135	7920	1.79	0.150
Disc. [%]	-19.3	7.2	0.53	2.7

The force-penetration curve given by the analytical solver (COLFOWT) correlates rather well with the numerical one. Initially, both curves follow a linear trajectory with a relatively steep slope corresponding to the local elastic denting mode (*Phase 1*). Then, the slope decreases, marking the initiation of the combined local plastic/global elastic mode (*Phase 2*). At this velocity, the third mode of deformation (*Phase 3*) is not reached as contact loss occurs during *Phase 2*.

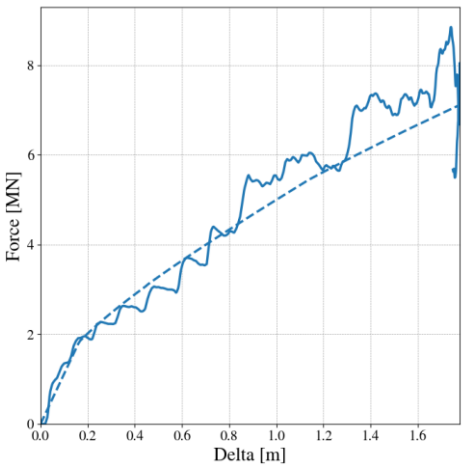

Figure 6 Force-penetration plot for an impact at 2 m/s. Dashed lines show the analytical results; Solid lines show the numerical results.

A good agreement between analytical and numerical results is also observed for the energy balance. The deformation energy U_{FOWT} calculated by the analytical solver correlates almost perfectly with the numerical results in the first second after the impact. It is then slightly over-estimated toward the end of the simulation. This can be explained by the fact that the quasi-static analytical approach is unable to capture the kinetic energy of the deformed parts. On contrary, in the LS-DYNA simulation, part of the ship initial kinetic energy is transferred to kinetic energy of the deformed nodes. Nevertheless, the maximum discrepancy on U_{FOWT} observed at the end of the simulation (i.e., when the contact between the ship and the FOWT is lost) does not exceed 7.2%.

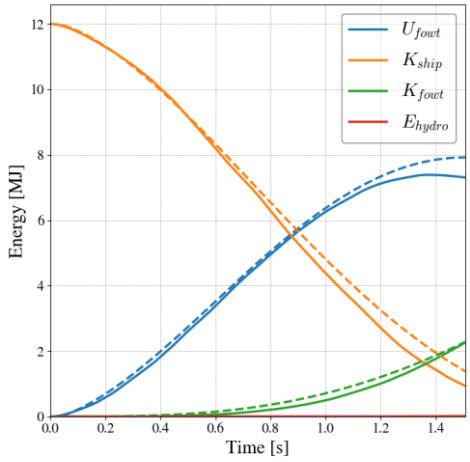

Figure 7 Energy balance time histories for an impact at 2 m/s. Dashed lines show the analytical results; Solid lines show the numerical results.

In terms of the ship and FOWT's kinetic energies, K_{ship} and K_{FOWT}, the analytical results also correlate well with the numerical ones. Finally, it is observed that the hydrodynamic energy E_{hydro}, calculated as the sum of hydrostatic, wave radiation and drag damping energies, remains negligible during the whole collision process.

4.2.2 *Results at 5 m/s*

For a collision at 5 m/s, force-penetration curves and energy balance time histories are plotted in Figures 8 and 9 respectively. In addition, maximum levels of resistant force, deformation energy, total deformation, and pitch angle are compared in Table 4.

Table 4 Comparison of maximum levels of resistant force, deformation energy, total deformation, and pitch angle for an impact at 5 m/s

	F_{max} [MN]	U_{max} [MJ]	δ $[m]$	Pitch [°]
LS-DYNA	15.15	45.53	5.83	0.858
COLFOWT	13.20	49.51	5.98	0.629
Disc. [%]	-12.9	8.7	2.6	-26.6

As for an impact at 2 m/s, *Phase 1* and first part of *Phase 2* are rather well approximated up to an overall deformation $\delta = 2$ m. A major spike then appears in the numerical simulation leading up to the plastic collapse of the tube. This effect occurs when the local mechanism ceases and the participation of the global elastic bending mode to the overall resistance rapidly increases. As a result, the force rises abruptly. Note that this behavior is not reproduced by the proposed analytical approach.

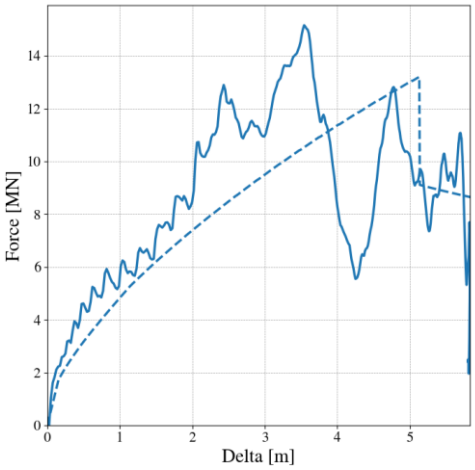

Figure 8 Force-penetration plot for an impact at 5 m/s. Dashed lines show the analytical results; Solid lines show the numerical results.

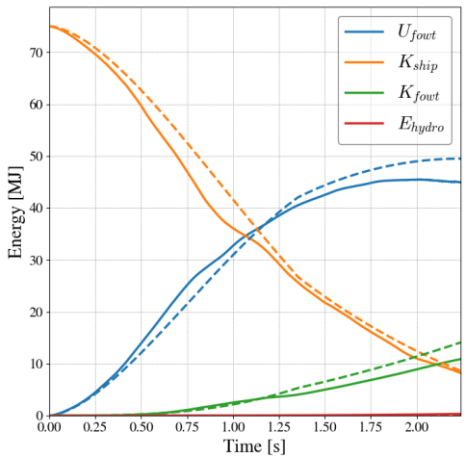

Figure 9 Energy balance time history plot for an impact at 5 m/s. Dashed lines show the analytical results; Solid lines show the numerical results.

Looking at the energies, Figure 9 suggests a similar conclusion as the one drawn for an impact at 2 m/s. The discrepancies between numerical and analytical results remain acceptable and the slight overestimation of U_{FOWT} and K_{FOWT} at the end of the collision is still due the quasi-static nature of the S.E. solver. It is finally worth noting that the total deformation δ of the impacted tower is correctly predicted and that the underestimation of the rigid-body pitch angle (26.6 %) does not affect the results as this rotational motion remains very small (less than 1°).

5 CONCLUSIONS

In this paper, a simplified method to predict the response of a spar-buoy FOWT subjected to low and high energy ship collisions is proposed. This approach combines distinct analytical models for the internal mechanics with the external dynamics solver MCOL into a time stepping algorithm that can predict the overall deformation process of the wind turbine in conjunction with the rigid-body motion of the floater. Its main purpose is to provide a rapid and easy-to-use assessment tool, suitable for risk-based damage stability analyses and crashworthiness optimization. It will serve as an alternative to computationally intensive NLFEA in early design stages, where time is a major constraint. The next steps of this research program will consist in integrating the action of the mooring lines as well as the deformability of the striking vessel.

ACKNOWLEDGEMENTS

This work was performed within the framework of the West Atlantic Marine Energy Community (WEAMEC) and granted by ICAM Engineering School, Pays de la Loire Region, and Europe (European Regional Development Fund).

REFERENCES

Bela, A., Le Sourne, H., Buldgen, L. & Rigo, P. 2017. Ship collision analysis on offshore wind turbine monopile foundations. *Marine Structures* 51, 220–241.

Buldgen, L., Le Sourne, H. & Pire, T. 2014. Extension of the super-elements method to the analysis of a jacket impacted by a ship. *Marine Structures* 38, 44–71

BV. 2021. Rules for the classification and certification of floating offshore wind turbines. *Standard NI572 R02* (Bureau Veritas).

Cerik, B.C., & Choung, J., 2020. On the modelling of strain-rate effects in nonlinear FE analysis of ship collisions. In: *Proceedings of the International Conference on Ships and Offshore Structures*, Glasgow.

Conti, F., Le Sourne, H., Vassalos, D., Kujala, P., Lindroth, D., Kim, S.J., Hirdaris, S., 2022. A comparative method for scaling solas collision damage distributions based on ship crashworthiness application to probabilistic damage stability analysis of a passenger ship. *Ships and Offshore Structures 17*, 1498–1514.

Dai, L., Ehlers, S., Rausand, M. & Utne, I. B. 2013. Risk of collision between service vessels and offshore wind turbines. *Reliability Engineering & System Safety* 109, 18–31.

DNV-GL. 2021. Recommended practice for determining design loads for offshore wind turbines. *DNVGL-RP-C204*.

Echeverry, S., Marquez, L., Rigo, P. & Le Sourne, H. 2019. Numerical crashworthiness analysis of a spar floating offshore wind turbine impacted by a ship. In: *Proceedings of the 8th International Conference on Collision and Grounding of Ships and Offshore Structures, ICCGS 2019*, 85–95.

Echeverry, S. 2021. Numerical and analytical study of a spar-like floating offshore wind turbine impacted by a ship. *PhD thesis, University of Liege*, 1–179.

Ferry, M., Le Sourne, H., Besnier, F., 2002. MCOL Theoretical Manual. *Principia Marine Technical Report*

Gresnigt, A. & Karamanos, S. A. 2014. Response of steel tubes under concentrated lateral loads. *Steel Construction* 7, 133–140.

Hollandse Kust. 2023. Rudderless Julietta D causes damage to foundation of wind farm Hollandse Kust. Zuid. *https://tinyurl.com/ycywdkuw. Accessed: 2023-04-04*.

IEC. 2020. Wind turbines – Part 3-2: Design requirements for offshore wind turbines. *Technical Specification 61400-3-2* (International Electrotechnical Commission).

Jones, N. 2011. Structural impact (Cambridge university press).

Jonkman, J. M. 2007. Dynamics modeling and loads analysis of an offshore floating wind turbine. *University of Colorado at Boulder*.

Jonkman, J., 2010. Definition of the Floating System for Phase IV of OC3. *Technical Report, National Renewable Energy Lab.* (NREL), Golden, CO (United States).

Ladeira, I., Echeverry, S. & Le Sourne H. 2023. A simplified method to assess the elasto-plastic response of standalone tubular Offshore Wind Turbine supports subjected to ship impact. *Ocean Engineering 279* 114313

Le Sourne, H. 2007. A ship Collision Analysis Program Based on Super-Element Method Coupled with Large Rotational Ship Movement Analysis. In: *Proceedings of the 4th International Conference on Collision and Grounding of Ships*, 131–138.

Le Sourne, H., Besnard, N., Cheylan, C. & Buannic, N. 2012. A ship collision analysis program based on upper bound solutions and coupled with a large rotational ship movement analysis tool. *Journal of Applied Mathematics 2012*.

Marquez, L., Le Sourne, H. & Rigo, P. 2022. Mechanical model for the analysis of ship collisions against reinforced concrete floaters of offshore wind turbines. *Ocean Engineering 261*, 111987.

Pineau, J.-P., Conti, F., Le Sourne, H. & Looten, T. 2022. A fast simulation tool for ship grounding damage analysis. *Ocean Engineering 262,* 112248.

Pire, T. 2018. Development of a code based on the continuous element method to assess the crashworthiness of an offshore wind turbine jacket. *PhD thesis - University of Liège*, 1–279.

Ting, L. & Yuan, S. 1958. On radial deflection of a cylinder of finite length with various end conditions. *Journal of the Aerospace Sciences* 25, 230–234.

Yu, Z., & Amdahl, J., 2018. A review of structural responses and design of offshore tubular structures subjected to ship impacts. *Ocean Engineering*, 154, 177-203.

Yu, Z., Amdahl, J., Rypestøl, M. & Cheng, Z. 2022. Numerical modelling and dynamic response analysis of a 10 MW semi-submersible floating offshore wind turbine subjected to ship collision loads. *Renewable Energy 184*, 677–699.

Zhang, Y., Hu, Z., Ng, C., Jia, C. & Jiang, Z. 2021. Dynamic responses analysis of a 5 MW spar-type floating wind turbine under accidental ship-impact scenario. *Marine Structures 75, 102885*.

Wierzbicki, T. & Suh, 1988. M. Indentation of tubes under combined loading. *International Journal of Mechanical Sciences* 30, 229–248.

B. FOWT.mco File Example

```
002$rigid body mass matrix (Mrb)
 8.0660E+06 0.0000E+00 0.0000E+00 0.0000E+00 0.0000E+00 0.0000E+00
 0.0000E+00 8.0660E+06 0.0000E+00 0.0000E+00 0.0000E+00 0.0000E+00
 0.0000E+00 0.0000E+00 8.0660E+06 0.0000E+00 0.0000E+00 0.0000E+00
 0.0000E+00 0.0000E+00 0.0000E+00 1.7442E+10 0.0000E+00 0.0000E+00
 0.0000E+00 0.0000E+00 0.0000E+00 0.0000E+00 1.7330E+10 0.0000E+00
 0.0000E+00 0.0000E+00 0.0000E+00 0.0000E+00 0.0000E+00 1.9200E+08
003$hydrostatic restoring matrix (Ks)
 0.0000E+00 0.0000E+00 0.0000E+00 0.0000E+00 0.0000E+00 0.0000E+00
 0.0000E+00 0.0000E+00 0.0000E+00 0.0000E+00 0.0000E+00 0.0000E+00
 0.0000E+00 0.0000E+00 6.9768E+05 0.0000E+00 0.0000E+00 0.0000E+00
 0.0000E+00 0.0000E+00 0.0000E+00 1.3316E+09 0.0000E+00 0.0000E+00
 0.0000E+00 0.0000E+00 0.0000E+00 0.0000E+00 1.3316E+09 0.0000E+00
 0.0000E+00 0.0000E+00 0.0000E+00 0.0000E+00 0.0000E+00 0.0000E+00
004$buoyancy parameters (xb,yb,zb,W=m*g,B=rho*g*displ,ZGref,PHIref,
TETAref)
 0.0000E+00 0.0000E+00-1.5900E+01 8.1588E+07 8.1588E+07 0.0000E+00
0.0000E+00 0.0000E+00
005$added mass matrix (Ma)
 8.3817E+06 0.0000E+00 0.0000E+00 0.0000E+00-4.9209E+08 0.0000E+00
 0.0000E+00 8.3817E+06 0.0000E+00 4.9209E+08 0.0000E+00 0.0000E+00
 0.0000E+00 0.0000E+00 2.2361E+05 0.0000E+00 0.0000E+00 0.0000E+00
 0.0000E+00 4.9210E+08 0.0000E+00 3.8289E+10 0.0000E+00 0.0000E+00
-4.9210E+08 0.0000E+00 0.0000E+00 0.0000E+00 3.8289E+10 0.0000E+00
 0.0000E+00 0.0000E+00 0.0000E+00 0.0000E+00 0.0000E+00 3.6443E-05
006$nbsurf and viscous damping surfaces (rho,dCl/dalpa,Cd,A,nx,ny,
nz,xc,yc,zc)
001
 0.1025E+04 0.0000E+00 0.6000E+00 1.1280E+03 0.0000E+00 0.1000E+01
0.0000E+00 0.0000E+00 0.0000E+00 0.0000E+00
007$parameter for checking convergence (gosa0,accl)
 0.1000E-03 0.1000E+01
008$nbomega, omega and wave damping matrixes [C(w)]
019
 0.10
 4.3731E+01 0.0000E+00 0.0000E+00 0.0000E+00-2.5514E+03 0.0000E+00
 0.0000E+00 4.3731E+01 0.0000E+00 2.5514E+03 0.0000E+00 0.0000E+00
 0.0000E+00 0.0000E+00 3.9459E+02 0.0000E+00 0.0000E+00 0.0000E+00
 0.0000E+00 2.5513E+03 0.0000E+00 1.4885E+05 0.0000E+00 0.0000E+00
-2.5513E+03 0.0000E+00 0.0000E+00 0.0000E+00 1.4885E+05 0.0000E+00
 0.0000E+00 0.0000E+00 0.0000E+00 0.0000E+00 0.0000E+00-4.5829E-16
 0.15
 1.9873E+02 0.0000E+00 0.0000E+00 0.0000E+00-1.1326E+04 0.0000E+00
 0.0000E+00 1.9873E+02 0.0000E+00 1.1326E+04 0.0000E+00 0.0000E+00
 0.0000E+00 0.0000E+00 5.9399E+02 0.0000E+00 0.0000E+00 0.0000E+00
 0.0000E+00 1.1325E+04 0.0000E+00 6.4543E+05 0.0000E+00 0.0000E+00
```

```
-1.1325E+04 0.0000E+00 0.0000E+00 0.0000E+00 6.4543E+05 0.0000E+00
 0.0000E+00 0.0000E+00 0.0000E+00 0.0000E+00 0.0000E+00-1.2853E-15
 0.20
 7.1751E+02 0.0000E+00 0.0000E+00 0.0000E+00-3.9429E+04 0.0000E+00
 0.0000E+00 7.1751E+02 0.0000E+00 3.9429E+04 0.0000E+00 0.0000E+00
 0.0000E+00 0.0000E+00 7.6676E+02 0.0000E+00 0.0000E+00 0.0000E+00
 0.0000E+00 3.9428E+04 0.0000E+00 2.1667E+06 0.0000E+00 0.0000E+00
-3.9428E+04 0.0000E+00 0.0000E+00 0.0000E+00 2.1667E+06 0.0000E+00
 0.0000E+00 0.0000E+00 0.0000E+00 0.0000E+00 0.0000E+00-3.1026E-15
 0.25
 2.2751E+03 0.0000E+00 0.0000E+00 0.0000E+00-1.1879E+05 0.0000E+00
 0.0000E+00 2.2751E+03 0.0000E+00 1.1879E+05 0.0000E+00 0.0000E+00
 0.0000E+00 0.0000E+00 8.3413E+02 0.0000E+00 0.0000E+00 0.0000E+00
 0.0000E+00 1.1879E+05 0.0000E+00 6.2025E+06 0.0000E+00 0.0000E+00
-1.1879E+05 0.0000E+00 0.0000E+00 0.0000E+00 6.2025E+06 0.0000E+00
 0.0000E+00 0.0000E+00 0.0000E+00 0.0000E+00 0.0000E+00-6.7779E-15
 0.30
 6.0459E+03 0.0000E+00 0.0000E+00 0.0000E+00-2.9576E+05 0.0000E+00
 0.0000E+00 6.0459E+03 0.0000E+00 2.9576E+05 0.0000E+00 0.0000E+00
 0.0000E+00 0.0000E+00 7.2483E+02 0.0000E+00 0.0000E+00 0.0000E+00
 0.0000E+00 2.9575E+05 0.0000E+00 1.4468E+07 0.0000E+00 0.0000E+00
-2.9575E+05 0.0000E+00 0.0000E+00 0.0000E+00 1.4468E+07 0.0000E+00
 0.0000E+00 0.0000E+00 0.0000E+00 0.0000E+00 0.0000E+00-1.2729E-14
 0.35
 1.3117E+04 0.0000E+00 0.0000E+00 0.0000E+00-5.9358E+05 0.0000E+00
 0.0000E+00 1.3117E+04 0.0000E+00 5.9358E+05 0.0000E+00 0.0000E+00
 0.0000E+00 0.0000E+00 5.0496E+02 0.0000E+00 0.0000E+00 0.0000E+00
 0.0000E+00 5.9357E+05 0.0000E+00 2.6860E+07 0.0000E+00 0.0000E+00
-5.9357E+05 0.0000E+00 0.0000E+00 0.0000E+00 2.6860E+07 0.0000E+00
 0.0000E+00 0.0000E+00 0.0000E+00 0.0000E+00 0.0000E+00-2.0212E-14
 0.40
 2.4143E+04 0.0000E+00 0.0000E+00 0.0000E+00-9.9773E+05 0.0000E+00
 0.0000E+00 2.4143E+04 0.0000E+00 9.9773E+05 0.0000E+00 0.0000E+00
 0.0000E+00 0.0000E+00 2.9152E+02 0.0000E+00 0.0000E+00 0.0000E+00
 0.0000E+00 9.9774E+05 0.0000E+00 4.1232E+07 0.0000E+00 0.0000E+00
-9.9774E+05 0.0000E+00 0.0000E+00 0.0000E+00 4.1232E+07 0.0000E+00
 0.0000E+00 0.0000E+00 0.0000E+00 0.0000E+00 0.0000E+00-2.8207E-14
 0.45
 3.9422E+04 0.0000E+00 0.0000E+00 0.0000E+00-1.4688E+06 0.0000E+00
 0.0000E+00 3.9422E+04 0.0000E+00 1.4688E+06 0.0000E+00 0.0000E+00
 0.0000E+00 0.0000E+00 1.4192E+02 0.0000E+00 0.0000E+00 0.0000E+00
 0.0000E+00 1.4688E+06 0.0000E+00 5.4723E+07 0.0000E+00 0.0000E+00
-1.4688E+06 0.0000E+00 0.0000E+00 0.0000E+00 5.4723E+07 0.0000E+00
 0.0000E+00 0.0000E+00 0.0000E+00 0.0000E+00 0.0000E+00-3.5942E-14
 0.50
 5.9019E+04 0.0000E+00 0.0000E+00 0.0000E+00-1.9594E+06 0.0000E+00
 0.0000E+00 5.9019E+04 0.0000E+00 1.9594E+06 0.0000E+00 0.0000E+00
 0.0000E+00 0.0000E+00 5.8725E+01 0.0000E+00 0.0000E+00 0.0000E+00
```

```
 0.0000E+00 1.9594E+06 0.0000E+00 6.5050E+07 0.0000E+00 0.0000E+00
-1.9594E+06 0.0000E+00 0.0000E+00 0.0000E+00 6.5050E+07 0.0000E+00
 0.0000E+00 0.0000E+00 0.0000E+00 0.0000E+00 0.0000E+00-4.2939E-14
 0.55
 8.2974E+04 0.0000E+00 0.0000E+00 0.0000E+00-2.4319E+06 0.0000E+00
 0.0000E+00 8.2974E+04 0.0000E+00 2.4319E+06 0.0000E+00 0.0000E+00
 0.0000E+00 0.0000E+00 2.0780E+01 0.0000E+00 0.0000E+00 0.0000E+00
 0.0000E+00 2.4320E+06 0.0000E+00 7.1278E+07 0.0000E+00 0.0000E+00
-2.4320E+06 0.0000E+00 0.0000E+00 0.0000E+00 7.1278E+07 0.0000E+00
 0.0000E+00 0.0000E+00 0.0000E+00 0.0000E+00 0.0000E+00-4.9004E-14
 0.60
 1.1146E+05 0.0000E+00 0.0000E+00 0.0000E+00-2.8664E+06 0.0000E+00
 0.0000E+00 1.1146E+05 0.0000E+00 2.8664E+06 0.0000E+00 0.0000E+00
 0.0000E+00 0.0000E+00 6.3183E+00 0.0000E+00 0.0000E+00 0.0000E+00
 0.0000E+00 2.8666E+06 0.0000E+00 7.3720E+07 0.0000E+00 0.0000E+00
-2.8666E+06 0.0000E+00 0.0000E+00 0.0000E+00 7.3720E+07 0.0000E+00
 0.0000E+00 0.0000E+00 0.0000E+00 0.0000E+00 0.0000E+00-5.4135E-14
 0.65
 1.4480E+05 0.0000E+00 0.0000E+00 0.0000E+00-3.2590E+06 0.0000E+00
 0.0000E+00 1.4480E+05 0.0000E+00 3.2590E+06 0.0000E+00 0.0000E+00
 0.0000E+00 0.0000E+00 1.6571E+00 0.0000E+00 0.0000E+00 0.0000E+00
 0.0000E+00 3.2592E+06 0.0000E+00 7.3353E+07 0.0000E+00 0.0000E+00
-3.2592E+06 0.0000E+00 0.0000E+00 0.0000E+00 7.3353E+07 0.0000E+00
 0.0000E+00 0.0000E+00 0.0000E+00 0.0000E+00 0.0000E+00-6.4198E-14
 0.70
 1.8339E+05 0.0000E+00 0.0000E+00 0.0000E+00-3.6144E+06 0.0000E+00
 0.0000E+00 1.8339E+05 0.0000E+00 3.6144E+06 0.0000E+00 0.0000E+00
 0.0000E+00 0.0000E+00 3.7595E-01 0.0000E+00 0.0000E+00 0.0000E+00
 0.0000E+00 3.6146E+06 0.0000E+00 7.1239E+07 0.0000E+00 0.0000E+00
-3.6146E+06 0.0000E+00 0.0000E+00 0.0000E+00 7.1239E+07 0.0000E+00
 0.0000E+00 0.0000E+00 0.0000E+00 0.0000E+00 0.0000E+00-2.1514E-14
 0.75
 2.2756E+05 0.0000E+00 0.0000E+00 0.0000E+00-3.9394E+06 0.0000E+00
 0.0000E+00 2.2756E+05 0.0000E+00 3.9394E+06 0.0000E+00 0.0000E+00
 0.0000E+00 0.0000E+00 7.3868E-02 0.0000E+00 0.0000E+00 0.0000E+00
 0.0000E+00 3.9397E+06 0.0000E+00 6.8204E+07 0.0000E+00 0.0000E+00
-3.9397E+06 0.0000E+00 0.0000E+00 0.0000E+00 6.8204E+07 0.0000E+00
 0.0000E+00 0.0000E+00 0.0000E+00 0.0000E+00 0.0000E+00-1.3884E-13
 0.80
 2.7739E+05 0.0000E+00 0.0000E+00 0.0000E+00-4.2382E+06 0.0000E+00
 0.0000E+00 2.7739E+05 0.0000E+00 4.2382E+06 0.0000E+00 0.0000E+00
 0.0000E+00 0.0000E+00 1.2599E-02 0.0000E+00 0.0000E+00 0.0000E+00
 0.0000E+00 4.2386E+06 0.0000E+00 6.4762E+07 0.0000E+00 0.0000E+00
-4.2386E+06 0.0000E+00 0.0000E+00 0.0000E+00 6.4762E+07 0.0000E+00
 0.0000E+00 0.0000E+00 0.0000E+00 0.0000E+00 0.0000E+00-2.0365E-14
 0.85
 3.3257E+05 0.0000E+00 0.0000E+00 0.0000E+00-4.5100E+06 0.0000E+00
 0.0000E+00 3.3257E+05 0.0000E+00 4.5100E+06 0.0000E+00 0.0000E+00
```

```
 0.0000E+00 0.0000E+00 1.8432E-03 0.0000E+00 0.0000E+00 0.0000E+00
 0.0000E+00 4.5104E+06 0.0000E+00 6.1166E+07 0.0000E+00 0.0000E+00
-4.5104E+06 0.0000E+00 0.0000E+00 0.0000E+00 6.1166E+07 0.0000E+00
 0.0000E+00 0.0000E+00 0.0000E+00 0.0000E+00 0.0000E+00-9.2391E-14
 0.90
 3.9227E+05 0.0000E+00 0.0000E+00 0.0000E+00-4.7490E+06 0.0000E+00
 0.0000E+00 3.9227E+05 0.0000E+00 4.7490E+06 0.0000E+00 0.0000E+00
 0.0000E+00 0.0000E+00 2.2552E-04 0.0000E+00 0.0000E+00 0.0000E+00
 0.0000E+00 4.7495E+06 0.0000E+00 5.7499E+07 0.0000E+00 0.0000E+00
-4.7495E+06 0.0000E+00 0.0000E+00 0.0000E+00 5.7499E+07 0.0000E+00
 0.0000E+00 0.0000E+00 0.0000E+00 0.0000E+00 0.0000E+00-4.4612E-14
 0.95
 4.5495E+05 0.0000E+00 0.0000E+00 0.0000E+00-4.9451E+06 0.0000E+00
 0.0000E+00 4.5495E+05 0.0000E+00 4.9451E+06 0.0000E+00 0.0000E+00
 0.0000E+00 0.0000E+00 2.0776E-05 0.0000E+00 0.0000E+00 0.0000E+00
 0.0000E+00 4.9457E+06 0.0000E+00 5.3757E+07 0.0000E+00 0.0000E+00
-4.9457E+06 0.0000E+00 0.0000E+00 0.0000E+00 5.3757E+07 0.0000E+00
 0.0000E+00 0.0000E+00 0.0000E+00 0.0000E+00 0.0000E+00 1.1764E-13
 1.00
 5.1841E+05 0.0000E+00 0.0000E+00 0.0000E+00-5.0861E+06 0.0000E+00
 0.0000E+00 5.1841E+05 0.0000E+00 5.0861E+06 0.0000E+00 0.0000E+00
 0.0000E+00 0.0000E+00 7.6761E-07 0.0000E+00 0.0000E+00 0.0000E+00
 0.0000E+00 5.0868E+06 0.0000E+00 4.9907E+07 0.0000E+00 0.0000E+00
-5.0868E+06 0.0000E+00 0.0000E+00 0.0000E+00 4.9907E+07 0.0000E+00
 0.0000E+00 0.0000E+00 0.0000E+00 0.0000E+00 0.0000E+00 1.3231E-13
```

C. Scheme of the SE Solver

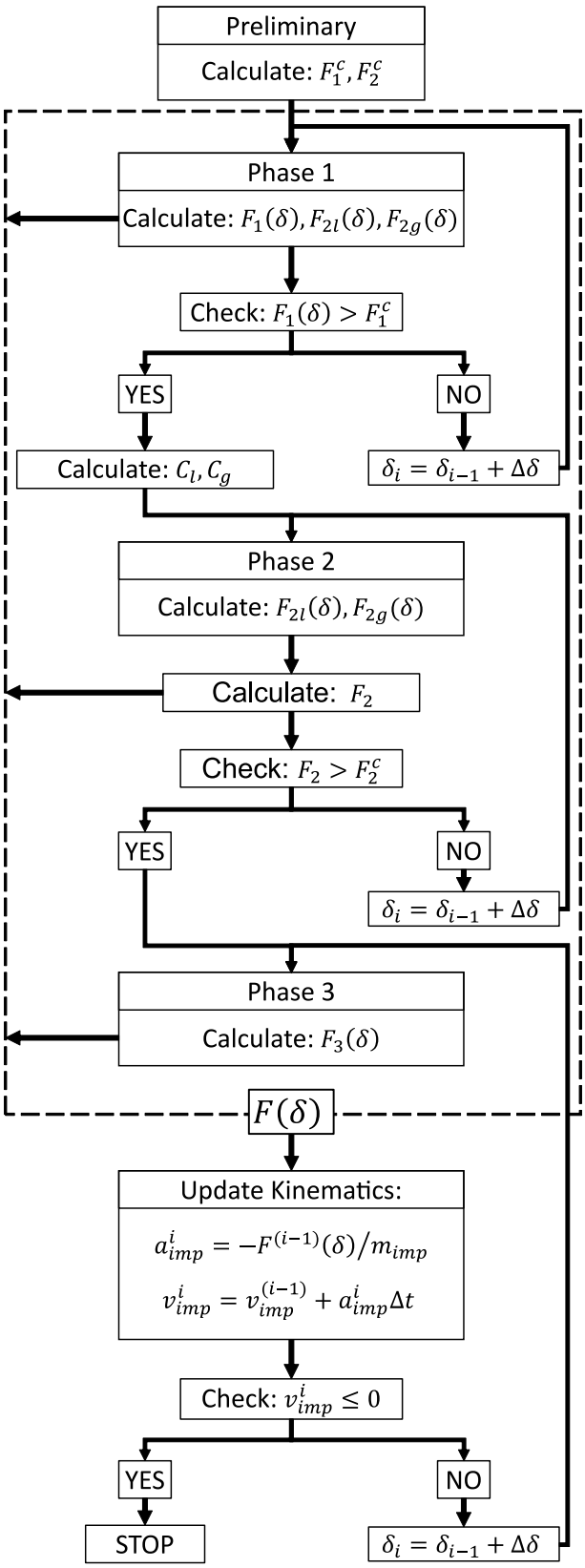

Figure C.1.: Schematic diagram of the SE solver algorithm. In the "Update Kinematics" box, the parameters v_{imp} and a_{imp} denote the velocity and acceleration of the impactor, respectively. *From: Ladeira et al., 2023*

D. Scheme of the Moorline Solver

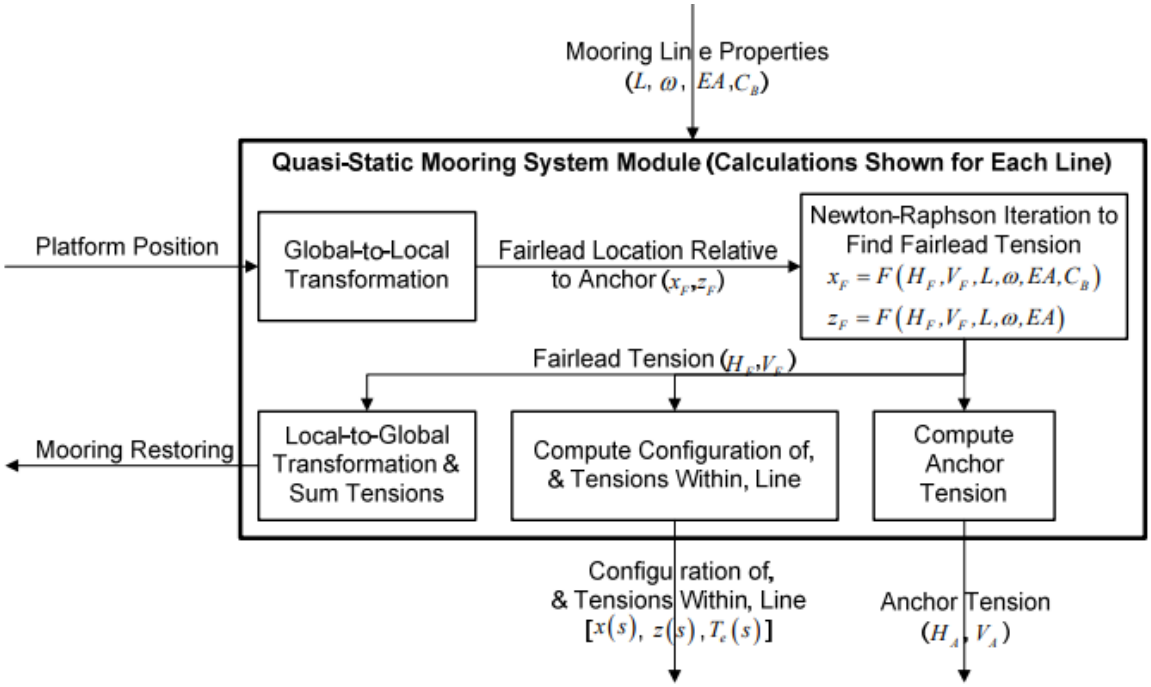

Figure D.1.: Schematic diagram of the Moorline algorithm. *From: Jonkman et al., 2007*

E. LS-DYNA version R13 Issues

With the version R13 of LS-DYNA, a few issues with MCOL were unresolved during the internship (March-July 2023). The main issue was that the velocities computed by MCOL in the version R13 was not equal to the velocity computed by integrating the acceleration. Fig. E.1 shows the difference between the results in both versions. With this figure, it can clearly be seen that the velocity computed in the version R13 is not correctly computed and therefore, another version should be used until the issue is fixed.

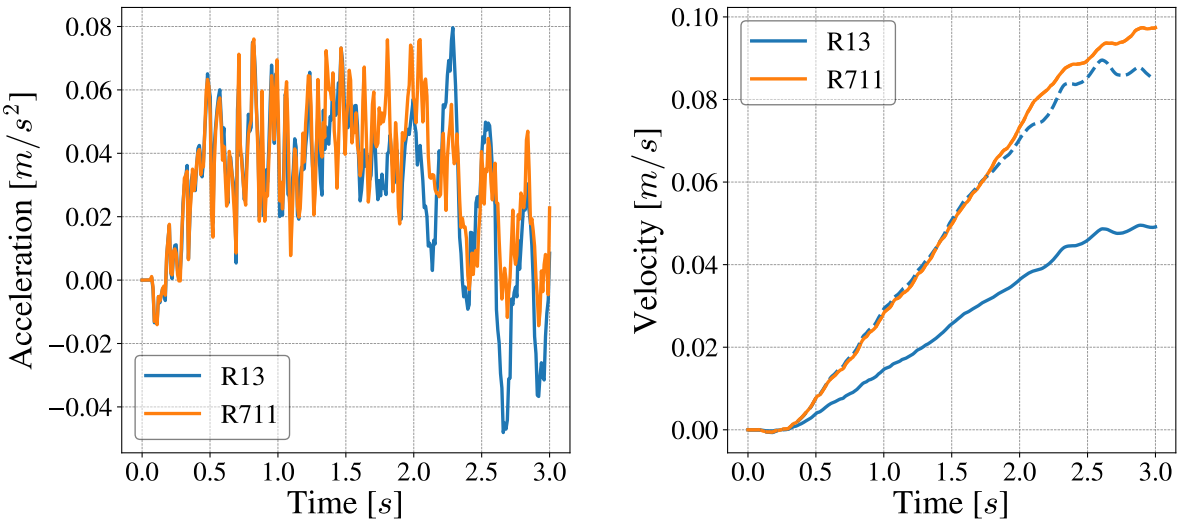

(a) Acceleration in sway.

(b) Velocity in sway.

Figure E.1.: Issue with the velocity computation in LS-DYNA version R13. In the velocity time history plot: (i) the continuous line is the velocity computed by LS-DYNA; (ii) the dashed line is the velocity computed by integration of the acceleration.